Simulation of Plasma Flows in Self-Field Lorentz Force Accelerators

Kameshwaran Sankaran

A DISSERTATION
PRESENTED TO THE FACULTY
OF PRINCETON UNIVERSITY
IN CANDIDACY FOR THE DEGREE
OF DOCTORATE OF PHILOSOPHY

RECOMMENDED FOR ACCEPTANCE
BY THE DEPARTMENT OF
MECHANICAL AND AEROSPACE ENGINEERING

January, 2005

Simulation of Plasma Flows in Self-Field Lorentz Force Accelerators

Prepared by:

_____

Kameshwaran Sankaran

Approved by:

_____

Professor Edgar Y. Choueiri
Dissertation Advisor, MAE Dept.

_____

Professor Stephen C. Jardin
Reader, Astrophysical Sciences

_____

Professor Luigi Martinelli
Reader, MAE Department

Acknowledgments

Give thanks to the Lord, for He is good;
His love endures forever.

Ever since I entered the doors of the Electric Propulsion & Plasma Dynamics Lab in 1997, my advisor Prof. Edgar Choueiri has played an influential role in my life. I learnt a lot from him - watching him at work in research, and in squash courts as well - and I hope I remember those lessons for the rest of my life. Thanks Eddie.

I came to the graduate school in Princeton largely due to a tradition of excellence in plasma propulsion research, built by Prof. Robert Jahn. After I came here, Prof. Jahn taught me the fundamentals of the plasma propulsion, and was always available to talk to me about "the big picture" of what research should be.

Prof. Steve Jardin taught me everything I know about computational plasma physics. He was around whenever I hit a wall (which I did frequently) and patiently guided me through the rough times. I've lost count of how many times he has bailed me out of a hole. On that note, I also thank Stephane Ethier, Ravi Samtaney and many others at the Princeton Plasma Physics Lab who gladly opened their doors and patiently answered my (often naive) questions.

Prof. Luigi Martinelli taught me the fundamentals of numerical methods and helped convince me that a new route to simulating plasma flows has to be taken. In addition to that, his role in mentoring and advising has been truly valuable to me.

My partners in crime over these years: John Ziemer, Vince Chiravalle, Tom Markusic, Jörg Heiermann (from U. Stuttgart), Andrea Kodys, Lenny Cassady, Kurt Polzin, Jack Berkery, Slava Spektor, Luke Uribarri and other graduate students (and staff such as Bob Sorenson) - provided encouragement, as well as many stimulating discussions. I hope to continue my friendship with them for a long time.

Tom & Christa (and of course their kids) were my family through these years, and their love was instrumental in my surviving the long and arduous journey through this valley of shadow of death.

For my parents and my siblings, this denotes a complete turnaround in my life. I want to thank them for their role in making me who I am.

I'm eternally grateful for the people of Westerly Road Church and Princeton Evangelical Fellowship, who made this homeless nomad feel at home. Special thanks go to Clay Porr, David Monn, Rajan Mathews, and Pastor Matt Ristuccia for their guidance and care, which got me through this mess.

In the end, all credit goes to whom it is due - to the one whose Name is above all names. Thank you for being the way, the truth, and my life.

This dissertation carries the designation 3121-T in the records of the Department of Mechanical and Aerospace Engineering.

Abstract

A characteristics-based scheme for the solution of ideal MHD equations was developed, and its ability to capture time-dependent discontinuities monotonically, as well as maintain force-free equilibrium, was demonstrated. Detailed models of classical transport, real equations of state, multi-level ionization models, anomalous transport, and multi-temperature effects for argon and lithium plasmas were implemented in this code. The entire set of equations was solved on non-orthogonal meshes, using parallel computers, to provide realistic description of flowfields in various thruster configurations. The calculated flowfield in gas-fed magnetoplasmadynamic thrusters (MPDT), such as the full-scale benchmark thruster (FSBT), compared favorably with measurements. These simulations provided insight into some aspects of FSBT operation, such as the weak role of the anode geometry in affecting the coefficient of thrust, the predominantly electromagnetic nature of the thrust at nominal operating conditions, and the importance of the near-cathode region in energy dissipation. Furthermore, the simulated structure of the flow embodied a number of photographically-recorded features of the FSBT discharge. Based on the confidence gained from its success with gas-fed MPDT flows, this code was then used to study a promising high-power spacecraft thruster, the lithium Lorentz force accelerator (LiLFA), in order to uncover its interior plasma properties and to obtain insight into underlying physical processes that had been poorly understood. The simulated flowfields of density, velocity, ionization, and anomalous resistivity were shown to change qualitatively with the total current. The simulations show the presence of a velocity reducing shock at low current, which disappeared as the current was increased above the value corresponding to nominal operation. The breakdown and scaling of the various components of thrust and power were revealed. The line on which the magnetic pressure equaled the gasdynamic pressure, and its motion with increasing current, was shown to provide a clear illustration of the anode starvation mechanism that leads to the current conduction crisis called onset.

Nomenclature

a	Sonic speed
$\mathbf{A}$	Jacobian of the hyperbolic system
$\mathbf{B}$	Magnetic induction vector
$\bar{\bar{\mathcal{B}}}_M$	Maxwell stress tensor
C	Wave propagation speed
$\mathbf{Dr}, \mathbf{Dz}$	Numerical dissipation in the radial and axial flux directions
e	Charge of an electron
E, E'	Electric field strengths in the lab and plasma reference frame
$\mathcal{E}$	Energy density
$\bar{\bar{\mathcal{F}}}$	Flux tensor
$\mathbf{Hr}, \mathbf{Hz}$	Radial and axial flux across the cell face
$\mathbf{j}$	Current density
J	Total current
k_B	Boltzmann's constant
k_{th}	Thermal conductivity
$\mathbf{Lr}, \mathbf{Lz}$	Flux limiters in the radial and axial directions
$\dot{m}$	Propellant mass flow rate
m	Mass of a particle
M	Mass of a particle
n	Number density of a specie
$\mathbf{n}$	Unit normal vector
p	Thermodynamic pressure
$\bar{\bar{p}}$	Isotropic pressure tensor
P	Total (magnetic+ thermodynamic) pressure

$\mathbf{q}$	Energy source/sinks
Q	Collision cross section
Q	Partition function
$\mathbf{R}, \mathbf{R}^{-1}$	Matrix of eigenvectors, and its inverse
R_m	Magnetic Reynolds' number
T	Thrust
T	Temperature
$\mathbf{u}$	Velocity vector
$\mathbf{U}$	Vector of conserved variables, $\rho, \rho\mathbf{u}, \mathbf{B}$, and $\mathcal{E}$
$\mathbf{U}_{J,K}^n$	Value of $\mathbf{U}$ at time $n \cdot \Delta t$ at the point $(J \cdot \Delta r, K \cdot \Delta z)$
u_{de}	Electron drift velocity
v_{ti}	Ion thermal velocity
Z	Average ionization fraction at a spatial location
β	Ratio of thermodynamic to magnetic pressure
γ	Ratio of specific heats
$\Delta r, \Delta z$	Cell-size in the radial and axial direction
$\Delta \mathbf{V}$	Characteristic increment in spacecraft velocity
ϵ_o	Permitivity of free space
η	Classical resistivity
$\bar{\bar{\eta}}$	Anisotropic resistivity tensor
λ	Eigenvalue
λ_D	Debye length
λ_{mfp}	Mean free path between collisions
$\mathbf{\Lambda}$	Diagonal matrix of eigenvalues
Λ	Plasma parameter = number of particles in a Debye sphere
μ_o	Magnetic permeability of free space

μ_{vis}	Coefficient of viscous dissipation
ν	Energy averaged momentum transfer collision frequency
ν_{AN}	Anomalous collision frequency
ρ	Average mass density of the fluid
τ	Characteristic time scale
$\bar{\bar{\tau}}_{vis}$	Viscous stress tensor
ψ	Stream function $= rB_\theta$
ω	Plasma frequency
Ω	Hall parameter (ratio of gyro and collisional frequncies)
Ω	Control volume in a mesh (cell)
$\lvert\,\Omega\,\rvert$	Volume of the cell Ω_j

Subscripts

a	Anode
c	Cathode
D	E $\times$ B drift
e	Electrons
ex	Exhaust
EM	Electromagnetic
g	Gasdynamic
h	Heavy species (Ar I, Ar II, Ar III, Ar IV, Li I, Li II, Li III)
i	Ions
j, k	Cell indices
r	Radial direction
w	Wall
z	Axial direction
θ	Azimuthal direction

Contents

List of Figures

Chapter 1

INTRODUCTION

The Earth is the cradle of the mind, but we cannot live forever in a cradle.

Konstantin E. Tsiolkovsky

1.1   Objective of This Thesis

The ultimate goals of this work are three-fold:

1. Realistic simulation of plasma flowfields in high-power Lorentz force accelerators with self-induced magnetic fields. For this purpose it is necessary to develop a full-fledged high-fidelity computational model in which the governing equations of the relevant physical processes are solved using a reliable numerical scheme.

2. Use the results of these simulations to:

   - Obtain detailed distributions of relevant flowfield parameters inside the thruster. Internal flowfield data are scarce due to the dearth of high-power experimental facilities and the difficulties in making measurements in harsh plasma environments.

- Obtain insight into the physics of thrust production and energy dissipation in these devices.

3. Use this code to understand the operation of a specific type of thruster, the lithium Lorentz force accelerator (LiLFA), for which experimental data is scarce.

1.2   Importance of Plasma Propulsion

Arguably the greatest technological achievement of the twentieth century was NASA's Apollo mission that successfully put men on the surface of the moon and brought them safely back to earth. However, only about 2% of the total mass of about 2750 metric tonnes of the rocket was useful payload. The bulk of the remaining mass was filled by the 960 thousand gallons of fuel needed for propulsion. The reason for the large propellant fraction is clear from the *rocket equation*, derived by Tsiolkovsky[1] in 1903. In the absence of external forces, the ratio of mass of propellant (m_{prop}) to the total mass of the rocket (m_{tot}) is given by the relation,

$$\frac{m_{prop}}{m_{tot}} = 1 - e^{-\Delta V/u_e} \, , \tag{1.1}$$

where u_e is the exhaust velocity of the propellant and ΔV is the characteristic velocity increment imparted to the vehicle.

Since the exhaust velocities of the chemical rockets used in the *Saturn V* were relatively small (the F-1 engines used in the first stage had exhaust velocities ranging from 2600 to 3000 m/s from sea level to high altitude, and the J-2 engines used in the second and third stage had an exhaust velocity of 4200 m/s at high altitude) compared to the ΔV requirements for the mission, the mass of propellant required was enormous. Despite the advances in combustion research, the highest exhaust velocity of a functional chemical propulsion system, 3600 to 4500 m/s from sea level to high altitude (of the Space Shuttle Main Engine), is still inadequate for most deep-space missions of interest[2]. The reinvigorated vision of NASA[3] calls for missions beyond the moon, and for

such missions chemical propulsion is not a viable option, except for the case of launch vehicles where high thrust is required.

Functionally, the inability of chemical propulsion systems to achieve higher exhaust velocities is due to the limitation in the maximum tolerable temperature in the combustion chamber, to avoid excessive heat transfer to the walls. Fundamentally, there is also an intrinsic limitation on the maximum energy that is available from the chemical reactions.

Both these limitations can be overcome by the use of electric propulsion, a working definition of which is found in ref.[2],

> *The acceleration of gases for propulsion by electrical heating and/or by electric and*
> *magnetic body forces.*

Two distinct means to harness electrical power to accelerate propellants can be identified:

1. Heating the propellant locally, such that average temperatures are higher than those that can be tolerated by the walls,

2. Acceleration of the propellant by the application of body forces.

The first method can be understood by observing that the electrical power deposited per unit volume of the plasma is,

$$\mathbf{j} \cdot \mathbf{E} = \left\{ \eta j^2 \right\} + \left\{ (\mathbf{j} \times \mathbf{B}) \cdot \mathbf{u} \right\} . \tag{1.2}$$

By maximizing the first term, the Ohmic heating, the electrical power can be used to increase the enthalpy of the propellant in a localized fashion, thus avoiding excessive temperatures near the walls. This allows for the average chamber temperature to be higher than those attainable in chemical propulsion systems. The enthalpy can be recovered and converted into directed kinetic energy using a nozzle, as in a chemical rocket. This is the acceleration mechanism in *electrothermal thrusters* such as *arcjets, resistojets* and *microwave-heated thrusters*.
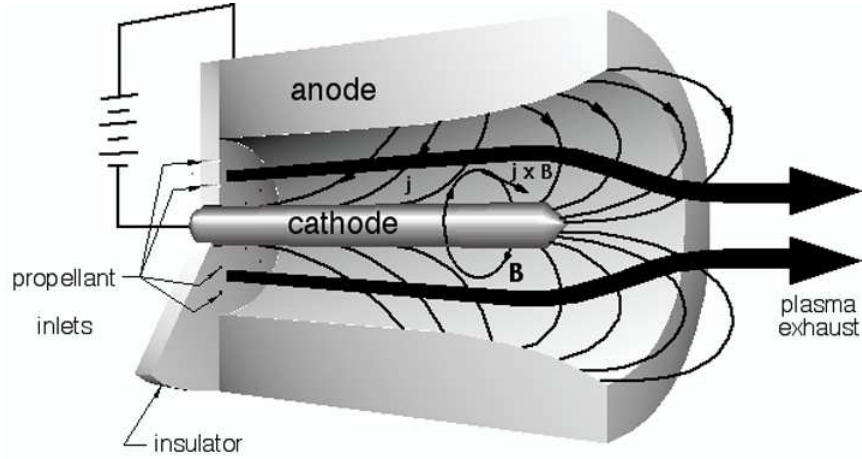
Figure 1.1: Schematic of plasma acceleration in a magnetoplasmadynamic thruster.

The second acceleration method relies on bypassing thermal expansion altogether, via application of direct body forces. This can be achieved by forces exerted by electrical and magnetic fields on an ionized gas:

$$\mathbf{f}_{ext} = \{\rho_e \mathbf{E}\} + \{\mathbf{j} \times \mathbf{B}\} \ . \tag{1.3}$$

From eqn.(1.3) two distinct means of application of body forces can be identified. The first term is the body force due to an external electric field. This is the acceleration mechanism in *electrostatic thrusters* such as *ion thrusters* and *field emission thrusters*.

For a highly conducting, quasineutral working fluid, the first term in eqn.(1.3) is small (as will be shown in §2.1 , eqn.(2.4)), compared to the second, the electromagnetic body force (a.k.a. *Lorentz force*). This is the driving force in *electromagnetic thrusters* such as *magnetoplasmadynamic thrusters*, and *pulsed plasma thrusters*. As shown in Fig.(1.2), this body force accelerates the fluid in the direction perpendicular to both the electric and the magnetic fields. The energy expended in this process is given by the second term in eqn.(1.2).

It is important to note that, although the various means for using electrical power to accelerate gases has been explained in a conceptual fashion, the discovery of these methods was often

4

empirical. For instance, magnetoplasmadynamic acceleration was discovered when an arcjet was operated under conditions of very low mass flow rates and high currents[4], at which the second term of eqn.(1.2) dominated the first.

In order to provide the obligatory electrical power for magnetoplasmadynamic acceleration, an on-board power supply has to be carried along. Therefore, the problem now reduces to that of minimizing the combined mass of the power supply and the mass of the propellant, instead of merely the latter. As seen in eqn.(1.1), the required propellant mass decreases with increasing exhaust velocity. However, for a system that provides a constant thrust, at a constant efficiency, the mass of the powerplant increases with increasing exhaust velocity[2]. Thus, the exhaust velocity should be at an optimum value that minimizes the combined mass of propellant and power supply. Moreover, for piloted missions, the optimization has to be done not only for minimum propellant mass but also for a reasonable trip time. Due to these factors, the choice of a propulsion system is mission specific. Over their periods of development, many varieties of electric propulsion systems have spawned their own array of technical specialties and subspecialties, and their own cadres of proponents and detractors[5]. As described in ref.[6], many of these technologies have carved out their own niche, and have validly qualified for specific applications, to various degrees of suitability. Appendix A describes how some of these propulsion systems are suited for a piloted missions to Mars, and ref.[6] expands the discussion to consider Mars cargo missions as well.

All electric propulsion systems are intrinsically thrust limited, because, it is not practically feasible to electrically supply power of the same order as that is available from chemical/nuclear reactions. This is obvious from observing that the kinetic power in the exhaust of the *Saturn V* rocket (about 120 GW) is more than 50 times greater than the maximum electrical power generation capacity of the Hoover dam. In the absence of such colossal electrical power supplies, electric propulsion systems are not suitable for overcoming steep gravitational potential wells, such as launching from earth's surface. However, they are well suited for missions where the instanta-

neous thrust requirements are small (in micro-gravity environments), but the total impulse ($\int T dt$) requirements are large.

Magnetoplasmadynamic thrusters (MPDT) (and their variants, lithium Lorentz force accelerators (LiLFA),) and pulsed-plasma thrusters (PPT) use quasineutral plasma as a working fluid. Therefore, unlike ion thrusters (cf. ref.[7])), they are not constrained by space-charge limitations[2]. Moreover, since MPDTs/LiLFAs and PPTs rely on the interaction of the collision dominated current, rather than the Hall current, with magnetic field to produce thrust, they can operate at much larger mass flow rates and densities than Hall thrusters[2].

The MPDT/LiLFA has the unique capability, among all developed electric thrusters, of processing megawatt power levels in a simple, small and robust device, producing thrust densities as high as 10^5 N/m^2. These features render it an attractive option for high energy deep-space missions requiring higher thrust levels than other EP systems[5], such as piloted and cargo missions to Mars and other outer planets, as well as for near term missions such as transfer from LEO to GEO[8].

1.3   Research Issues in High-Power Plasma Thrusters

The gas-fed self-field MPDT is the most studied high-power plasma propulsion device, and has been the subject of numerous graduate theses (such as refs.[9]-[33]). Yet, despite four decades of research and development involving laboratory tests of many permutations of geometries and operating conditions and even a space flight test[34], no MPDT is currently used on operational spacecraft. Three reasons can be identified for the present absence of MPDTs in actual spaceflight missions:

1. Intolerably high cathode erosion rates,

2. Unacceptably low efficiencies at low power levels that are available today in space,

3. Occurrence of performance limiting oscillations at operation above a certain value of $J^2/\dot{m}$.

Fortunately, it has been known for some time (cf. refs.[35, 36, 37, 38]) that using a multi-channel hollow cathode, with alkali metals such as lithium as the propellant, promises to alleviate some of these pitfalls. The improvements on the first two drawbacks are perhaps because,

1. Multi-channel hollow cathodes have lower surface current densities and therefore have lower electrode evaporation rates. Moreover, compared to all other potential propellants, lithium coated electrodes have a lower work function ($\phi = 2.9$ eV) than uncoated electrodes[39, 27] ($\phi = 5.4$ eV). A combination of these two factors reduces the electrode erosion rates significantly, thus improving the thruster lifetime.

2. Lithium has a low ionization potential, and therefore the fraction of input power expended in ionizing the propellant is reduced.

This version of the MPDT is termed the lithium Lorentz force accelerator (LiLFA) for historical reasons to differentiate it from the traditional gas-fed solid cathode MPDT variant. The LiLFA has demonstrated essentially erosion-free operation for over 500 hours of steady thrusting, with excellent performance characteristics (12.5 N of thrust, 4000 sec I_{sp}, and 60% efficiency at 500 kW of input power[40]).

For high energy, deep-space missions, these thrusters would operate at power levels of several megawatts (MW). However, testing these devices at MW power levels presents formidable technological and economic challenges. In fact, there are no experimental facilities at present that are capable of long-term MW-level operation of a MPDT/LiLFA. To this date all data in the MW range has been taken in quasi-steady mode. In this mode, the thruster is operated for current pulse length of $\mathcal{O}(1$ ms), and data from this mode is expected to be a good indicator of its steady-state performance[41]. Databases of measured quasi-steady thruster performance have been compiled in Japan [42] and at Princeton University [43]. A MW-class pulsed facility at the NASA-Glenn Research Center began operation in 2001, with plans to develop it to a steady-state facility[44]. So far, steady-state data is limited to less than 600 kW, and has been obtained mostly at the NASA Glenn

(formerly Lewis) Research Center[45], and at the University of Stuttgart[46]. The NASA-Lewis test facility had the capability to operate at steady-state power level of up to 600 kW, but research was discontinued by the early 1990s. NASA-JPL has only recently completed development of a 500 kW facility to test the LiLFA.

The dearth of high-power experimental facilities implores the need for a rational alternative to empirical testing, as a way to predict performance. Unfortunately the simple explanation for the acceleration mechanism described earlier, in §1.2, belies the complexity that underlies the electromagnetic acceleration process, which embodies interlocking aspects of compressible gasdynamics, ionized gas physics, electromagnetic field theory, particle electrodynamics[2], collective plasma phenomena and plasma-surface interactions[27]. Consequently, a realistic description of the acceleration process is analytically intractable. This inability is the foremost hindrance to understanding the details of processes by which the electrical energy is partitioned among various energy sinks, including acceleration.

As shown in Fig.(1.3), the electrical power deposited into the plasma can be expended into many sinks, only two of which, directed electromagnetic kinetic power and directed electrothermal kinetic power, are useful for propulsion. Understanding and quantifying these disparate processes is essential to improving the efficiency of these devices. Since it is difficult to do so using an empirical or analytical approach alone, numerical simulations are valuable tools in plasma thruster research.

Over the years, there have been several notable attempts to develop detailed numerical models to study MPDT flows. Some of them will be summarized below.

1.4   Existing Computational Work

The earliest recorded attempt to simulate the flowfield in a high-power plasma accelerator was made by Burshlinkskii, Morozov *et al.*[48, 49, 50] (1967-68). Due to serious limitations on com-
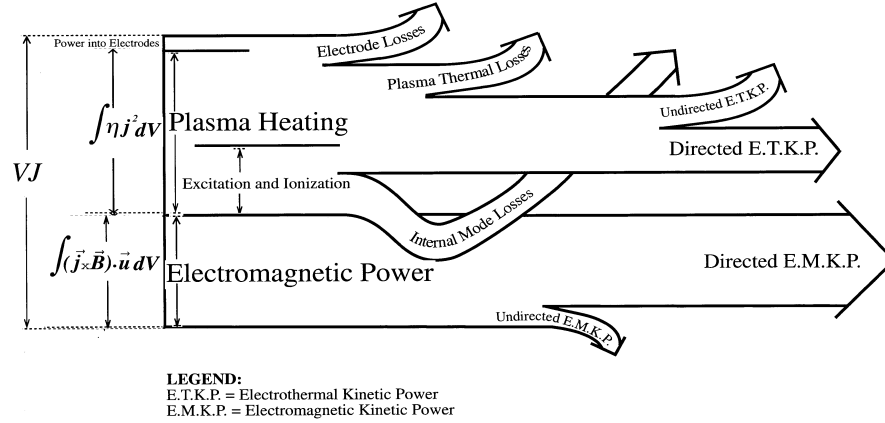
Figure 1.2: Expenditure of input power in an electromagnetic accelerator (from ref.[47]).

putational power available in the 1960s, their model had to be relatively simple. It excluded the energy equation, and assumed a constant uniform value of resistivity. Nevertheless, their code was able to make reasonable predictions of current and density contours in coaxial devices.

Kimura $et\ al.$ [51] (1982), and Fujiwara $et\ al.$[52] (1984), started developing single-temperature, 2-D models on simple geometries, and have continued to make improvements to their models. Currently, the efforts of Fujiwara $et\ al.$[53] (1999) are directed at studying critical phenomena in magnetoplasmadynamic thrusters, using multi-temperature models.

Chanty, Niewood, Martinez-Sanchez $et\ al.$ [54, 30] (1987-93) have developed two-temperature axisymmetric numerical models to study various aspects of the flow. The model of Niewood[30] (1993) includes a non-equilibrium ionization model developed by Sheppard[31], and accounts for effects due to the presence of neutrals, such as ion-neutral slip.

The effort by LaPointe[55] (1992) was aimed at simulating the effect of geometry on performance on the ZT-1 thruster[56] and the Half-Scaled Flared Anode Thruster (HSFAT)[22].

Caldo and Choueiri[57] (1994) developed a two-temperature model to study the effects of anomalous transport, described in ref.[58], on MPDT flows. The steady state form of Faraday's

9

law and time-dependent form of the flow equations were solved using a multigrid, multi-stage time iteration scheme, on a grid that was customized for Princeton's Full-Scale Benchmark Thruster (FSBT)[16].

The most persistent effort so far has been that of Auweter-Kurtz, Sleziona, Heiermann, *et al.*[59, 60, 56, 61, 62, 63, 64, 65, 33] (1989-2002) at the University of Stuttgart, who, for almost two decades, have been developing numerical models for MPDTs. Detailed models for many transport processes and multiple levels of ionization have been incorporated into their governing equations, which are solved on unstructured adaptive grids. The major objective of this work is to predict the overall performance of the ZT-1 and the HAT series of thrusters. Another proposed used of their code is to study the role of gradient-driven instabilities in MPDT flows[66].

Turchi, Mikelllides, *et al.* [32, 44, 67, 68, 69] (1994-2004) utilized MACH2, a widely-used unsteady MHD solver developed for high power plasma gun simulations[70], to model PPTs and MPDTs in many geometries. MACH3[71] (1995), the next generation of MACH2, is also used to simulate possible 3-D effects in specific situations.

1.5   Scope of This Thesis

Though the abovementioned research efforts have made significant progress in simulating MPD flows, there remains room for improvement in both physical models and numerical schemes used in them.

As is argued in §2.3.6, it is important to have equation-of-state models that are suitable to the conditions of interest to plasma thrusters. In addition, it is important to have reliable models for classical and anomalous transport, as well as ionization processes.

At a more fundamental level, any code used to predict plasma properties should be first validated against standard MHD test problems for which analytical solutions exist, as well as by comparisons with plasma thruster experiments for which experimental data exist.

While it can be argued that the existing codes can be adapted to meet the abovementioned requirements, it is not viable to change the underlying numerical methods of a code. Some notable shortcomings of existing numerical models can be identified:

1. Some of the existing codes exhibit numerical instabilities at high current levels. MPDTs reach higher efficiencies at higher currents, until a value at which voltage oscillations occur, and many of the important research questions tend to also occur at higher current levels. Consequently, the inability of a simulation to work reliably at those situations undermines its value.

   A probable explanation for these instabilities is the failure to solve the magnetic field evolution self-consistently with the flow. For highly resistive flows, the time scale for resistive diffusion of the magnetic field is orders of magnitude smaller than that of convection. However, in MPDT flows it is common to have resistivities of $\mathcal{O}(10^{-4})$ Ohm m. In such situations, these time scales are not very far off, and there is a strong coupling between the flow and the magnetic field. The corresponding magnetic Reynolds' numbers $Re_m \sim \mathcal{O}(1-10)$ indicate that both convective and resistive diffusion of the magnetic field are important (to be discussed later in §2.3.3). Moreover, the Alfvèn and fluid time scales are not very disparate. Therefore, the full set of equations describing the flow field and magnetic field evolution has to be computed self-consistently.

   An important feature of the MHD formalism is the multitude of waves it permits to exist. The nonlinear coupling of these waves play an important role in determining physical phenomena and in computing the solution, as explained in ref.[72, 73]. Solving Maxwell's equations consistently with compressible gasdynamics equations naturally produces waves physically associated with the problem, such as Alfvèn and magnetosonic waves, as eigenvalues. Such a formulation is thus suitable for handling MHD waves and shocks.

2. Some of the earlier efforts[57, 59] have experienced problems conserving mass, momentum,

11

and energy. A conservative formulation of the governing equations ensures that these quantities are indeed conserved. Such a formulation also facilitates the application of boundary conditions, since the fluxes are the only quantities to be specified at the boundaries. From the perspective of numerical solution, it can be shown that conservative formulation is necessary for accurately capturing discontinuities.

3. As also noted in ref.[30], none of the existing models (with the exception of recent work at the University of Stuttgart[61, 62, 63, 64, 65, 33]) take advantage of the developments in the techniques for numerical solution of Euler and Navier-Stokes equations.

Each of the problems mentioned above can be overcome, respectively, by adapting the following approach:

1. Treat the flow and magnetic field equations in a self-consistent manner,

2. Formulate the governing equations in a conservative form,

3. Use characteristics-splitting techniques satisfying Rankine-Hugoniot relations, combined with anti-diffusion to increase accuracy. These techniques can capture shocks and other strong gradients in a non-oscillatory manner, and can have good spatial accuracy in smooth regions of the flow.

The development of precisely such a code, and its application to produce realistic simulations of the internal flowfield, and obtaining insight into the underlying physical phenomena from those simulations, is the subject of this thesis.

The physical models and numerical methods developed in this thesis, and the code itself, can be used to study many types of plasma thrusters. However, this thesis focuses only on high-power Lorentz force accelerated thrusters with self-induced magnetic fields (magnetoplasmadynamic thrusters (MDPTs) and Lithium Lorentz Force Accelerators (LiLFAs)).

1.6 Outline

The physical models that describe the evolution of the flow and the field are described in chapter 2. A concise review of existing analytical models is made, and the need for a detailed multi-dimensional, time-dependent numerical simulation is demonstrated. Subsequently, the MHD equations, which form the core of the current model, are briefly reviewed. Models for classical and anomalous transport coefficients, effects of thermal nonequilibrium between electrons and ions, a real equation of state, and a multi-level equilibrium ionization model are also developed in chapter 2.

The techniques that are used to obtain a numerical solution of the governing equations are discussed in chapter 3. First, the relevant fundamental concepts are summarized. Following that, a new characteristics-splitting scheme developed for the solution of the ideal MHD equations is described. Finally, the validation of this scheme, by solving standard test problems with known analytical solutions, is also described in chapter 3.

The physical models, presented in chapter 2, are incorporated into the numerical scheme, developed in chapter 3, and are used to simulate plasma flows in a real MPDT configurations in chapter 4. It includes descriptions of the thruster geometries, along with appropriate boundary conditions required to obtain realistic solutions. The profiles of many relevant physical properties, obtained from the converged numerical solutions, are then compared with experimental data in chapter 4.

The confidence acquired from accurately predicting MPDT flows sets the stage for predicting flowfields in thrusters for which little or no internal data exist, and extracting insight into the underlying physical processes in the LiLFA. This is the subject of chapter 5.

A summary of this work and the recommendations for future work are discussed in chapter 6.

Chapter 2

PLASMA FLOW MODELING

I have been carried ... into that sanctuary of minuteness and of power, where molecules obey the laws of their existence, clash together in fierce collision, or grapple in yet more fierce embrace, building up in secret the forms of visible things. But who will lead me into that still more hidden and dimmer region where Thought weds Fact, where the mental operation of the mathematician and the physical action of the molecules are seen in their true relation?

James Clerk Maxwell

The physical laws governing the flow of the plasma and the evolution of the magnetic field in Lorentz force accelerators are discussed in this chapter. First, the case for a continuum treatment of the plasma is made. Then, a brief review of existing analytical models for MPDT flows is made and the need for a comprehensive multi-dimensional time-dependent model is demonstrated. Subsequently such a model, the set of MHD equations, is discussed along with effects of thermal nonequilibrium, appropriate expressions for classical and anomalous transport, a real equation of state, and a multi-level equilibrium ionization model.

2.1 Continuum Model of the Plasma

The mechanism of plasma acceleration in an electromagnetic thruster can be described in terms of the mean trajectories of the current-carrying electrons, as done in ref.[2]. While attempting to follow the applied electric field, the electrons are turned in the stream direction by the magnetic field with a velocity,

$$\mathbf{V}_D = \frac{\mathbf{E} \times \mathbf{B}}{B^2} \ .$$

(2.1)

The motion of these electrons then sets up microscopic polarization fields that accelerate the ions. Alternatively, the transfer of streamwise momentum from electrons to the bulk of the plasma can also be accomplished through collisions. It is important to observe that, in either process, the working fluid remains quasineutral, that is, there is no macroscopic charge separation.

If limitless computing power is available, a perfect simulation would solve for the trajectory of every particle in three-dimensional space, subject to fundamental physical laws such as Newton's laws and Maxwell's equations (with some knowledge of quantum mechanics to estimate collision cross sections). However, for conditions of interest to plasma thrusters, with electron and ion densities of $\mathcal{O}\left(10^{21}\right)/\mathrm{m}^3$, mass-averaged velocities $\mathcal{O}(10^4)$ m/s, temperatures of ~ 2 eV, thermodynamic pressures of $\mathcal{O}(10^{-1}-1)$ Torr, and magnetic pressures of $\mathcal{O}(1-10)$ Torr, particle simulations are not presently practical, even when following only representative or macro particles.

Under these conditions, the most useful approach to understanding the nature of electromagnetic acceleration is that of magnetohydrodynamics, in which the ionized gas is treated as a continuum fluid whose physical properties are described by a set of bulk parameters whose dynamical behavior is represented by a set of conservation relations[2].

For typical operating conditions, the MPDT/LiLFA plasma is quasineutral. This assumption can be justified by the following rationale:

1. The dimensions of the device are much larger than the characteristic length scale of charge

separation (the *Debye length*),

$$\frac{L}{\lambda_D} \sim \mathcal{O}\left(10^5\right) \ .$$ (2.2)

2. The residence time scale is much larger than the time scale needed for the electrons to adjust to the charge separation (inverse of the *electron plasma frequency*),

$$\frac{\tau_{res}}{1/\omega_{pe}} \sim \mathcal{O}\left(10^5\right) \ .$$ (2.3)

3. Inertial forces are far greater than the electrostatic force due to charge separation,

$$\frac{\rho\mathbf{U}\cdot\nabla\mathbf{U}}{\rho_e E} \sim \mathcal{O}\left(10^9\right) \ .$$ (2.4)

From these, it is sensible to treat the plasma in the bulk of the device as quasineutral. There is, however, a *sheath* at the interface between the plasma and a boundary, where the quasineutral assumption breaks down. Modeling the sheath will be a topic for future research, and is discussed in §6.2.2.

The continuum treatment is reasonable because the characteristic length scale of the device is found to be much larger than the mean free path between collisions:

$$\frac{L}{\lambda_{mfp}} \sim \mathcal{O}\left(10^3\right) \ .$$ (2.5)

In self-field accelerators, the flow direction of the plasma is perpendicular to the magnetic field. In such a situation, the magnetic field further bolsters the continuum approximation by playing the role of collisions in maintaining Maxwellian distributions and in providing the 'localizing influence' that is the essential ingredient of the fluid theory (cf. ref.[74]).

Now that the continuum treatment has been justified, the acceleration mechanism (in a self-field device such as the one shown in Fig.(1.2)) can be described as follows: The applied electric field, $\mathbf{E}$, induces a current of density $\mathbf{j}$, which induces a magnetic field $\mathbf{B}$. The interaction of the current and the magnetic field produces a distributed body force density, $\mathbf{f}_{EM} = \mathbf{j}\times\mathbf{B}$, that accelerates the flow.

16

2.2 Simplified Analytical Models

An analytical model, based on the continuum description, to predict the *electromagnetic* component of thrust was developed by Maecker[75], and later expounded by Jahn[2]. The essence of this approach is a calculation of the unbalanced magnetic pressure acting on the thruster, by evaluating the surface integral of the magnetic stress tensor (to be explained in §2.3.2). The result of that analysis is that for a total operating current of J, the thrust is given by,

$$T = \frac{\mu_o}{4\pi}\left(\ln\frac{r_a}{r_c} + A\right)J^2, \tag{2.6}$$

where r_a and r_c are the radii of the anode and the cathode, respectively, and A is a dimensionless constant between 0 and 1. Note that this formula needs no information on field distribution patterns inside the thruster or the propellant type or even the mass flow rate. Yet, Maecker's formula (eqn.(2.6)) generally predicts the thrust with acceptable accuracy over a wide range of operating conditions.

However, as pointed out in ref.[76], the deviations from Maecker's law are significant at currents below a critical value. The model by Tikhonov *et al.*[77] improved on the Maecker's formula by proposing the following scaling relation,

$$T = \frac{\mu_o}{4\pi}\left(\frac{\gamma+1}{2} + \frac{1}{2}\left(\frac{8\pi a_o \dot{m}}{\gamma\mu_o J^2}\right)^2\right)J^2, \tag{2.7}$$

obtained from a quasi-1-D MHD analytical model that allows the free boundary of the flow to vary consistently with the flow conditions. Here, a_o is the ion acoustic speed evaluted at the upstream end. The Tikhonov thrust scaling law will be useful in the discussion of the LiLFA in §5.3. Though the Tikhonov scaling law is an improvement over the Maecker's law, it still does not account for the type of propellant or any details of the geometry. The model of Choueiri[76], however, accounts for variations in current distribution patterns and propellant types. However, that model is semi-empirical in nature, requiring some experimental data for current distribution patterns on the electrodes and the pressure distribution on the backplate. Nevertheless, it provides

17

excellent predictions of thrust and is very useful in the understanding of thrust scaling trends. Specifically, it was shown that the non-dimensional parameter

$$\xi \equiv \left[\frac{\frac{\mu_o J^2}{4\pi} \left(\ln \frac{r_a}{r_c} + A \right)}{\dot{m} \sqrt{2\phi_i/M}} \right]^{1/2}, \tag{2.8}$$

with

A a dimensionless constant between 0 and 1,

$\dot{m}$ the mass flow rate,

ϕ_i the first ionization potential of the propellant, and

M the atomic weight of the propellant,

plays an important role in many scaling relations. This can also be viewed as an appropriate non-dimensionalization of the thruster current,

$$\xi \equiv \frac{J}{J_{ci}}, \tag{2.9}$$

where J_{ci} is the Alfvèn critical ionization current,

$$J_{ci} = \left[\frac{\dot{m} \sqrt{2\phi_i/M}}{\left(\frac{\mu_o}{4\pi} \right) \left(\ln \frac{r_a}{r_c} + A \right)} \right]^{1/2}. \tag{2.10}$$

It has been shown[76] that nominal operation is achieved at $\xi \simeq 1$.

By and large, these analytical models have been successful in accurately predicting the electromagnetic thrust. This is because a good estimate of the magnetic pressure acting on the boundaries can be made from the total current, without detailed knowledge of field distributions within the channel.

However, as mentioned in §1.3, prediction of energy dissipation is a far more challenging endeavor. Some of the earlier efforts to understand the energetics were made by DiCapua[10],

Villani[18] and King[17] at Princeton. Armed with experimental information on relevant parameters, they constructed simple analytical models to estimate the expenditure of energy. They will now be briefly reviewed.

DiCapua[10] investigated the energy loss mechanisms in a parallel plate accelerator, using a simple 1-D model. A magnetic boundary layer model, in which the convection and diffusion of the magnetic field was estimated, was used to explain some of the features of the discharge region. The analysis using momentum and energy balance indicated that over currents ranging from 10 kA to 100 kA, with argon mass flow rates such that $J^2/\dot{m} = 37.0\,\text{kA}^2/\text{g/s}$, up to 85% of the input power appeared in the exhaust. However, only $\sim 20\%$ was in the form of directed kinetic energy of the flow, with the remainder going into ionization and raising the enthalpy. It was concluded that the Ohmic heating term was always greater than the energy expended in accelerating the working fluid (cf. ref.1.2).

Villani's efforts[18] were focused on the understanding effect of current distribution on the efficiencies of coaxial thrusters. From simple order-of-magnitude analysis, he determined that predicting the total power consumed by the thruster reduces to the problem of estimating the volume integral of the Ohmic heating term. Observing that the variations in j^2 in the channel far exceed the corresponding variations in the values of resistivity (η), it was demonstrated that Ohmic heating (ηj^2) can be minimized with a curl-free current distribution ($\nabla \times \mathbf{j} = 0$).

Using 1-D models, King[17] attempted to relate the terminal characteristics, such as voltage, specific impulse, and thrust efficiency, to the total current, mass flow rate, and geometry of self-field coaxial MPDTs. It was determined that decreasing the anode radius and increasing the electrode length precluded the occurrence of large Hall parameters and thus delayed the onset of voltage oscillations (alluded to in §1.3). By relating the thermodynamics of energy addition to relevant plasmadynamic quantities, this model predicted an upper bound of $\sim 70\%$ for the thrust efficiency, at large magnetic Reynolds' numbers.

Though these analytical investigations have elucidated the crucial issues, they provide no assistance in prescribing precise guidelines for design. For instance, they do not attempt to *predict* the current distribution patterns (and thus Ohmic heating terms) for a given geometry and operating condition. This is because the task of assessing the energy deposition into various modes of the plasma in an accelerator requires detailed knowledge of the electromagnetic fields, the gasdynamic flow fields, and the thermodynamic state of the plasma. The difficulty of the task is further magnified by the complex non-equilibrium nature and non-ideal equation-of-state of the working fluid[17]. Therefore, any investigation neglecting these complexities is reduced to a "black box" or a terminal analysis of the accelerator[10].

To overcome these limitations, it is apparent that a comprehensive, time-dependent, multi-dimensional treatment of the plasma flow is required. Such a model, with appropriate descriptions of transport and non-equilibrium effects, will be described in the subsequent section.

2.3   Multidimensional Time-Dependent Model

The governing equations of conservation of mass, momentum, energy, and magnetic flux will be derived in this section. Much of the discussion in this section is based on refs.[78, 79, 74].

2.3.1   Conservation of Mass

If the plasma were to be treated as a single fluid, the global continuity equation for the plasma can be written as,

$$\frac{\partial \rho}{\partial t} + \nabla \cdot (\rho \mathbf{u}) = 0 \,, \tag{2.11}$$

where ρ is the mass-averaged density. Note that there are no source/sink terms because the average density is not affected by ionization/recombination reactions.

However, the electrons are created and destroyed in ionization/recombination reactions, and

they obey a different continuity relation,

$$\frac{\partial \rho_e}{\partial t} + \nabla \cdot (\rho_e \mathbf{u}_e) = m_e \dot{n}_e, \tag{2.12}$$

where ρ_e is the density of the electron fluid, $\dot{n}_e$ is the net ionization/recombination rate, and the electron velocity is $\mathbf{u}_e = \mathbf{u} - \mathbf{j}/en_e$.

The adapted models for ionization and recombination will be described in §2.3.8.

2.3.2   Conservation of Momentum

The relation for conservation of momentum of the plasma is analogous to the Navier-Stokes momentum equation, with an external body force acting on the fluid:

$$\frac{\partial \rho \mathbf{u}}{\partial t} + \nabla \cdot (\rho \mathbf{u}\mathbf{u} + \bar{\bar{p}}) = \nabla \cdot \bar{\bar{\tau}}_{\text{vis}} + \mathbf{f}_{\text{ext}} ,$$

where, in the case under consideration, the external force is the Lorentz force, $\mathbf{f}_{\text{ext}} = \mathbf{j} \times \mathbf{B}$, per unit volume of the plasma.

Using the vector identities eqns. (C.1), (C.2), and (C.3), along with the definition of the Maxwell stress tensor,

$$\bar{\bar{\mathcal{B}}}_M = \frac{1}{\mu_o} \left[\mathbf{B}\mathbf{B} - \frac{B^2}{2}\bar{\bar{\mathcal{I}}} \right] , \tag{2.13}$$

the conservation of momentum can be rewritten as:

$$\frac{\partial \rho \mathbf{u}}{\partial t} + \nabla \cdot \left(\rho \mathbf{u}\mathbf{u} + \bar{\bar{p}} - \bar{\bar{\mathcal{B}}}_M \right) = \nabla \cdot \bar{\bar{\tau}}_{vis} + \mathbf{B} \left(\nabla \cdot \mathbf{B} \right) . \tag{2.14}$$

In a self-field MPDT, the inertial term (ρu^2) is typically $\mathcal{O}\left(10^4\right)$ Pa, the thermodynamic pressure is typically $\mathcal{O}\left(10^3\right)$ Pa, and the magnetic pressure is typically $\mathcal{O}\left(10^4\right)$ Pa.

Although the Maxwell's equations prescribe that $\nabla \cdot \mathbf{B} = 0$, terms involving this quantity are retained in the present treatment for a numerical reason to be explained in §2.3.10.

The importance of viscous effects in plasma thruster flows is still an open question, although it is known to depend on the overall geometry. Viscosity tends to complicate the discharge physics

by reducing the back EMF, which alters the current distribution in the channel. This, in turn, redistributes the local Ohmic dissipation, which affects the local temperature, which in turn changes the coefficient of viscosity. Wolff[22] attributed the unexpectedly low values of thrust from geometries with long electrodes to the detrimental effects of viscous drag. Niewood[30] partly attributes the high observed ion temperatures to viscous heating. Mikellides *et al.*[80, 81] suggest that viscous effects are important in *applied-field* MPDTs. On the other hand, DiCapua[10] and Villani[18] have shown from order-of-magnitude analysis that viscous dissipation is probably a second order effect with little effect on the performance. For a fully ionized plasma, the coefficient of viscosity (with ions being the primary contributors) is (cf. ref.[78]),

$$\mu_{vis} = 0.27 \frac{(4\pi\epsilon_o)^2 \sqrt{M} (k_B T)^{5/2}}{Z^2 e^4 \ln \Lambda}. \tag{2.15}$$

In the temperature range of interest to plasma propulsion (1-10 eV), it can be verified that $\mu_{vis} \leq 10^{-5}$kg/m.s, and consequently, the total viscous drag is $\sim \mathcal{O}$ (0.01 - 0.1) N at normal operating conditions of a thruster. Heimerdinger[29] examined the strong variation of the coefficient of viscosity with temperature and concluded that it is indeed important in certain regimes, though the effect on the overall characteristics is small. However, it is important to note that none of the aforementioned theories and predictions has ever been empirically verified in high-power self-field plasma thrusters. For now, viscous effects will be ignored during the applications of this model, though they can be easily included in the general formulation of the physical model if deemed relevant.

All the preceding discussions had an implicit assumption that all the heavy species (ions of various stages of ionization and neutrals) can be treated as a single fluid. However, it is important to realize that the momentum of the neutrals is not affected by electromagnetic forces, but only by collisions with ions. Under extreme conditions of very low densities and very high magnetic fields, ion-neutral collisions may become sufficiently rare that the ions traverse the accelerator channel or achieve cycloidal drift of their own, without interacting with the neutrals. This condition is

referred to as *ion slip*; if severe, as explained in ref.[2], ion slip could lead to an uncoupling of the electromagnetic processes from the gasdynamics, resulting in an inefficient thruster. However, for the conditions of interest here, both the ionization fraction and the collision frequencies are high enough to warrant neglecting ion slip. Further discussion of this issue will appear in §2.3.3.

2.3.3 Faraday's Law

The relevant equation to determine the magnetic field evolution is Faraday's law:

$$\frac{\partial \mathbf{B}}{\partial t} = -\nabla \times \mathbf{E} \ . \tag{2.16}$$

In a collisionless plasma, the particles will be frozen to the magnetic field lines, and the induced EMF will cancel out the electric field. However, in the presence of collisions, the particles slip away from the field lines, and the electric field in the reference frame of the plasma is finite.

The electric field can be determined from the electron momentum equation,

$$\rho_e \left[\frac{\partial \mathbf{u}_e}{\partial t} + (\mathbf{u}_e \cdot \nabla) \mathbf{u}_e \right] + \nabla p_e = -en \left\{ \mathbf{E} + (\mathbf{u}_e \times \mathbf{B}) \right\} + \sum_s m_e n \nu_{es} \left(\mathbf{u}_s - \mathbf{u}_e \right) \ , \tag{2.17}$$

where ν_{es} is the collision frequency between electrons with species *s*. Collisions among electrons do not contribute to this because the momentum of any interacting pair of electrons is conserved and thus the total electric current carried by the pair is preserved (cf. ref.[82]). For the case in consideration, with effective ionization fraction $Z \simeq 1$, the electron-ion collisions are far more important than electron-neutral collisions.

Using the relation $\mathbf{u}_e = \mathbf{u} - (\mathbf{j}/en_e)$, and ignoring the electron inertial terms, the resulting relation, call the generalized *Ohm's law*, takes the form:

$$\mathbf{E}' = \mathbf{E} + (\mathbf{u} \times \mathbf{B}) = \eta \mathbf{j} + \frac{(\mathbf{j} \times \mathbf{B}) - \nabla p_e}{en_e} \ , \tag{2.18}$$

where the resistivity is,

$$\eta = \frac{m_e \sum_s \nu_{es}}{n_e e^2} \ . \tag{2.19}$$

23

Calculation of classical transport coefficients requires estimation of momentum transfer during elastic collisions. The energy-weighted average of the momentum transfer collision frequency between the electrons and species s, is (cf. refs.[78, 65]),

$$\nu_{es} = n_s Q_{es} \sqrt{\frac{8k_B T_e}{\pi m_e}} . \tag{2.20}$$

Where Q is the cross section for collision. If the species in consideration is an ion of ionization level Z_s, and the average ionization level of that region of space is Z, then,

$$Q_{es} = \frac{\pi}{4} \left(\frac{Z_s e^2}{4\pi\epsilon_o k_B T_e} \right)^2 \ln \left(1 + \frac{144\pi^2 \left(\epsilon_o k_B T_e\right)^3}{n_e e^6 Z^2 \left(Z+1\right)} \right) . \tag{2.21}$$

The electron-neutral collision cross section for argon is taken to be $Q_{eo} \simeq 4.0 \times 10^{-20} \mathrm{m}^2$, and the ion-neutral collision cross section is $Q_{io} \simeq 1.4 \times 10^{-18} \mathrm{m}^2$ for conditions of interest here (cf. ref.[83]). The ion-ion collision frequency is estimated as (cf. [78])

$$Q_{ii} = \frac{5.845 \times 10^{-10}}{T_h^2} \ln \left(1.239 \times 10^7 \sqrt{\frac{T_h^3}{n_e}} \right) . \tag{2.22}$$

The collision cross sections and the collision frequencies are shown in figs.(2.1 & 2.2), respectively, for argon and lithium plasmas.

In the 1-3 eV temperature range of interest to propulsive plasma flows, the typical value of resistivity is, $\mathcal{O}\left(10^{-3} - 10^{-4}\right)$Ohm.m, as shown in Fig.2.3.

Under these circumstances, the magnetic Reynolds' number, $R_m = \mu_o u L / \eta$, which can be viewed as an estimate of the relative importance of back EMF to resistive voltage drop, is $\mathcal{O}\left(1\right)$. This implies that an ideal MHD treatment is not acceptable for these situations.

The Hall effect, which induces current conduction normal to the magnetic field and the applied electric field, can be ignored if the gyro-frequency is much smaller than collision frequency. However, for electrons, the primary current carriers, this ratio, the *electron Hall parameter*, is,

$$\Omega_e = \frac{\omega_{c,e}}{\sum_s \nu_{es}} \sim \mathcal{O}\left(1\right) . \tag{2.23}$$

24
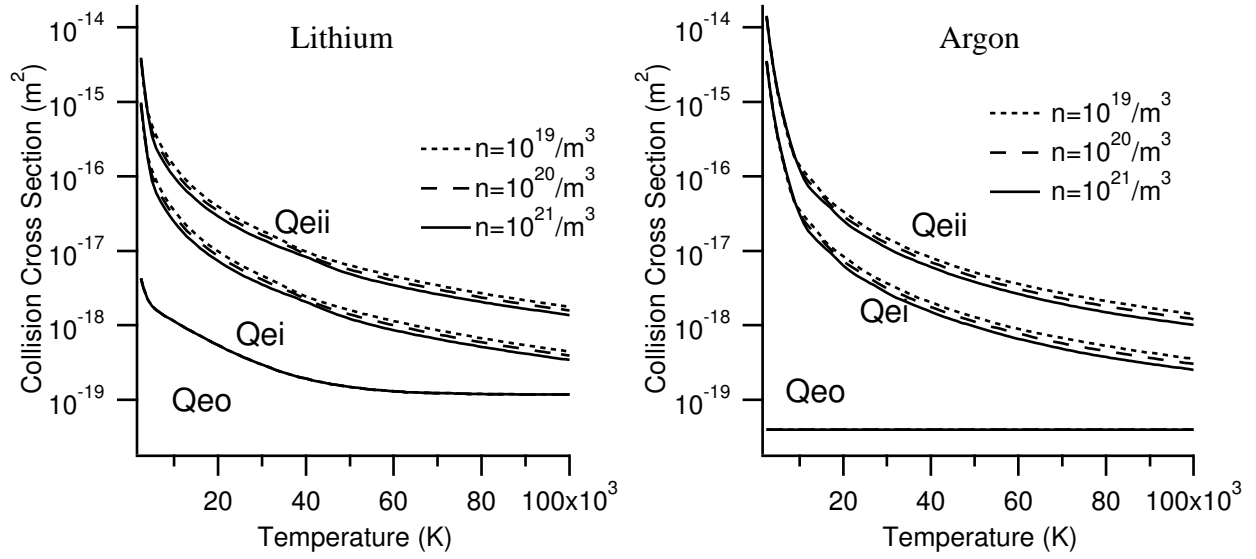
Figure 2.1: Variation of electron collision cross sections with temperature, for lithium and argon.

Therefore, the Hall effect must be included in the Ohm's law (eqn.(2.18)).

As mentioned in §2.3.2, there could be an ion slip contribution to the current. This can be estimated to be,

$$\mathbf{j_{ion}} = (1 - \alpha)^2 \, \frac{\Omega_e \Omega_i}{B^2} \left\{ (\mathbf{j} \times \mathbf{B}) \times \mathbf{B} \right\} , \qquad (2.24)$$

where Ω_e and Ω_i are the electron and ion Hall parameters respectively, $\alpha = n_i/(n_A + n_i)$ is the fractional degree of ionization ($0 \leq \alpha \leq 1$). In the ionization model adapted later, the ionization fraction $\alpha \simeq 1$. For the cases considered here, $\Omega_e \sim \mathcal{O}(1)$. The ratio of ion to electron Hall parameters is then

$$\frac{\Omega_i}{\Omega_e} \simeq \sqrt{\frac{m_e}{M_i}} \sim \mathcal{O}\left(10^{-2}\right) . \qquad (2.25)$$

Therefore, the ion slip effect is small and can be neglected in the present discussion.

The Hall effect causes the resistivity to be anisotropic, as shown in the appendix §C.2. So, Faraday's law (without ∇p_e) can be written as,

$$\frac{\partial \mathbf{B}}{\partial t} = - \left[\nabla \times \left\{ (\bar{\bar{\eta}} \cdot \mathbf{j}) - (\mathbf{u} \times \mathbf{B}) \right\} \right] . \qquad (2.26)$$

25
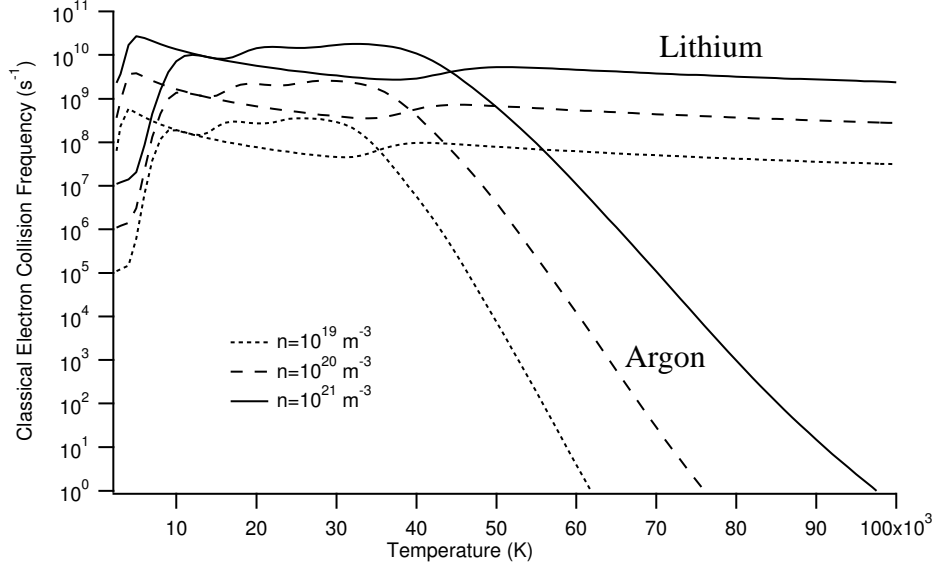
Figure 2.2: Variation of electron collision frequency with temperature, for lithium and argon.

The convective diffusion can be written, using eqns. (C.4) and (C.2) from the appendix, as the divergence of a tensor. Maintaining the same formulation, the resistive diffusion can also be written as the divergence of a tensor, using some manipulations shown in §C.2 in the appendix. Thus, the relation for the evolution of magnetic field takes the form,

$$\frac{\partial \mathbf{B}}{\partial t} + \nabla \cdot (\mathbf{uB} - \mathbf{Bu}) = \nabla \cdot \bar{\bar{E}}_{res} + \mathbf{u}\left(\nabla \cdot \mathbf{B}\right) \ . \tag{2.27}$$

2.3.4 Conservation of Energy

The Navier-Stokes relation for the conservation of gasdynamic energy density,

$$\mathcal{E}_g = \frac{p}{\gamma - 1} + \frac{1}{2}\rho \mathbf{u} \cdot \mathbf{u} \ , \tag{2.28}$$

can be written as,

$$\frac{\partial \mathcal{E}_g}{\partial t} + \nabla \cdot \left[\left(\mathcal{E}_g + p\right)\mathbf{u}\right] = \nabla \cdot \left(\bar{\bar{\tau}}_{vis} \cdot \mathbf{u}\right) + \nabla \cdot \left(k_{th}\nabla T\right) + \dot{q} \ , \tag{2.29}$$

where,

26
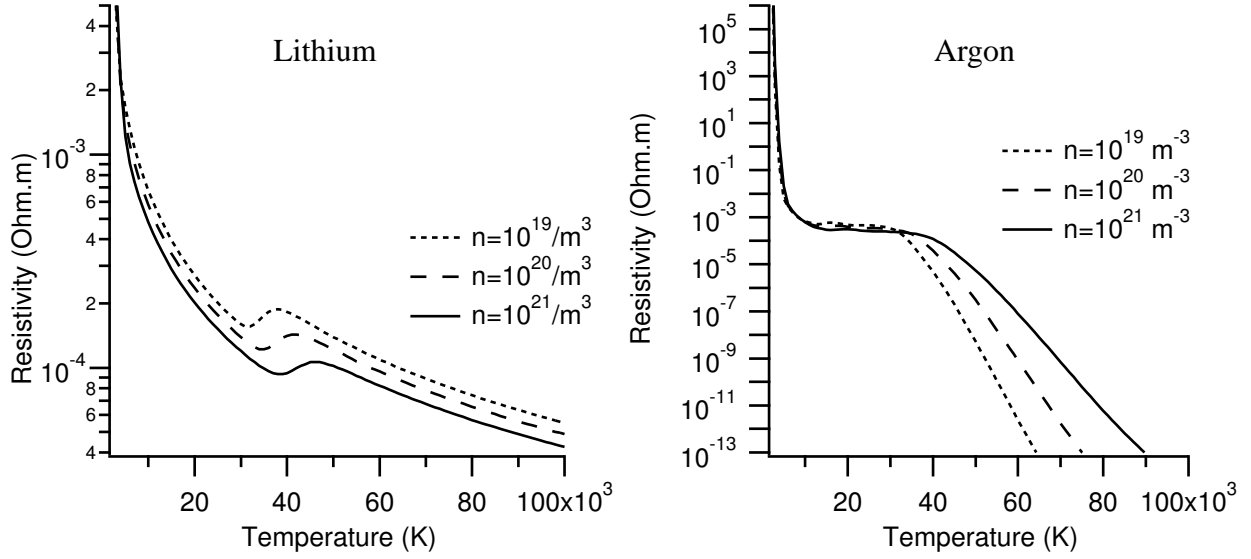
Figure 2.3: Variation of resistivity with temperature, for lithium and argon.

$\frac{\partial \mathcal{E}_g}{\partial t}$ = rate of change of the energy density,

$\left(\frac{\rho u^2}{2}\right)\mathbf{u}$ = convective flux of kinetic energy,

γ = ratio of specific heats,

$\frac{\gamma p}{\gamma - 1}\mathbf{u}$ = convective flux of internal/thermal energy,

$\bar{\bar{\tau}}_{vis} \cdot \mathbf{u}$ = viscous heat transfer,

$k_{th}\nabla T$ = thermal conduction,

$\dot{q}$ = external energy source/sink.

For a typical MPDT plasma, the gasdynamic energy density is $\mathcal{O}\left(10^4\right)$ J/m^3. This is partitioned between the kinetic energy and the internal energy, and their ratio is a function of Mach number squared (kinetic energy/internal energy $\sim v^2/T \sim (v/a)^2 \sim M^2$).

For reasons explained in §2.13, the viscous dissipation of energy can be assumed to be negligible. Globally, the thermal conduction can be shown to be small compared to the dominant terms. However, in the presence of strong thermal gradients, and in regions where convective heat transfer

27

is small, thermal conduction can be significant and therefore has to be included in the model.

The external source is clearly the electrical power input per unit volume, $\dot{q} = \mathbf{j} \cdot \mathbf{E}$. Using Faraday's law, Ampère's law without the displacement current, and the vector identity:

$$
\begin{aligned}
\nabla \cdot (\mathbf{E} \times \mathbf{B}) &= \mathbf{B} \cdot (\nabla \times \mathbf{E}) - \mathbf{E} \cdot (\nabla \times \mathbf{B}) \\
&= -\frac{\partial}{\partial t} (B^2/2) - \mu_o (\mathbf{j} \cdot \mathbf{E}) \ ,
\end{aligned}
$$

the power input to the plasma can then be written as:

$$
\mathbf{j} \cdot \mathbf{E} = - \left[\frac{\partial}{\partial t} \left(B^2/2\mu_o \right) + \nabla \cdot \frac{(\mathbf{E} \times \mathbf{B})}{\mu_o} \right] . \tag{2.30}
$$

The first term can be identified as the rate of change of energy density in the magnetic field, and the second term is the Poynting flux of electromagnetic energy. Defining the magnetogasdynamic total energy density (gasdynamic energy density + energy density in magnetic field)

$$
\mathcal{E} = \mathcal{E}_g + \frac{B^2}{2\mu_o} = \frac{p}{\gamma - 1} + \frac{1}{2}\rho u^2 + \frac{B^2}{2\mu_o}, \tag{2.31}
$$

the conservation of total energy density of the plasma can be written as:

$$
\frac{\partial \mathcal{E}}{\partial t} + \nabla \cdot \left[(\mathcal{E} + p) \, \mathbf{u} - \bar{\bar{\mathcal{B}}}_M \cdot \mathbf{u} \right] = \nabla \cdot \left[\frac{-\mathbf{E}' \times \mathbf{B}}{\mu_o} + k_{th} \nabla T \right] + \left(\frac{\mathbf{B}}{\mu_o} \cdot \mathbf{u} \right) (\nabla \cdot \mathbf{B}) \ ,
$$

where the contribution of the back EMF ($\bar{\bar{\mathcal{B}}}_M \cdot \mathbf{u}$) and resistive drop to the electric field (in the Poynting flux term) have been separated to emphasize the energy expended in acceleration and in heating, respectively.

Under some physical conditions, (for instance, when the magnetic pressure is several orders of magnitude larger than thermodynamic pressure) the conservation form of the energy equation may not be suitable. In these cases, since p is calculated from subtraction of one large number ($B^2/2\mu_o$) from another ($\mathcal{E}$), the associated numerical errors could be large. However, for the conditions that are of interest to plasma propulsion, thermodynamic pressure is seldom two orders of magnitude lesser than the magnetic pressure ($\beta = p/p_m > 10^{-2}$), and there is generally no need to worry

28

about such errors. Thus the conservation form of the energy equation is, in general, numerically suitable here.

In order to treat the fluid as if it were in thermal equilibrium, the characteristic residence time scale should be much larger than the time scale for energy equilibration between electrons and ions. For MPDT plasmas this ratio is,

$$\frac{\tau_{\text{res}}}{\tau_{\text{equi}}} \sim \mathcal{O}\left(10\right) \ . \tag{2.32}$$

Since this condition is not strongly satisfied, it may be important to treat the electrons and ions as separate fluids with separate temperatures. In fact, there is sufficient experimental evidence[14, 12] that this is indeed the case, though the disparity is less than an order of magnitude. This suggests that the temperature of the individual species can be obtained by subtracting the energy of other components from the total energy. In order to do so, some rearrangements are necessary. The definition of the fluid energy density, eqn.(2.28), has to be split into the internal energy density and the kinetic energy density:

$$\mathcal{E}_g = \mathcal{E}_{int} + \mathcal{E}_{KE} \ . \tag{2.33}$$

With this definition, the conservation relation for the internal energy takes the form:

$$\frac{\partial \mathcal{E}_{int}}{\partial t} + \nabla \cdot \left[\mathcal{E}_{int}\mathbf{u}\right] + p\nabla \cdot \mathbf{u} = \eta j^2 + \nabla \cdot \left(k_{th}\nabla T\right) \ . \tag{2.34}$$

The internal energy of the fluid can be further split into those pertaining to electrons and ions,

$$\mathcal{E}_{int} = \mathcal{E}_i + \mathcal{E}_e \ . \tag{2.35}$$

The thermal conductivity in the total energy equation is the sum of the contributions from both electrons and ions,

$$k_{th}\nabla T = \left(k_{th,e}\nabla T_e\right) + \left(k_{th,i}\nabla T_h\right) \ . \tag{2.36}$$

From the relation for collision frequency (eqn.(2.20)), the coefficient for electron thermal conductivity can then be estimated as

$$k_{th,e} = 3.20 \frac{k_B^2 n_e T_e}{m_e \sum_s \nu_{es}} \ , \tag{2.37}$$

while that of the ions is

$$k_{th,i} = \sqrt{\frac{\pi k_B^3 T_h}{8 M_i}} \left(\frac{n_i}{n_i Q_{ii} + n_o Q_{io}} \right) \ . \tag{2.38}$$

The electron and ion thermal conductivities are shown in figs.(2.4 & 2.5), respectively, for argon and lithium plasmas. It can be shown[78] that,

$$\frac{k_{th,e}}{k_{th,i}} \simeq \sqrt{\frac{M_i}{m_e}} \sim \mathcal{O}\left(10^2\right) . \tag{2.39}$$

As seen in fig.(2.5), $k_{th,i} \simeq 0.01 - 0.1$ W/K/m, and as seen in fig.(2.4), $k_{th,e} \simeq 1$ W/K/m, in the 1 - 3 eV temperature range. Since the temperatures of electrons and ions are not very disparate, one could make the assumption that thermal conduction of the ions is negligible compared to that of the electrons. However, there may be some regions, such as stagnation points, where thermal conduction may be an important dissipation mechanism for the ions. Moreover, inclusion of ion thermal conduction does not impose additional constraints on the solver. Therefore this term is retained in this model.

With these assumptions, the conservation relations for the internal energy of electrons can be written as,

$$\frac{\partial \mathcal{E}_e}{\partial t} + \nabla \cdot [\mathcal{E}_e \mathbf{u}] + p_e \nabla \cdot \mathbf{u} = \eta j^2 - \Delta \dot{\mathcal{E}}_{ie} + \nabla \cdot (k_{th,e} \nabla T_e) \ , \tag{2.40}$$

and that of ions as,

$$\frac{\partial \mathcal{E}_i}{\partial t} + \nabla \cdot [\mathcal{E}_i \mathbf{u}] + p_i \nabla \cdot \mathbf{u} = \Delta \dot{\mathcal{E}}_{ie} + \nabla \cdot (k_{th,i} \nabla T_h) \ . \tag{2.41}$$

In deriving eqns.(2.40) and (2.41) it was also assumed that Ohmic heating primarily affects the electrons. Note that the energy expended in acceleration, $(\mathbf{j} \times \mathbf{B}) \cdot \mathbf{u}$, does not appear in eqns.(2.34),

30
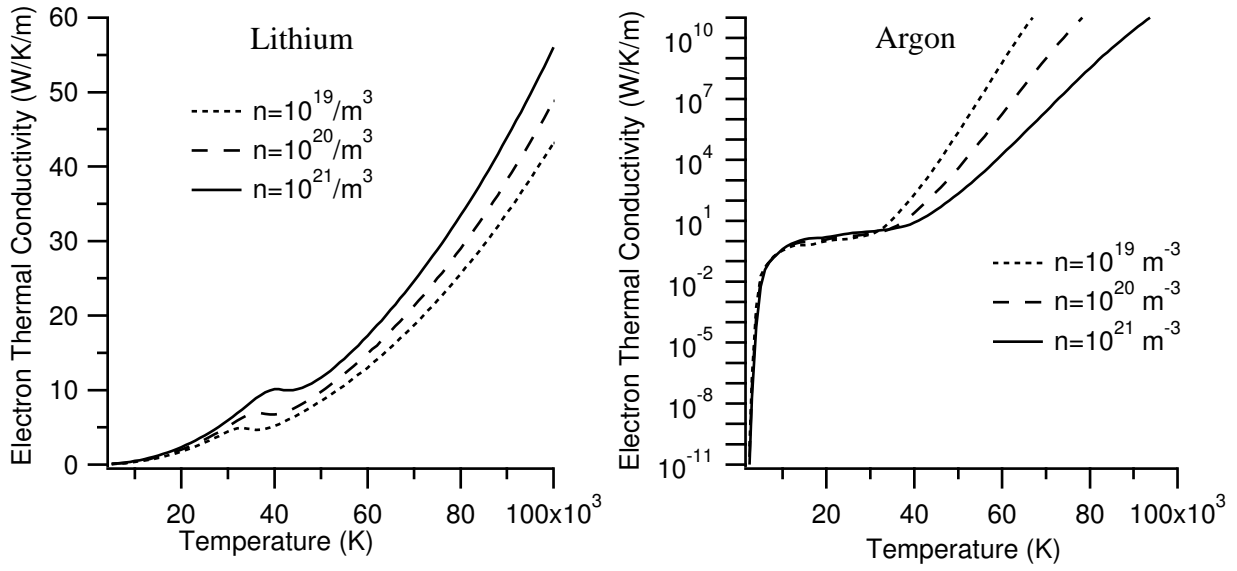
Figure 2.4: Variation of electron thermal conductivity with temperature, for lithium and argon.
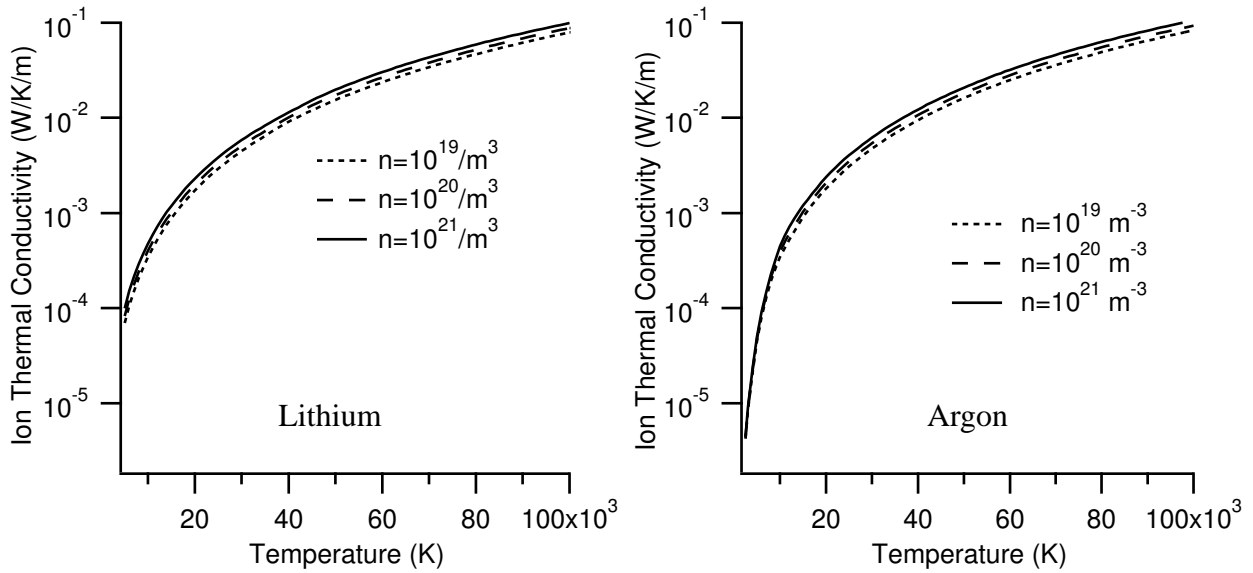
Figure 2.5: Variation of ion thermal conductivity with temperature, for lithium and argon.

31

(2.40) and (2.41) becuase they are relations for the *internal* energy only. The acceleration energy would appear only if the kinetic energy were also included in the definition of energy density.

In eqns.(2.40) and (2.41), the rate of exchange of energy (via collisions) between electrons and ions can be estimated to be[74],

$$\Delta\dot{\mathcal{E}}_{ie} = \frac{3n_e m_e \nu_{ei}}{M_i} k_B \left(T_e - T_h\right) \ . \tag{2.42}$$

2.3.5 Radiation

Energy losses due to radiation are important in many types of plasmas. As explained by LeVeque *et al.*[84], the energy lost by radiation, per unit time, per unit volume, can be captured as a sink term to the right hand side of eqn.(2.29). In this case,

$$\dot{q}_r = -n_e n_i L(T_e), \tag{2.43}$$

where $L(T_e)$ is obtained empirically. For lithium plasma, $L(T_e)$ was obtained from ref.[85], and is shown in fig.(2.6).

However, earlier experimental work by Boyle[14], Villani[18], and Bruckner[12] on argon-fed MPDTs suggest that the relative magnitude of this sink is not significant for the MPDT plasma. As will be shown in §4.2.4, the highest observed emission in the MPDT is from a thin shell around the cathode (dubbed as the "cathode barrel"). Even in this region, the power loss by radiation is only $\dot{q}_r < 10^7 \text{W/m}^3$, whereas the Ohmic heating is typically $\dot{q} = \eta j^2 \sim 10^9 \text{W/m}^3$, indicating that radiation accounts for only 1% of the energetics of that region. This radiation loss model (eqn.(2.43)) was implemented for the LiLFA calculations (§5), and its effect on the solution was confirmed to be insignificant.
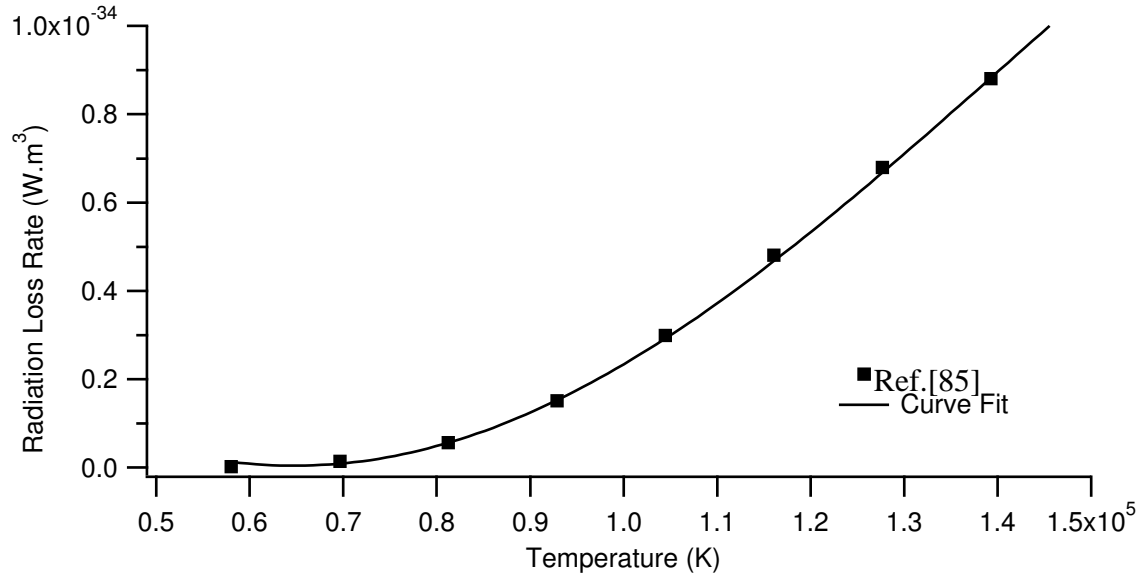
Figure 2.6: Energy loss rate by radiation for lithium (from ref.[85]).

2.3.6 Equation of State

For a system with N structureless molecules in thermal equilibrium at a temperature T, moving freely in a volume V, the pressure is given by the ideal gas law. However, real molecules are not structureless, but possess energy in modes other than translational motion. Furthermore, their motion may be influenced by potentials of the neighboring molecules. In these situations, the relationship between pressure, density and temperature is of the form,

$$p = Nk_BT\frac{\partial \ln Q}{\partial V} \; . \tag{2.44}$$

Ignoring nuclear contributions, the total partition function, Q can be written as,

$$Q = Q_{rot}Q_{vib}Q_{tr}Q_{el} \; , \tag{2.45}$$

where Q_{rot} is the contribution of rotational energy levels, Q_{vib} that of the vibrational energy levels, and Q_{el} that of the electronic energy levels.

The calculation of the translation partition function for non-interacting particles is relatively

33
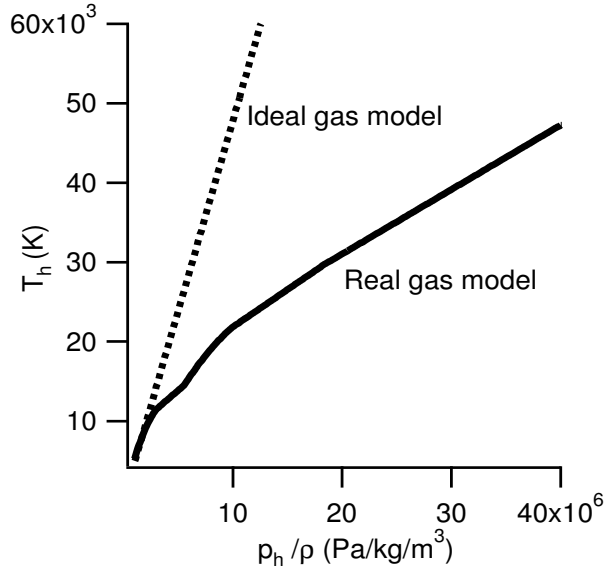
Figure 2.7: Deviation from ideal gas behavior for argon (calculated from data in ref.[87])

straightforward and is found to be (cf. ref.[86]), ,

$$Q_{tr} = V \left(\frac{2\pi M_i k_B T}{h^2} \right)^{3/2} .$$ (2.46)

However, estimating this for *interacting* particles is a nontrivial task. For argon, this information was obtained from ref.[87]. Based on it, King[17] and Choueiri[88] have derived expressions to obtain the temperature from pressure and density. As shown in Fig.(2.7), it is clear that at temperatures at or above 10^4K, the deviations from the ideal gas model are significant. This relation for the equation of state will be used in the current model, and further details can be found in the appendix. For lithium, it is known[89, 90, 91, 92] for very high density and/or very high temperature situations, but not for the parameters of interest to propulsive plasmas. Therefore, this model currently uses eqn.(2.46) for lithium plasmas, though its validity has yet to be assessed.

As energy is deposited into the internal modes, the ratio of specific heats also changes. This can be estimated using the internal energy partition function. Fortunately, most of the propellants of interest to plasma propulsion (Li, Ar, and Xe) are monatomic in nature, and therefore, the

34

rotational and vibrational contributions are absent in the internal energy partition function. Thus the problem of finding the equation of state of a real gas reduces to the problem of estimating the electronic excitation partition function Q_{el}. Even this is very difficult to compute for atoms with multiple electronic levels. Fortunately, this information can be found for many elements of interest in references such as ref.[87]. Information from ref.[87] was used to compute the ratio of specific heats for argon. Q_{el} for lithium is simple enough to computed from first principles. The electronic energy levels for lithium, obtained from ref.[93, 94], are given Table 2.1. Using these, the electronic energy partition function can be calculated as,

$$Q_{el} = \sum_i g_i \, e^{-\epsilon_i/k_B T_e}. \tag{2.47}$$

Then,

$$Q_{\text{tot}} = Q_{tr} Q_{el}. \tag{2.48}$$

Using this, the internal energy per unit volume, $\mathcal{E}$, can be computed,

$$\mathcal{E} = n k_B T^2 \frac{\partial \ln Q_{\text{tot}}}{\partial T}. \tag{2.49}$$

Using the definition of specific enthalpy,

$$h \equiv \mathcal{E} + p, \tag{2.50}$$

the specific heats can then be calculated using their standard definitions,

$$c_p \equiv \frac{\partial h}{\partial T}, \tag{2.51}$$

and

$$c_v \equiv \frac{\partial \mathcal{E}}{\partial T}. \tag{2.52}$$

Armed with these parameters, the ratio of specific heats can be calculated as,

$$\gamma \equiv \frac{c_p}{c_v}. \tag{2.53}$$
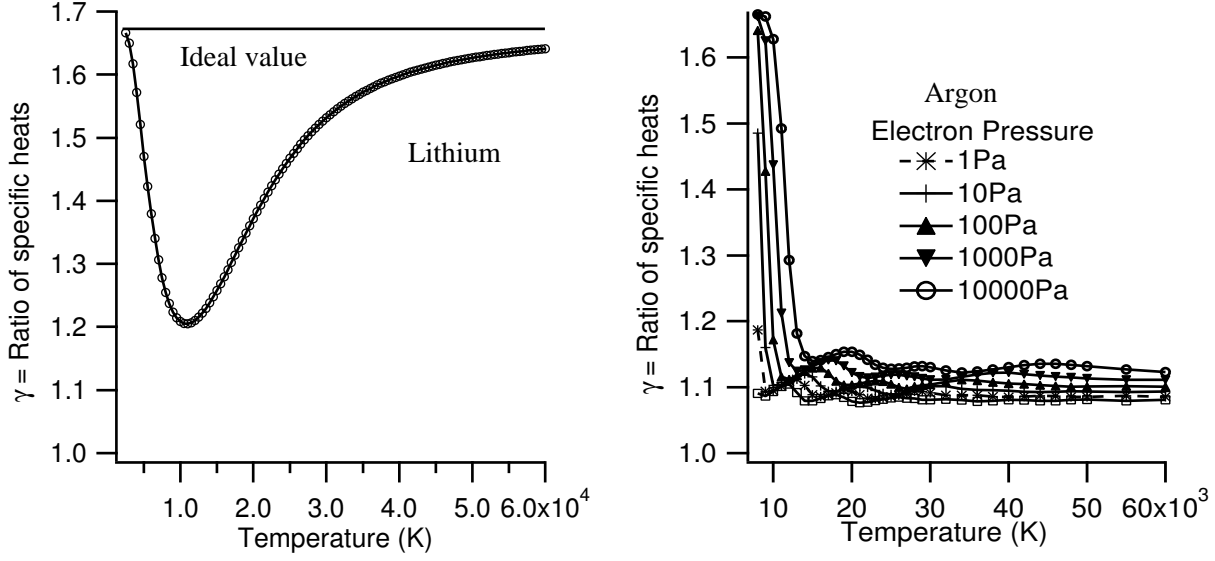
Figure 2.8: Variation of the ratio of specific heats for lithium and argon.

For argon, information for eqns.(2.47-2.50) was obtained from ref.[87], and for lithium eqns.(2.47)-(2.53) were calculated from first principles. The resulting ratios of specific heats are shown in Fig.(2.8). As the temperature increases, progressively more electronic energy levels become accessible, and consequently γ continues to drop ($\gamma = 1$ is the isothermal case in which an infinite number of internal energy states are available to absorb energy without raising the temperature). For argon, the deviation from the ideal value of $5/3$ is severe at temperatures above 10^4K. In contrast, lithium's ratio of specific heats quickly reverts to its ideal value of 5/3 because the gap between the first and second ionization potentials (5.39 eV and 75.62 eV) is very large. This fact may be significant for propulsive applications; as discussed in §2.2 and in ref.[10], much of the power in an argon MPDT exhaust is in internal modes, and is not easily recovered (hence known as "frozen flow"); but for lithium, this energy is in thermal energy, which can potentially be recovered as directed kinetic energy.

36

2.3.7 Anomalous Transport

It is known that current can drive microinstabilities in a collisional and finite-β magnetized plasma[95] such as those in MPDTs/LFAs. The presence of current-driven microinstabilities - generalized lower hybrid drift instability (GLHDI) and electron cyclotron drift instability (ECDI) - in such accelerator plasmas has been established experimentally in the plasma of the MPDT at both low and high power levels[96, 97]. Exchange of momentum between particles and waves induced by these microinstabilities gives rise to enhanced values of transport properties (hence the term anomalous transport), and substantially increases energy dissipation and adversely impacts the efficiency of a thruster.

Choueiri[58] has developed a model to estimate the resulting anomalous transport and heating in terms of macroscopic parameters. Under this formulation, apart from the classical collision frequency of the particles, there exist additional momentum and energy-transferring collisions between particles and waves. The resulting anomalous collision frequency is important whenever the ratio of electron drift velocity to ion thermal velocity,

$$\frac{u_{de}}{v_{ti}} = \frac{j}{en_e} \sqrt{\frac{M_i}{2k_B T_h}} \geq 1.5 \; . \tag{2.54}$$

Above this threshold, the ratio of anomalous collision frequency to classical collision frequency was found to depend on the classical electron Hall parameter, Ω_e, and the ratio of ion to electron temperatures, T_h/T_e. Polynomials giving these relations were derived in ref.[58] to be,

$$\begin{aligned}
\frac{\nu_{e,\text{an}}}{\nu_{e,\text{cl}}} = \; & \{0.192 + 3.33 \times 10^{-2}\Omega_e + 0.212\Omega_e^2 - 8.27 \times 10^{-5}\Omega_e^3\} \\
& + \tfrac{T_h}{T_e} \{1.23 \times 10^{-3} - 1.58 \times 10^{-2}\Omega_e - 7.89 \times 10^{-3}\Omega_e^3\} \; ,
\end{aligned}$$

and are shown in Fig.(2.9). It was shown in ref.[95] that this relationship is insensitive to the ion mass, and therefore it will be used in this work for both lithium and argon. As a result, the effective resistivity of the plasma is,

$$\eta_{\text{eff}} = \frac{m_e \left(\nu_{e,\text{cl}} + \nu_{e,\text{an}} \right)}{e^2 n_e} \; . \tag{2.55}$$

37
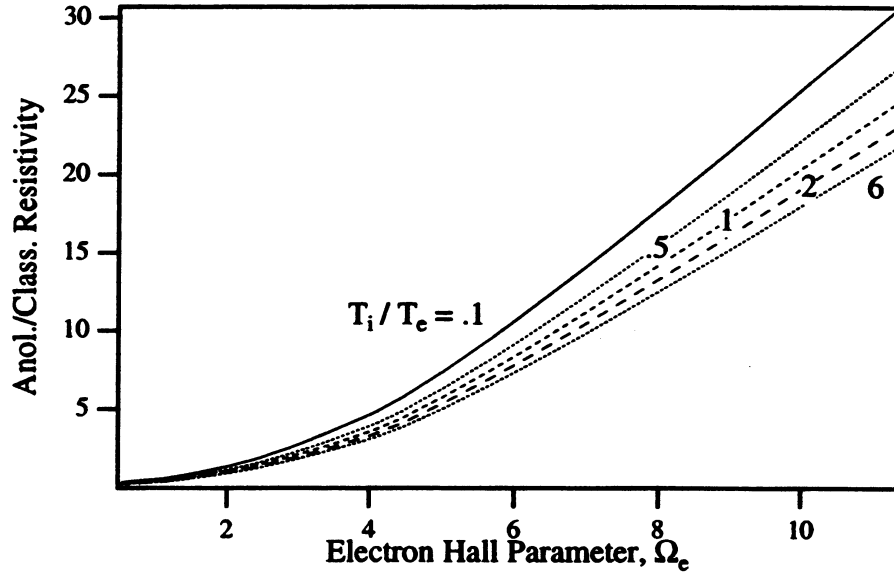
Figure 2.9: Ratio of anomalous to classical resistivity in argon plasmas (from ref.[58])

2.3.8 Ionization Processes

It is imperative that, within the acceleration region, a significant fraction of the working fluid remains in a state of ionization, as the free charges are responsible for carrying current, and thereby establishing the electromagnetic fields required for acceleration[2]. The plasma in a self-field, quasi-steady MPDT is generally in a state of ionizational nonequilibrium [31]. The reaction rates for ionization reactions must account for transitions from the ground states, as well as those from excited states. Though some numerical simulations (such as refs.[30]) have used finite-rate ionization models, they do not include higher levels of ionization that have been observed experimentally [12, 98]. There are indications[60] that, for the conditions of interest to MPD plasmas, the solution of flow fields using the seemingly restrictive assumption of equilibrium ionization may yield results that are sufficiently close to reality.

In equilibrium, irrespective of the manner in which the species are created, the densities of the

electrons, n_e, ions, n_i, and the neutrals , n_o, are related by the Saha[99] equation,

$$\frac{n_i n_e}{n_{i-1}} = \frac{2 \left(2\pi m_e k_B T\right)^{3/2}}{h^3} \frac{\sum_l g_l^i \, e^{-\epsilon_l^i/k_B T}}{\sum_l g_l^{i-1} \, e^{-\epsilon_l^{i-1}/k_B T}} = K_i \, , \qquad (2.56)$$

where ϵ_l^i is the lth energy level of the species of ionization level i, and g_l^i is the corresponding statistical weight.

Similar expressions can be written for higher ionization levels, with the energy levels scaled to a common ground. The propellants considered in this work are lithium and argon. Lithium's first and second ionization potentials are 5.39 eV and 75.62 eV respectively. The relevant energy levels of lithium atom, its ions, and their statistical weights are given in Table (2.1), and they have to be adjusted to the ionization potentials given above. Argon's first, second and third ionization potentials are 15.755 eV, 27.63 eV, and 40.90 eV respectively. The relevant energy levels of argon atom, its ions, and their statistical weights are given in Table (2.2), and they have to be adjusted to the ionization potentials given above.

Even when thermal nonequilibrium exists between electrons and ions, a modified Saha equation can be applicable. As shown in refs.[100] and [101], due to the high mobility of the electrons, the temperature in eqn.(2.56) can be replaced, in such situations, with the temperature of the electron fluid, and the resulting modified Saha equation is an accurate model.

For a model with N levels of ionization, the electron number density can be obtained by finding the single positive root of the polynomial (from Heiermann *et al.*[65]),

$$n_e^{N+1} + \sum_{l=1}^{N} \left[n_e^{N-l} \left(n_e - l n_o\right) \prod_{m=1}^{l} K_m \right] = 0 \, ,$$

where n_o is the total number density of all nuclei, and the equilibrium constant, K_m is from eqn.(2.56).

Li I		Li II		Li III	
E_l^0 (eV)	g_l^0	E_l^+ (eV)	g_l^+	E_l^{++} (eV)	g_l^{++}
0.000	2	0.000	1	0.000	2
1.848	6	59.021	3	91.788	8
3.373	2	60.920	1	108.785	18
3.834	6	61.281	9	1114.735	32
3.879	10	62.216	3		
4.341	12	68.780	3		
4.522	6	69.278	1		
4.541	10	69.368	9		
4.541	14	69.584	15		
4.748	2	69.588	5		
4.837	6	69.647	3		
4.847	24				

Table 2.1: Energy levels and statistical weights in lithium and lithium ions (obtained from ref.[93, 94])

2.3.9 Summary of Governing Equations

The nucleus of this model is the set of single fluid MHD equations. The corresponding conservation laws, given by eqns. (2.11), (2.13), (2.16) and (2.32), can be summarized in the vector form:

$$\frac{\partial}{\partial t}\begin{bmatrix} \rho \\ \rho\mathbf{u} \\ \mathbf{B} \\ \mathcal{E} \end{bmatrix} + \nabla \cdot \begin{bmatrix} \rho\mathbf{u} \\ \rho\mathbf{u}\mathbf{u} + \bar{\bar{p}} - \bar{\bar{\mathcal{B}}}_{\mathcal{M}} \\ \mathbf{u}\mathbf{B} - \mathbf{B}\mathbf{u} \\ (\mathcal{E} + p)\,\mathbf{u} - \bar{\bar{\mathcal{B}}}_{\mathcal{M}} \cdot \mathbf{u} \end{bmatrix} = \nabla \cdot \begin{bmatrix} \mathbf{0} \\ 0 \\ \bar{\bar{E}}_{res} \\ \mathbf{q} \end{bmatrix} . \tag{2.58}$$

Ar I		Ar II		Ar III		Ar IV	
E_l^0 (eV)	g_l^0	E_l^+ (eV)	g_l^+	E_l^{++} (eV)	g_l^{++}	E_l^{+++} (eV)	g_l^{+++}
0.000	1	0.059	6	0.111	29	0.000	4
11.577	8	13.476	2	1.737	6	3.478	16
11.802	4	16.420	20	4.124	2	14.671	24
13.096	24	16.702	12	14.214	6	31.133	24
13.319	12	17.177	6	17.856	1	35.568	40
14.019	48	17.688	28	17.964	10		
14.242	24	18.016	6	19.460	14		
14.509	24	18.300	12	20.066	1		
14.690	12	18.438	10	20.222	8		

Table 2.2: Energy levels and statistical weights in argon and argon ions (obtained from refs. [102, 98, 103])

Under this framework, ancillary relations such as the energy equation for the individual species, which do not fit into the conservation form, are solved separately, without affecting the underlying solver. Notice that the eqns. (2.11), (2.13), (2.16) and (2.32) strictly contain a $\nabla \cdot \mathbf{B}$ term not included in the conservation form given in eqn.(2.58). This is the topic of the next section.

2.3.10 Zero Divergence Constraint

Though it is physically true that $\nabla \cdot \mathbf{B} \equiv 0$, it is often not true numerically, as there may be truncation errors. The treatment of the terms are important, since they could be a cause of numerical instabilities, as explained in ref.[104]. The technique used here, based on the work of Powell[105], has a modified eigensystem (see appendix §D) that accounts for any possible errors in $\nabla \cdot \mathbf{B}$. The
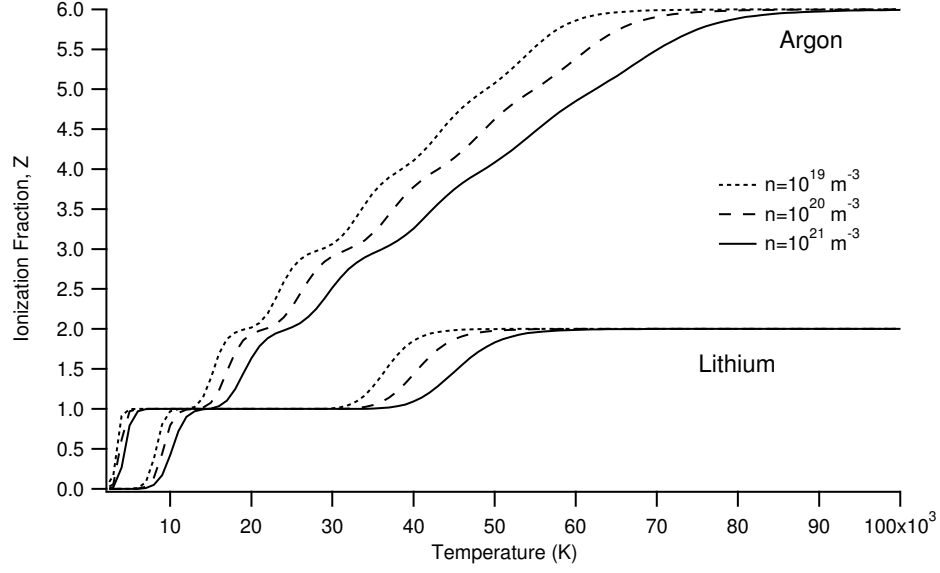
Figure 2.10: Variation of ionization fraction with temperature for lithium and argon.

resulting scheme satisfies the relation,

$$\frac{\partial}{\partial t}\left(\nabla \cdot \mathbf{B}\right) + \nabla \cdot \left[\left(\nabla \cdot \mathbf{B}\right)\mathbf{u}\right] = 0 \ . \tag{2.59}$$

In other words, the numerical scheme used in this work ensures that any artificial source of $\nabla \cdot \mathbf{B}$ is convected out of the domain.

In the case of a self-field accelerator in a coaxial geometry, the magnetic field is purely azimuthal. If the assumption of axisymmetry is made, then

$$\nabla \cdot \mathbf{B} = \frac{1}{r}\frac{\partial B_\theta}{\partial \theta} = 0 \ . \tag{2.60}$$

Therefore, in this work, the divergence of the magnetic field is always zero throughout the domain.

2.4 Summary

In summary, the physical models and the corresponding governing equations that describe MPDT flows were discussed in this chapter. The set of MHD equations, comprising the conservation

relations for mass, momentum, energy and magnetic flux were described. Further improvements to the MHD model, such as the effects of thermal nonequilibrium, anomalous transport effects, along with relations for classical transport, a real equation of state and a multi-level equilibrium ionization model, were also developed in this chapter.

The techniques for obtaining a numerical solution of these governing equations will be discussed in the following chapter.

Chapter 3

NUMERICAL SOLUTION

No knowledge can be certain if it is not based upon mathematics, or upon some other knowledge which is itself based upon the mathematical sciences.

Leonardo da Vinci.

As mentioned in §1.3, despite several earlier efforts to simulate MPDT flows, there remains a need for accurate and robust numerical schemes for this purpose. A new numerical method that has the potential to overcome the problems described in §1.3, will be described in this chapter. First, some fundamental concepts, pertaining to the guiding principles to be used in this thesis, will be reviewed. Then, the characteristics-splitting technique for the solution of the convection equations will be developed and validated. That will be followed by a brief discussion of the well known techniques for the solution of the diffusion equations.

3.1   Guiding Principles

In light of the discussion in §1.3, it is imperative that the numerical scheme developed in this work strictly adheres to the guidelines listed below:

1. Treat the flow and magnetic field equations in a self-consistent manner,

2. Use a conservative formulation of the problem,

3. Use non-oscillatory discontinuity capturing techniques that satisfy Rankine-Hugoniot relations, combined with techniques to limit numerical diffusion and improve spatial accuracy.

The mathematical foundation for the numerical solver used in this work will be described in this chapter.

3.2   Mesh System

The fundamental aspect of a numerical solution obtained using differencing schemes, unlike that of an analytical solution, is that it is defined on a discrete domain instead of a continuous domain. A rigorous treatment of this issue can be found in ref.[106], and only the information directly relevant to the present application will be discussed here. The true domain, $\mathcal{D}$, is divided into small control volumes, Ω_j, whose centers are given by position vectors $\mathbf{c}_j$. Within each of these control volumes, the solution $\mathbf{U}(x, t)$ is approximated by a constant $\mathbf{U}_j(t)$, which should be considered as an approximation of the mean value of $\mathbf{U}$ over the cell Ω_i rather than the value of $\mathbf{U}$ at point $\mathbf{c}_j$,

$$\mathbf{U}_j(t) \cong \frac{1}{|\Omega_i|} \int_{\Omega_i} \mathbf{U}(\mathbf{x}, t) \, d^3\mathbf{x}, \tag{3.1}$$

where $|\Omega_i|$ is the volume of Ω_i.

Given an initial distribution $\mathbf{U}(x, 0)$, and using the definition in eqn.(3.1), the time rate of change of $\mathbf{U}$ inside the control volume can be calculated from the sum of the fluxes through its boundaries,

$$\frac{\partial \mathbf{U}_j(t)}{\partial t} = -\frac{1}{|\Omega_i|} \sum \int_{\Gamma_{ij}} \mathcal{F} \cdot \mathbf{n}_i dA, \tag{3.2}$$

where Γ_{ij} is the boundary between cells Ω_i and Ω_j.

45
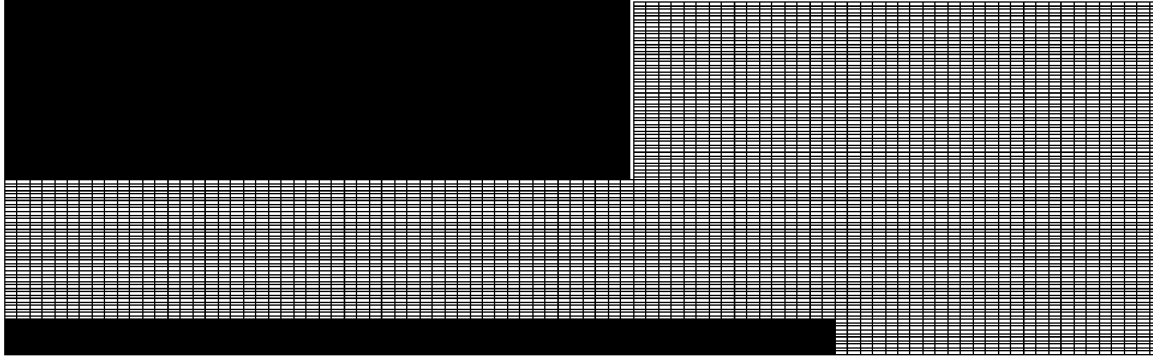
Figure 3.1: Uniform, orthogonal structured grid.

The adjoining issue is the detailed description of the control volumes, their identities, shapes, sizes, and locations. Mesh generation is an entire field of study in itself, and is beyond the scope of this work to get into the intricacies of that trade. Only a brief review that is relevant to the problem at hand will be made.

Generally, cylindrical coordinates are preferable for the study of plasma thrusters. Four distinct techniques of dissecting the domain into control volumes can be identified:

1. Structured, concentric cylindrical shells, separated by lines of constant $\hat{r}$, $\hat{\theta}$ and $\hat{z}$. Combined with the axisymmetric assumption, the control volumes are simply rectangles in the $r - z$ plane (cf. Fig.(3.1)).

2. Structured shells, separated by lines of a constant stream functions, η, ξ that fit the true boundaries as close as possible. Combined with the axisymmetric assumption, the control volumes are quadrilaterals in the $r - z$ plane (cf. Fig.(3.2)).

3. Structured shells, separated by non-orthogonal lines that fit the boundaries (cf. Fig.(3.3)).

4. Unstructured irregular tetrahedrons that fit the complicated boundary exactly. In an axisymmetric case, the control volumes are triangles in the $r - z$ plane (cf. Fig.(3.3)).
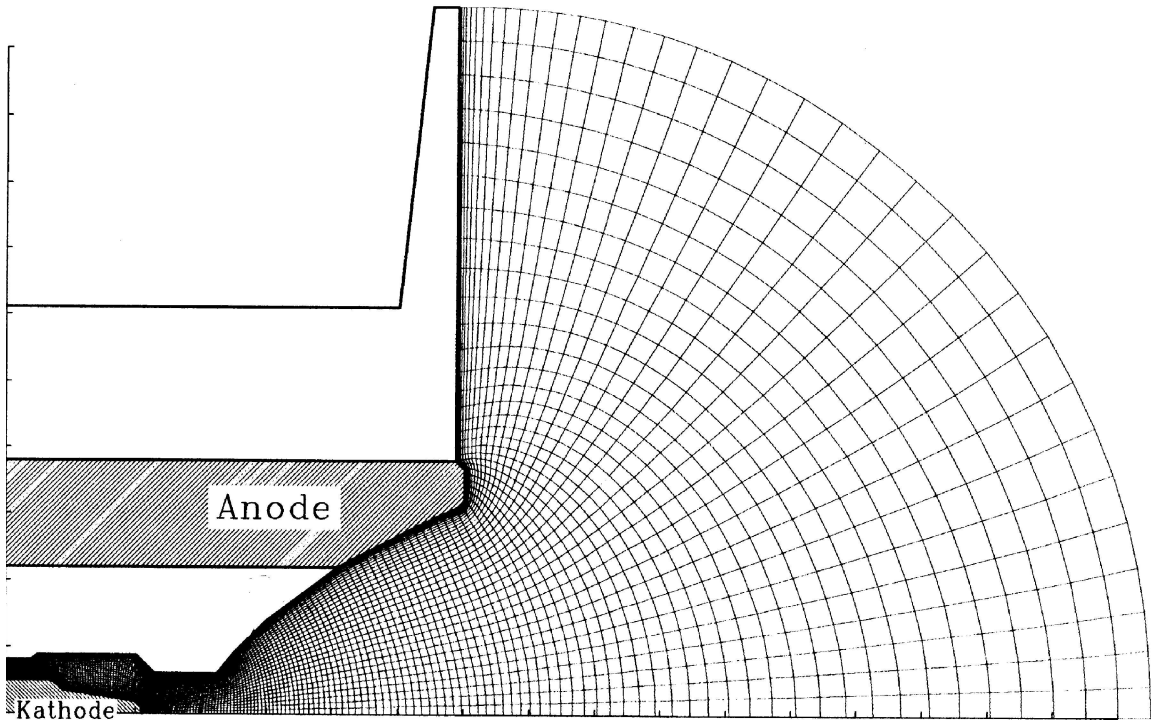
Figure 3.2: Non-uniform, orthogonal structured grid (obtained from ref.[59]).
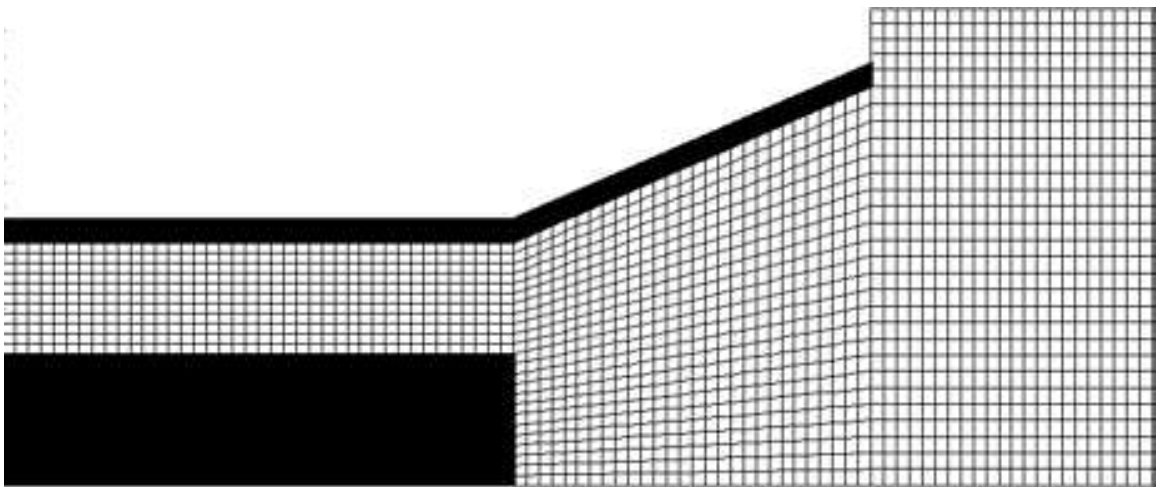
Figure 3.3: Non-uniform, non-orthogonal structured grid.
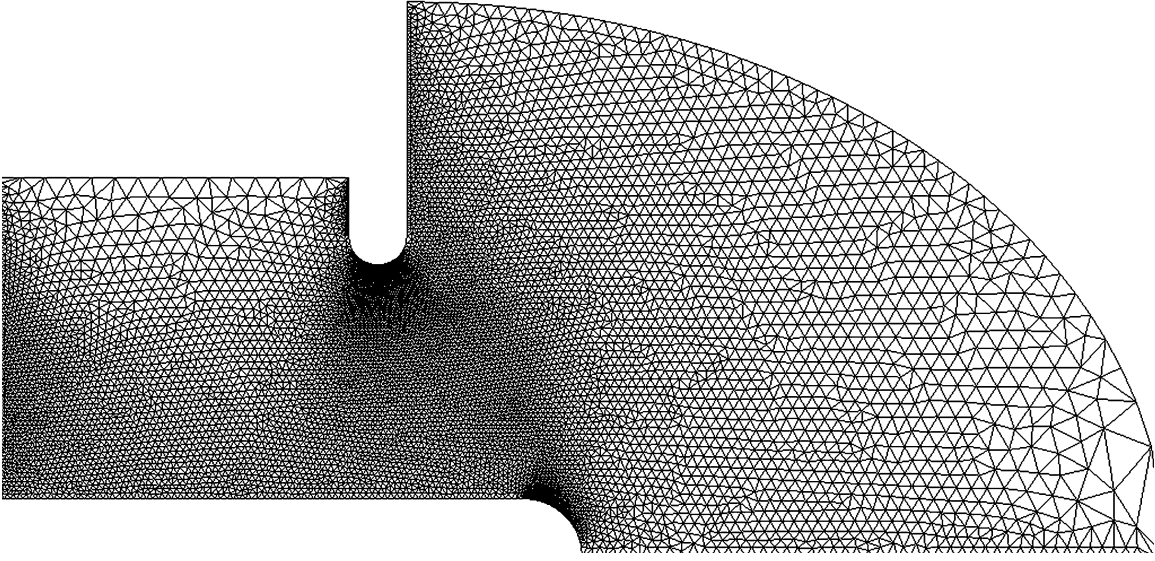
Figure 3.4: Non-uniform, non-orthogonal unstructured grid.

Grids of type 4 (unstructured) may seem very attractive because of their adaptability to complex geometries, and have been popular (cf. refs.[56, 61, 63, 64, 65, 33]). However there are some disadvantages that may not be immediately apparent. Unstructured grids are computationally expensive and there are problems in extending higher order accurate schemes to them. Since the precise control of geometry may not be as critical to the design of plasma thrusters as it is to, say aircraft design, the use of unstructured grids may not be as worthwhile. This work currently uses grids of type 3, shown in Fig.(3.3).

The variables to be computed, given by U in eqn.(3.1), can be stored either in the vertices of the cells, or in the center of the cells (further discussion can be found in ref.[107]). In the former, the variables will coincide with the boundary, and they will be specified as boundary conditions. In the latter, the faces of the cells will be aligned with the walls, and the fluxes of these variables will be specified as boundary conditions. While solving the conservative formulation, it is preferable to choose the cell-centered scheme since specifying the fluxes is more compatible with the governing equations.

3.3 Consistency, Stability, and Convergence

The true mathematical form of the systems of conservation laws are integral relations, while the partial differential forms are actually a special case, in which smoothness of the solution is assumed. To use the differential form in the presence of a discontinuity in the solution, one has to introduce the concept of weak form of the differential equations (cf. LeVeque[84]). Often, there are more than one possible weak solutions, of which, of course, only one is physical. If the numerical scheme converges to a solution, the question to be answered is, "Is it the correct solution?".

3.3.1 Lax-Wendroff Theorem

The above question is answered by the *Lax-Wendroff theorem*, that states that (cf. [84]):

> *If the numerical approximation computed with a consistent and conservative method converges, then the converged solution is the correct solution of the conservation law*.

This is a powerful result, but it does not help to determine *if* a scheme is convergent, but merely assures that the converged solution is the correct one.

3.3.2 Criteria for Stability and Convergence

For a linear numerical scheme there are a few techniques available to analyze stability. The most popular of these was developed by John von Neumann[108] during the Manhattan project and is commonly referred to as the von Neumann stability analysis (VNSA). It involves discrete Fourier transforming the solution and inspecting the growth of waves in the frequency space. This approach is intuitively obvious because, like many physical instabilities, numerical instabilities are often a result of unbounded growth of certain oscillations. Using this technique, it is possible to determine physically allowable combinations of grid spaces and time steps which will result in a stable numerical scheme.

Given a consistent and stable linear numerical scheme, the goal is to ensure that, as the discrete grid is refined to better emulate the continuous domain of the true solution, the discrete solution approaches the true solution. In other words, the solution should converge. These three concepts, consistency, stability and convergence, are related by the *Lax Equivalence Theorem* which assures that (cf. ref.[84]):

> *For a properly posed initial value problem, with a consistent linear numerical scheme,*
> *stability is the necessary and sufficient condition for convergence.*

This is indeed a useful result, since the VNSA can determine the stability of a linear method, and consistency can be easily verified, it is straightforward to determine if the numerical solution will converge to the true solution.

However, nonlinear convergence and stability are not simple extensions of their analog in the linear system. The Lax equivalence theorem is strictly applicable only to linear numerical schemes. Though some nonlinear equations can be linearized to obtained approximate answers, it is not of much help for truly nonlinear set of equations. For problems, such as the set of conservation laws seen in eqn.(2.58), requiring nonlinear operators, the need for establishing convergence still exists. Compounding the difficulty is the fact that VNSA is of practical use only for linear equations. In the complex set of highly nonlinear equations, such as MHD equations and Euler equations of compressible gas dynamics, a discrete Fourier transform would yield different frequencies. However, without the principle of linear superposition, any sort of VNSA becomes intractable, as explained by Laney[109].

Over the years, research in numerical techniques has led to the development of techniques to determine the stability and convergence of nonlinear systems of equations. The most useful among these are discussed below.

Total Variation Diminishing Schemes

One method of analyzing stability stems from the classical concept of total variation in real and functional analysis (cf. ref.[110]). Harten[111] adapted this to the sorts of functions seen in computational gasdynamics. The *total variation* of a function $\mathbf{U}$ can be defined as:

$$TV\left(\mathbf{U}\right) = \int\limits_{-\infty}^{\infty} \left|\frac{d\mathbf{U}}{dx}\right| dx. \tag{3.3}$$

For the discrete situation, eqn.(3.3) can be written as:

$$TV\left(\mathbf{U}^n\right) = \sum_j \left|\mathbf{U}_{j+1}^n - \mathbf{U}_j^n\right|. \tag{3.4}$$

It can be proven (cf. ref.[109]) that the solutions to the conservation equations must be *total variation diminishing (TVD)* in the sense:

$$TV\left(\mathbf{U}^{n+1}\right) \leq TV\left(\mathbf{U}^n\right), \tag{3.5}$$

for all time levels. Since oscillations add to the total variation, the TVD condition cannot be satisfied by unbounded growth of oscillations. Thus, the TVD condition can be used as a stability check for nonlinear equations.

Local Extremum Diminishing Schemes

Though the TVD principle is a popular check for convergence, it has its limitations. Since it imposes a condition only on the global variations, a scheme satisfying TVD condition eqn.(3.5) could, theoretically, allow spurious local oscillations (cf. ref.[109]). A more practical limitation of the TVD condition is that its extension to multidimensional problems does not provide a satisfactory measure of oscillations. To overcome both these shortcomings, Jameson[112] has developed the concept of *local extremum diminishing (LED)* schemes, which is summarized below.

Any time dependent conservation law, such as eqn.(2.58), can be written in a general form:

$$\frac{d\mathbf{U}_j}{dt} = \sum_{j \neq k} C_{j,k} \left(\mathbf{U}_k - \mathbf{U}_j \right).\tag{3.6}$$

If the numerical scheme has a compact stencil, in which the value at the point is directly dependent only on its nearest neighbors, and if the coefficients are all non-negative, then:

$$C_{j,k} = \begin{cases} \geq 0; k = j \pm 1, \\ = 0; \text{else} \end{cases}\tag{3.7}$$

If $\mathbf{U}_j$ is a local maximum, then, $(\mathbf{U}_k - \mathbf{U}_j) \leq 0$, causing $d\mathbf{U}_j/dt \leq 0$. Conversely, if $\mathbf{U}_j$ is a local minimum, then, $(\mathbf{U}_k - \mathbf{U}_j) \geq 0$, causing $d\mathbf{U}_j/dt \geq 0$. These schemes are, therefore, aptly called *local extremum diminishing* (LED). Apart from ensuring that there are no local oscillations, the schemes built on this condition can be easily extended to multi dimensions. It can be shown that TVD is actually a 1-D special case of the LED concept.

It can be shown[112] that schemes built on obtaining information from the upwind part of a characteristic do satisfy positivity constraints (eqn.(3.7)) and are thus stable. This concept is used in the developing the numerical scheme used in this work.

3.4   Convergence and Stability Checks

In order to verify convergence, there are two types of diagnostics in the code. In the first diagnostic, the change of conserved variables between every time level is calculated. In each case the largest *change* in the domain, and the average *change* over the entire domain are stored. Monitoring the maximum change helps check for stability. Monitoring the average change helps check for convergence. Since the entire set of eqns.2.58 is of the form,

$$\frac{dU}{dt} + \nabla \cdot \mathcal{F} = 0 \,,\tag{3.8}$$

monitoring $\Delta t \left(\nabla \cdot \mathcal{F} \right)$ is an appropriate measure of change in U. The time history of the average change throughout the domain of an MPDT is shown in Fig.(3.5).

In the second diagnostic, the maximum *value* in the domain, and the average *value* over the domain of the conserved variables are stored. As before, monitoring the maximum value helps check for stability, and monitoring the average value helps check for convergence. The time history of the average value throughout the domain is shown in Fig.(3.5). From these plots, it was observed that convergence is reached only after $\sim 2.0 \times 10^6$ time steps, which corresponds to $\sim 200\mu s$ of physical time. The converged values of relevant variables are shown in §4.1.4.

3.5   Conservation Form

From a numerical solution perspective, it can be shown that the conservative formulation is necessary to accurately capture discontinuities. This can be seen even in a simple equation such as the Burger's equation (cf. ref.[84]):

$$\frac{\partial u}{\partial t} + \frac{\partial \left(u^2/2\right)}{\partial x} = 0 \tag{3.9}$$

If eqn.(3.9) is solved using non-conservative schemes such as Lax-Friedrichs,

$$u_j^{n+1} = \frac{u_{j+1}^n + u_{j-1}^n}{2} - \Delta t \left[\frac{u_{j+1}^n + u_{j-1}^n}{2} \frac{u_{j+1}^n - u_{j-1}^n}{2\Delta x} \right], \tag{3.10}$$

or backward differencing,

$$u_j^{n+1} = u_j^n - \Delta t \left[u_j^n \frac{u_j^n - u_{j-1}^n}{\Delta x} \right], \tag{3.11}$$

it can be verified that both eqns. and give incorrect solutions of eqn.(3.9).

However, a conservative numerical formulation of eqn.(3.9),

$$u_j^{n+1} = u_j^n - \frac{\Delta t}{2\Delta x} \left[(u_j^n)^2 - (u_{j-1}^n)^2 \right], \tag{3.12}$$

will give the correct answer. For further information on this issue, refer to LeVeque[84].

Most of the discussion on the numerical techniques has emphasized the hyperbolic nature of the convective part of the problem. This is because the goal of this work is to simulate problems in propulsion, consequently computing the flow is the most important part. Also, the convective
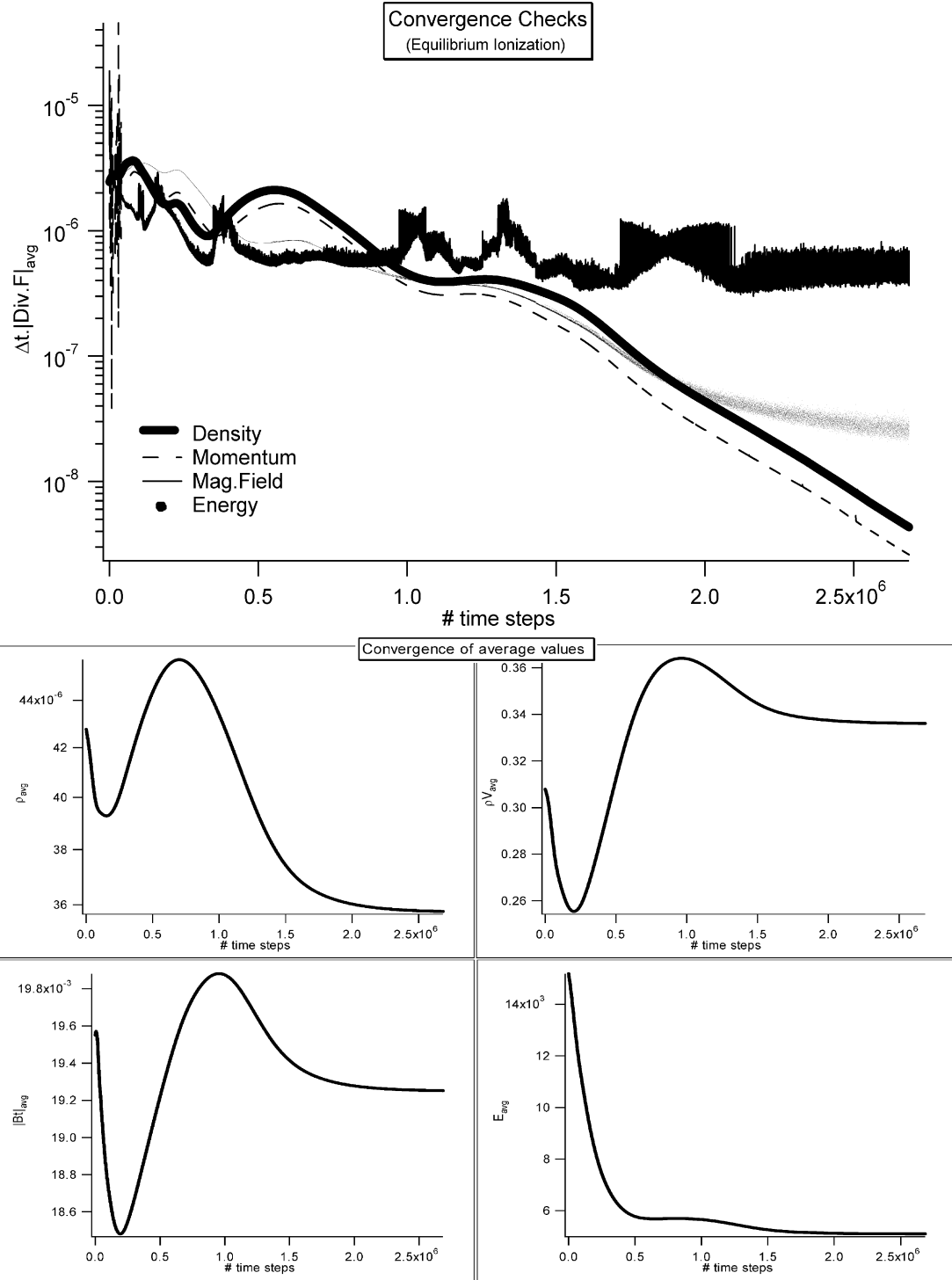
Figure 3.5: A. Convergence rates for the conserved variables; B. Domain averaged values of i) Density, ii) Axial momentum, iii) Magnetic field, and iv) Total energy at each time step

problem is the harder one to solve numerically. The dissipative part of the problem, which is responsible for adding a parabolic nature to the governing equations, is relatively well understood. However, as explained in section 3.1, there is strong coupling between the hyperbolic and the parabolic part of the problem.

This coupling raises important issues in spatial as well as temporal discretization. The issue regarding the time scales is discussed in §3.6.2. In the case of spatial discretization, the issue is that schemes that are good for parabolic equations are not suited for hyperbolic equations. Consider a simple scalar diffusion equation,

$$\frac{\partial u}{\partial t} = \mu \frac{\partial^2 u}{\partial x^2}. \tag{3.13}$$

A standard scheme to solve this equation is the explicit central differencing scheme:

$$u_j^{n+1} = u_j^n + \Delta t \left[\frac{u_{j+1}^n - 2u_j^n + u_{j-1}^n}{\Delta x^2} \right]. \tag{3.14}$$

However, it can be easily verified that for a simple scalar convection equation,

$$\frac{\partial u}{\partial t} + \lambda \frac{\partial u}{\partial x} = 0, \tag{3.15}$$

the FTCS scheme analogous to eqn.(3.14) does not satisfy the positivity condition (eqn.(3.7)) and even fails the VNSA.

On the other hand, a good scheme for solving the scalar convection equation is the explicit backward differencing scheme:

$$u_j^{n+1} = u_j^n - \Delta t \left(\lambda \left[\frac{u_j^n - u_{j-1}^n}{\Delta x} \right] \right). \tag{3.16}$$

Obviously, this scheme will not work for the diffusion equation because the numerical domain of dependence does not contain the physical domain of dependence (recall the CFL condition).

Therefore, it is clear that discretization of the convective and dissipative parts of the problem must be treated separately.

3.6 Hyperbolic (Convection) Equations

3.6.1 Spatial Discretization

The numerical solution to the set of hyperbolic equations (eqn.2.58 without the diffusion terms) is based on techniques that are extensively used in computational fluid dynamics. Based on the pioneering work of Godunov[113], [114], the principles underlying the design of non-oscillatory discretization schemes for compressible flows have been well established. There are two important issues in the design of discretization schemes:

- Estimating the numerical flux through cell boundaries, accounting for waves (discussed in appendix §D) traveling at different speeds, and possibly in different directions.

- Obtaining non-oscillatory solutions and capturing discontinuities with sufficient accuracy.

The scheme used in this thesis is developed in terms of local extremum diminishing (LED) principle of Jameson[112]. The method can be explained using eqn.(2.58) in one spatial dimension,

$$\frac{d\mathbf{U}_j}{dt} + \frac{\mathbf{Hz}_{j+1/2} - \mathbf{Hz}_{j-1/2}}{\Delta z} = 0, \tag{3.17}$$

where, $\mathbf{U}$ is the vector of conserved variables, and $\mathbf{Hz}$ is the approximation of flux in the $\hat{z}$ direction.

The true flux, obtained from eqn.(2.58), in the $\hat{z}$ direction can be split as,

$$\mathbf{Fz}(\mathbf{U}) = \mathbf{Fz}(\mathbf{U})^+ + \mathbf{Fz}(\mathbf{U})^-, \tag{3.18}$$

where the eigenvalues of $d\mathbf{Fz}^+/d\mathbf{U}$ are all non-negative, and the eigenvalues of $d\mathbf{Fz}^-/d\mathbf{U}$ are all non-positive. Then, the approximation of flux is estimated as,

$$\mathbf{Hz}_{j+\frac{1}{2}} = \mathbf{Fz}_j^+ + \mathbf{Fz}_{j+1}^-.$$

Using eqn.(3.18), this can be rewritten as,

$$\mathbf{Hz}_{j+\frac{1}{2}} = \frac{1}{2}\left(\mathbf{Fz}_j + \mathbf{Fz}_{j+1}\right) - \mathbf{Dz}_{j+\frac{1}{2}},$$

where

$$\mathbf{Dz}_{j+\frac{1}{2}} = \frac{1}{2} \left[\left\{ \mathbf{Fz}_{j+1}^+ - \mathbf{Fz}_j^+ \right\} - \left\{ \mathbf{Fz}_{j+1}^- - \mathbf{Fz}_j^- \right\} \right]. \tag{3.19}$$

There still remains a question of how $\mathbf{Fz}^+$ and $\mathbf{Fz}^-$ can be evaluated. This evaluation is possible if there is a matrix $\mathbf{A}$, such that

$$\Delta \mathbf{Fz}_{j+1/2} = \mathbf{A} \cdot \left(\Delta \mathbf{U}_{j+1/2} \right) , \tag{3.20}$$

where $\Delta \mathbf{Fz}_{j+1/2} = \mathbf{Fz}_{j+1} - \mathbf{Fz}_j$, and $\Delta \mathbf{U}_{j+1/2} = \mathbf{U}_{j+1} - \mathbf{U}_j$. Note that, in the case the points $j + 1$ and j are on opposite sides of a discontinuity, eqn.(3.20) indicates that this scheme satisfies the Rankine-Hugoniot jump conditions exactly.

Since the ideal MHD equations are hyperbolic, they have real characteristics. Therefore, the characteristic directions or characteristic manifolds have important physical meaning, since all information propagates along them (as explained in refs. [115, 72]). Moreover, the eigenvectors of the Jacobian, $\mathbf{A}$, are orthogonal and can be normalized. Therefore, the Jacobian can be diagonalized as:

$$\mathbf{A} \equiv \mathbf{R}\mathbf{\Lambda}\mathbf{R}^{-1}, \tag{3.21}$$

where $\mathbf{R}$ contains the right eigenvectors of $\mathbf{A}$ as its columns, and $\mathbf{R}^{-1}$ contains the left eigenvectors of $\mathbf{A}$ as its rows. $\mathbf{\Lambda}$ is the diagonal matrix of eigenvalues of $\mathbf{A}$. Since $\mathbf{\Lambda}$ can be easily split into,

$$\mathbf{\Lambda} = \mathbf{\Lambda}^+ + \mathbf{\Lambda}^-,$$

using eqn.(3.21), $\mathbf{A}$ can be split as,

$$\mathbf{A}^\pm \equiv \mathbf{R}\mathbf{\Lambda}^\pm\mathbf{R}^{-1}. \tag{3.22}$$

Thus if there exists an $\mathbf{A}$ such that eqn.(3.20) is true, then,

$$\Delta \mathbf{Fz}_{j+1/2}^\pm = \mathbf{A}^\pm \cdot \left(\Delta \mathbf{U}_{j+1/2} \right) . \tag{3.23}$$

Defining $|\mathbf{A}| = \mathbf{A}^+ - \mathbf{A}^-$, eqn.(3.19) can be written as,

$$\mathbf{Dz}_{j+\frac{1}{2}} = \frac{1}{2} |\mathbf{A}| \cdot \Delta\mathbf{U}_{j+\frac{1}{2}} \ . \tag{3.24}$$

For the Euler equations, the matrix $\mathbf{A}$ was derived by Roe[116, 117]. However, this is not necessarily applicable to MHD equations. There have been efforts by Cargo[118] to derive such matrices for MHD equations. The literature[119] suggests that various forms of averaged matrices work satisfactorily.

From Godunov's theorem, it is evident that the scheme can only be first-order accurate, if it is to capture discontinuities. However, away from the discontinuities, the spatial accuracy of the scheme can be improved by including flux-limited anti-diffusion, $\mathbf{Lz}$, described by Jameson[112]:

$$\mathbf{Dz}_{j+\frac{1}{2}} = \frac{1}{2} |\mathbf{A}| \left[\Delta\mathbf{U}_{j+\frac{1}{2}} - \mathbf{Lz} \left(\Delta\mathbf{U}_{j+\frac{3}{2}}, \Delta\mathbf{U}_{j-\frac{1}{2}} \right) \right] . \tag{3.25}$$

Essentially, this reduces numerical diffusion where it is not required.

Similar equations can be written for the corresponding terms in the $\hat{r}$ direction.

An alternative to characteristics-splitting for solving conservation form of the equations is to use artificial viscosity (scalar diffusion). In this formalism, the equivalent expression for eqn.(3.24) is,

$$\mathbf{Dz}_{j+\frac{1}{2}} = \frac{1}{2} |\lambda|_{max} \Delta\mathbf{U}_{j+\frac{1}{2}}. \tag{3.26}$$

Because of its low computational cost, scalar diffusion schemes such as eqn.(3.26) have been successfully adapted for industrial applications such as aircraft design. However, since these schemes tend to artificially smooth out the solution [112], eqn.(3.26) was only used in this work for comparison with eqn.(3.25).

3.6.2 Temporal Discretization

Unlike in fluid mechanics, the equations of MHD allow many different types of waves to exist. Even though physically the flow velocity is the sought quantity of most interest to propulsion, nu-

merically the velocity of the fastest wave is what determines the time-step constraints. In plasmas of propulsion interest, the fluid velocity is $\mathcal{O}(10^4)$ m/s . For a quasineutral plasma with charge density of $\mathcal{O}(10^{21})/\mathrm{m}^3$ and thermodynamic pressures of $\mathcal{O}(10^{-1})$ Torr and magnetic pressure of $\mathcal{O}(10^1)$ Torr, the fast magnetosonic wave speed is typically of the same order of magnitude as the flow velocity. This indicates that an explicit time marching scheme is suitable. From the CFL criterion, the time step for such a problem would be $\mathcal{O}(10^{-8} - 10^{-9})$ s.

A multi-stage scheme can be chosen to march forward in time. Writing eqn.(2.58) as,

$$\frac{d\mathbf{U}}{dt} + \mathcal{F}(\mathbf{U}) = 0 , \tag{3.27}$$

where $\mathcal{F}(\mathbf{U})$ represents the sum of all the fluxes, the multi-stage scheme can be written as:

$$
\begin{aligned}
\mathbf{U}^1 &= \mathbf{U}^n - \alpha_1 \Delta t\, \mathcal{F}(\mathbf{U}^n) , \\
\mathbf{U}^2 &= \mathbf{U}^n - \alpha_2 \Delta t\, \mathcal{F}(\mathbf{U}^1) , \\
\mathbf{U}^3 &= \mathbf{U}^n - \alpha_3 \Delta t\, \mathcal{F}(\mathbf{U}^2) , \\
\mathbf{U}^4 &= \mathbf{U}^n - \alpha_4 \Delta t\, \mathcal{F}(\mathbf{U}^3) , \\
\mathbf{U}^{n+1} &= \mathbf{U}^4 .
\end{aligned}
\tag{3.28}
$$

The coefficients used in this work are $\alpha_1 = 0.1084, \alpha_2 = 0.2602, \alpha_3 = 0.5052, \alpha_4 = 1.0$, and were obtained from ref.[120]. This multi-stage scheme offers increased temporal accuracy and stability, and was therefore used for the unsteady test cases described below. However, it is not beneficial when only the steady-state solution is sought. In those cases, a standard one-step explicit Euler time-stepping scheme was used.

3.6.3   Verification

Unsteady Case

<u>Riemann problem</u>

The test problem chosen to validate this scheme was of the classical Riemann problem type, which

consists of a single jump discontinuity in an otherwise smooth initial conditions. In 1-D the problem is:

$$\mathbf{U}(x,0) = \begin{cases} \mathbf{U}_L & \text{if } x < \frac{L}{2} \\ \mathbf{U}_R & \text{if } x \geq \frac{L}{2} \end{cases}. \tag{3.29}$$

The Riemann problem was chosen because it is one of the very few that have an analytical solution. This problem provides an excellent illustration of the wave nature of the equations. The solution to the Riemann problem is useful to verify the capturing of both smooth waves (characteristics) as well as non-smooth waves (shocks).

The initial states used were very similar to the Sod's problem[121] for Euler equations. They were:

$$\text{Left}: \begin{cases} \rho & = 1.0 \\ V_x & = 0.0 \\ V_y & = 0.0 \\ V_z & = 0.0 \\ B_x & = \frac{3}{4} \\ B_y & = 1.0 \\ B_z & = 0.0 \\ p & = 1.0 \end{cases} \quad \text{Right}: \begin{cases} \rho & = \frac{1}{8} \\ V_x & = 0.0 \\ V_y & = 0.0 \\ V_z & = 0.0 \\ B_x & = \frac{3}{4} \\ B_y & = -1.0 \\ B_z & = 0.0 \\ p & = \frac{1}{10} \end{cases}. \tag{3.30}$$

Some sample results are shown in Fig.(3.6).

The solution was computed at a dimensionless time (defined in ref.[122], based on the fast magnetosonic speed and the grid dimension) of $\tau = 0.1$, with the initial conditions described above. The solutions for the magnetic field and pressure profiles, with 400 points in the spatial dimension, are presented in Fig.(3.6). The number of points in the domain, and the time τ were chosen to allow comparisons to other works, such as ref.[105].

In these figures, the fast rarefaction (FR) wave can be seen on the far right and the far left, as it is the fastest of the waves present in the problem. The slow shock (SS) and the compound wave

60
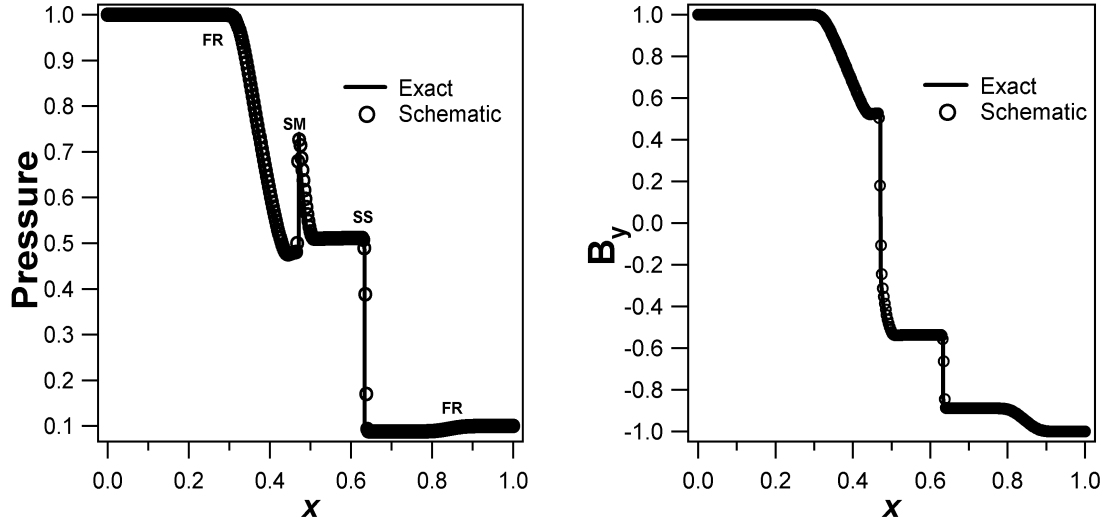
Figure 3.6: Comparison of calculated profiles of pressure and magnetic field, with exact solution

(SM) have speeds less than that of the FR wave.

As seen in these figures, the scheme successfully captures the time-dependent discontinuities.

Steady-State Case

Taylor state

In order to simulate steady-state MHD flows, this solver can be used to solve the unsteady equations and marched to steady state. An important question is whether the solution remains in that steady state. To answer this question, a test problem was chosen, whose equilibrium solution is known analytically. This equilibrium solution is given as the initial condition for the solver. After marching several hundreds or thousands of time steps, a check is performed if the variables have changed from the initial conditions.

The test problem chosen for this simulation was the Taylor State configuration[123]. Under certain conditions, described in ref.[123], when a bounded plasma is allowed to evolve, it will move quickly and dissipate energy before coming to rest. This stable equilibrium configuration

can be analytically found using the minimum energy principle, and is of the form:

$$\nabla \times \mathbf{B} = \lambda \mathbf{B}, \tag{3.31}$$

where λ is an eigenvalue.

Since the current is parallel to the magnetic field, the $\mathbf{j} \times \mathbf{B}$ body force is identically zero. Furthermore, if there are no thermodynamic pressure gradients, the plasma is in a state of force-free equilibrium. For an axisymmetric geometry, the resulting magnetic field profile is:

$$B_\theta = B_0 J_1(\lambda r); \ B_z = B_0 J_0(\lambda r), \tag{3.32}$$

where B_o is a constant amplitude, J_0 and J_1 are Bessel functions of the first kind, of orders 0 and 1 respectively.

For a Cartesian grid of dimensions $L_x \times L_z$, with symmetry along the $\hat{y}$ direction, the magnetic field distribution satisfying eqn.(3.31) is:

$$
\begin{aligned}
B_x &= -\frac{B_0}{\sqrt{2}} \ \sin\left(\frac{m\pi x}{L_x}\right) \cos\left(\frac{n\pi z}{L_z}\right), \\
B_y &= B_0 \ \sin\left(\frac{m\pi x}{L_x}\right) \sin\left(\frac{n\pi z}{L_z}\right), \\
B_z &= \frac{B_0}{\sqrt{2}} \ \cos\left(\frac{m\pi x}{L_x}\right) \sin\left(\frac{n\pi z}{L_z}\right),
\end{aligned}
\tag{3.33}
$$

where m and n are eigenvalues.

With these initial conditions, the code was run for 10^4 time steps (based on the fast magnetoacoustic speed) on a 100×100 grid. At the end, the solution had deviated from equilibrium by less than 0.5%. The results from the code for B_x given in eqn.(3.33) are compared with the exact solution in Fig.(3.7).

Thus the *property of linearity preservation* has been successfully verified for this solver.
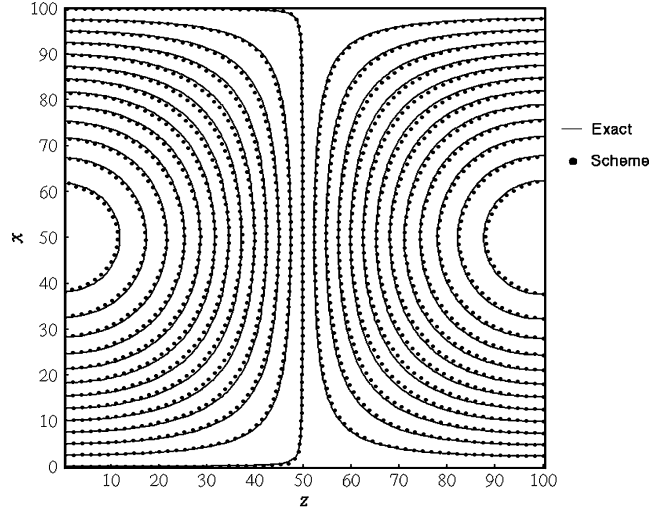
Figure 3.7: Magnetic field in the Taylor state configuration

3.7 Parabolic (Diffusion) Equations

3.7.1 Spatial Discretization

Numerical methods for parabolic equations are relatively commonplace. The parabolic terms can be written as,

$$
\mathbf{S}_{dis} = \nabla \cdot
\begin{bmatrix}
\mathbf{0} \\
0 \\
\bar{\bar{E}}_{res} \\
\mathbf{q}
\end{bmatrix} ,
$$

where

$$
\nabla \cdot \bar{\bar{E}}_{res} = -\nabla \times \left[\frac{\bar{\bar{\eta}} \cdot (\nabla \times \mathbf{B})}{\mu_o} \right] ,
$$

represents the resistive diffusion of the magnetic flux, including the Hall effect, and,

$$
\nabla \cdot \mathbf{q} = \nabla \cdot \left[\left\{ -\frac{\mathbf{E}' \times \mathbf{B}}{\mu_o} \right\} + \{ k_{th} \nabla T \} \right] , \tag{3.34}
$$

represents the energy sources/sinks due to viscous heating, Ohmic heating, and thermal conduction respectively. The first term, energy dissipation due to viscosity, can be shown[18] to be several orders of magnitude less than Ohmic heating, and therefore will be ignored henceforth.

Thus, the equations dictate that the numerical scheme should be second-order accurate in space. In the framework used here, this implies that the first derivatives of variables are to be known across cell faces. Therefore, a simple central-differencing scheme will be sufficient for this problem.

3.7.2 Temporal Discretization

Physical dissipation brings in different characteristic time scales into the problem. They are:

Magnetic diffusion: $= \mu_o \Delta r^2 / \eta \sim 10^{-10} - 10^{-11}$ s,

Thermal conduction: $= n_e k_B \Delta r^2 / k_{th} \sim 10^{-9} - 10^{-11}$ s.

Since these time scales could reach the extremities of the ranges mentioned, the choice of the time stepping scheme can be made on a case-by-case basis. If they are not vastly different, and an explicit *fractional time-stepping* scheme can be chosen.

In the situations when the time scales are less than two orders of magnitude apart, it may not be worthwhile to choose an implicit scheme, however a standard explicit or multi-stage time-stepping scheme would be expensive because it would require evaluating the convective fluxes at the time scales of dissipative fluxes. In order to find an optimum, a fractional time-stepping scheme can be chosen. In this method, the equation,

$$\frac{\partial \mathbf{U}}{\partial t} + \nabla \cdot \bar{\bar{\mathcal{F}}}_{\text{conv}} = \nabla \cdot \bar{\bar{\mathcal{F}}}_{\text{diff}} , \tag{3.35}$$

is marched forward at the dissipative time scale, Δt_d, dictated by the dissipative fluxes, $\bar{\bar{\mathcal{F}}}_{\text{diff}}$. However the convective fluxes, $\bar{\bar{\mathcal{F}}}_{\text{conv}}$, are evaluated only after N dissipative time steps. The number N is chosen such that the effective convective time step, $\Delta t_c = N \Delta t_d$, is still smaller then the convective time step dictated by the CFL condition. By reducing the time consuming operation of evaluation of the convective fluxes, the effective speed of the computation increases

significantly. In this work $N \simeq 10$ to 25 has been tried successfully. It should be noted that fractional time stepping is beneficial only if evaluation of convective fluxes is expensive compared internal calculations.

3.8   Application of Governing Equations

The conservation form of the MHD equations, given in eqn.(2.58), describe the evolution of eight variables, namely the total density (ρ), three components of momentum ($\rho u, \rho v, \rho w$), three components of magnetic field (B_r, B_θ, B_z), and the total energy ($\mathcal{E}$). However, in a self-field MPDT/LiLFA the magnetic field is purely azimuthal. Moreover, due to the assumption of axisymmetry, azimuthal momentum can be neglected. Though the solver described in §3.1 - §3.7 is for the generalized set of eight equations, it can be reduced for a system of five equations: the total density (ρ), two components of momentum ($\rho u, \rho w$), one component of magnetic field (B_θ), and the total energy ($\mathcal{E}$).

Expanding the vector-tensor form of eqn.(2.58) in cylindrical coordinates, using the identities eqns. (C.5), (C.6), and (C.7), along with the assumptions stated above, the MHD equations are:

$$
\frac{\partial}{\partial t}
\begin{bmatrix}
\rho \\
\rho u \\
\rho w \\
B_\theta \\
\mathcal{E}
\end{bmatrix}
+
\frac{\partial}{\partial r}
\begin{bmatrix}
\rho u \\
\rho u^2 + p + \frac{B^2}{2\mu_o} \\
\rho u w \\
-E'_z + u B_\theta \\
u \left(\mathcal{E} + p + \frac{B^2}{2\mu_o} \right) - q_r
\end{bmatrix}
+
\frac{\partial}{\partial z}
\begin{bmatrix}
\rho w \\
\rho u w \\
\rho w^2 + p + \frac{B^2}{2\mu_o} \\
E'_r + w B_\theta \\
w \left(\mathcal{E} + p + \frac{B^2}{2\mu_o} \right) - q_z
\end{bmatrix}
= \mathbf{S}_r \quad (3.36)
$$

65

with

$$
\mathbf{S}_r = -\frac{1}{r}
\begin{bmatrix}
\rho u \\[6pt]
\rho u^2 + \frac{B^2}{\mu_o} \\[6pt]
\rho u w \\[6pt]
0 \\[6pt]
u\left(\mathcal{E} + p + \frac{B^2}{2\mu_o}\right) - q_r
\end{bmatrix}
\qquad
\begin{aligned}
q_r &= \frac{E'_z B_\theta}{\mu_o} + \left(k_{th,e}\frac{\partial T_e}{\partial r}\right) + \left(k_{th,i}\frac{\partial T_h}{\partial r}\right) \\[6pt]
q_z &= \frac{-E'_r B_\theta}{\mu_o} + \left(k_{th,e}\frac{\partial T_e}{\partial z}\right) + \left(k_{th,i}\frac{\partial T_h}{\partial z}\right)
\end{aligned}
$$

These equations are solved, in combination with species energy equations (eqn.(2.40) and/or eqn.(2.41)), at every time level, throughout a specified domain (to be described in §4.2.1), for a given set of initial and boundary conditions, to be described in §4.1.3 and §4.1.2 respectively.

3.9 Finite Volume Formulation

The MHD equations, in eqns.(2.58 & 3.36) are conservation relations for mass *density*, momentum *density*, magnetic flux, and energy *density*. However, in reality, the conserved quantities are, mass, momentum, magnetic flux, and energy. Therefore, the first, second, and the fourth equations in the set eqn.(2.58) need to be multiplied by the volume element. In cylindrical coordinates, the volume of the cell is $2\pi r\, dr\, dz$.

Equations of the form,

$$
\frac{\partial U}{\partial t} = \frac{\partial F_r}{\partial r} + \frac{\partial F_z}{\partial z} + S \;, \tag{3.37}
$$

upon multiplication by the volume of the cell ($2\pi r\, dr\, dz$) take the form,

$$
\frac{\partial \left(r U\right)}{\partial t} = \frac{\partial \left(r F_r\right)}{\partial r} + \frac{\partial \left(r F_z\right)}{\partial z} + \left(S - F_r\right) \;. \tag{3.38}
$$

66

3.9.1   Integral Form

Now, these equations can be written in their integral form. Every one of these five conservation laws (for mass, radial momentum, axial momentum, magnetic flux, and total energy) can be individually integrated over the cell area,

$$\iint_A \left[\frac{\partial U}{\partial t} = \left(\frac{\partial F_r}{\partial r} + \frac{\partial F_z}{\partial z} \right) + \text{Source} \right] dA \; . \tag{3.39}$$

Now, if a vector $\hat{\mathbf{F}} = [F_z, -F_r]$, is defined, then,

$$\nabla \times \hat{\mathbf{F}}|_\theta = \frac{\partial \hat{F}_r}{\partial z} - \frac{\partial \hat{F}_z}{\partial r} = \frac{\partial F_r}{\partial r} + \frac{\partial F_z}{\partial z} \; . \tag{3.40}$$

Then, the right hand side of eqn.(3.39) can be expressed as the curl of $\hat{\mathbf{F}}$. Then, using Stokes' theorem, this curl over the cell area can be expressed as the line integral around the edges of the cell,

$$\iint_A \frac{\partial U}{\partial t} dA = \oint \hat{\mathbf{F}} \cdot \mathbf{dl} + \iint_A (\text{Source}) \, dA \; . \tag{3.41}$$

Since this equation is true irrespective of the shape of the control volume, the fluxes Fr and Fz can written in the (r,z) coordinate system, as shown in eqn.(3.42), regardless of the shape of the cell.

So, the finite volume formulation of eqn.(2.58) is,

$$
\frac{\partial}{\partial t}
\begin{bmatrix}
r\rho \\
r\rho u \\
r\rho w \\
B_\theta \\
r\mathcal{E}
\end{bmatrix}
+\frac{\partial}{\partial r}
\begin{bmatrix}
r\rho u \\
r\left(\rho u^2 + p + \frac{B^2}{2\mu_o}\right) \\
r\rho uw \\
-E'_z + uB_\theta \\
r\left(u\left(\mathcal{E} + p + \frac{B^2}{2\mu_o}\right) - q_r\right)
\end{bmatrix}
+\frac{\partial}{\partial z}
\begin{bmatrix}
r\rho w \\
r\rho uw \\
r\left(\rho w^2 + p + \frac{B^2}{2\mu_o}\right) \\
E'_r + wB_\theta \\
r\left(w\left(\mathcal{E} + p + \frac{B^2}{2\mu_o}\right) - q_z\right)
\end{bmatrix}
$$

$$
=
\begin{bmatrix}
0 \\
p - B^2/(2\mu_o) \\
0 \\
0 \\
0
\end{bmatrix},
\tag{3.42}
$$

where q_r and q_z are the same as in eqn.(3.36).

3.9.2 Derivatives in Non-orthogonal Coordinates

As it is apparent from eqn.(3.42), evaluation of dissipative fluxes requires computation of j_r, j_z as well as $\partial T/\partial r$ and $\partial T/\partial z$ across the bounding surfaces of a cell. In an orthogonal grid system, the gradients can be simply estimated as,

$$
\left.\frac{\partial B}{\partial z}\right|_{J,K+\frac{1}{2}} = \frac{B_{J,K+1} - B_{J,K}}{\Delta z},
\tag{3.43}
$$

and so forth.

However, in a non-orthogonal grid, the points (J,K) and (J,K+1) are not along the lines of constant "r". So, the gradients have to be estimated in a different manner.

Recall that, if some vector $\hat{\mathbf{B}} = [0, -rB]$, then,

$$
\nabla \times \hat{\mathbf{B}} = \frac{\partial(rB)}{\partial r} .
\tag{3.44}
$$

68
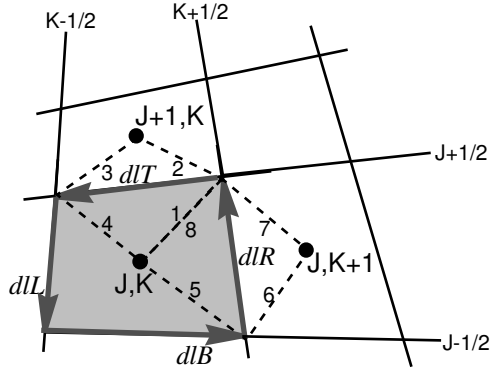
Figure 3.8: A general non-orthogonal control volume.

Using Stokes' theorem, this becomes,

$$j_z = \frac{1}{\mu_o}\frac{1}{r}\frac{\partial(rB)}{\partial r} = \frac{1}{\mu_o}\frac{1}{r}\frac{1}{A_{J+\frac{1}{2},K}}\oint[0,-rB]\cdot\mathbf{dl} \ . \tag{3.45}$$

Similarly, if $\hat{\mathbf{B}} = [B,0]$, then,

$$\nabla \times \hat{\mathbf{B}} = \frac{\partial B}{\partial z} \ , \tag{3.46}$$

which becomes,

$$j_r = -\frac{1}{\mu_o}\frac{\partial B}{\partial z} = -\frac{1}{\mu_o}\frac{1}{A_{J,K+\frac{1}{2}}}\oint[B,0]\cdot\mathbf{dl} \ . \tag{3.47}$$

Here, $A_{J,K+\frac{1}{2}}$ and $A_{J+\frac{1}{2},K}$ refer to the areas of the dotted cells in fig.(3.8) to the right and top, respectively. They can be estimated a simple averages of the control volumes.

The contour integrals in eqns.(3.47,3.45) require estimation of B along $\mathbf{dl}$, which is the dotted line in fig.(3.8). First, the line element vectors, $\mathbf{dl}$, themselves have to be computed from the coordinates of the vertices and the center of the cell. Then, B along this line element can be obtained by averaging from the nearby cell centers.

Now that the derivatives can be estimated across non-orthogonal surfaces, it enables the evaluation of all necessary fluxes. With this, all the pieces are in place for calculating the flowfields in real thrusters.

3.10 Parallel Computing

As described in §3.4 it takes $\mathcal{O}(10^6)$ time steps for a time-dependent simulation to reach steady state. In real time, this takes a single CPU roughly 200 to 400 hours to do this work. Clearly, there is a need to increase the computational speed to solve the problem at hand. With the current trend in high performance computer architectures being away from single processor scalar/vector machines, and toward the design and construction of parallel machines, it is important to exploit the strength of parallel computing platforms (cf. ref.[124]) for this purpose. A successful parallel implementation of a numerical algorithm must address how to allocate available resources (CPU/memory), how the algorithm itself is amenable to parallelization, and how the processors communicate efficiently.

For a given multiprocessor architecture, two distinct means of utilizing the computational power to solve a given problem can be identified: process decomposition, and domain decomposition (cf. ref.[125]).

3.10.1 Process Decomposition

Process decomposition involves allocating specific processors to specific portions of the algorithm. For instance, if n_{tot} processors are available to solve the problem at hand, then n_1 processors could be allocated to compute the convective fluxes, n_2 to compute diffusive fluxes, n_3 for equation of state and ionization calculations, and n_4 to coordinate the entire process and update the solution. This method of resource allocation is effective when the available processors are of varying computational speeds. In that case, the fastest one could be assigned to the most intensive task, and so forth. It also works if the processors are of different types. Any available vector processors could be used to calculate flux term (which can be vectorized easily), while terms/operations that cannot be vectorized easily (such as matrix inversions) can be assigned to scalar processors. This method is the preferred choice of processor allocation under the Parallel Virtual Machine (PVM) school

of parallel computing (cf. ref.[125]). However, three notable problems can be identified with this approach:

1. Ensuring that all the processors "load balanced", i.e., each complete their part of the job at the same time,

2. Difficulties if the computer memory were distributed across various processors (as it is in the case of the machine that was used in this work - a "Beowulf cluster", or the SGI Origin 2000 system),

3. Scalability: the code has to be rewritten if the number of available processors change.

Due to the abovementioned difficulties, it is better to follow the domain decomposition method of parallel computing for this work.

3.10.2   Domain Decomposition

In this technique, the computational domain is divided into smaller domains, and these smaller domains are assigned to each of the available processors. Each processor only computes the solution in the domain it is assigned. This offers advantage on all of the three problem fronts listed above:

1. If the domain of each processor is roughly of the same size, then all processors will finish one time step at roughly the same time, and if necessary, communicate with each other about the updated solution. This feature, often termed as "load balancing" ensures maximum utilization of the available computing power,

2. Domain decomposition works for either shared memory or distributed memory systems,

3. With domain decomposition, transporting the code across computers with varying number of processors is a relatively easy task.

Message Passing

If domain decomposition is used with shared memory systems, there is no overhead cost for communication (except possibly if memory access slows down). However, in distributed computing systems like the "Beowulf" clusters (which are very popular because of their scalability and inexpensive nature), there is a need for communication between processors.

In order to estimate the values at time t near the boundaries, processors require knowledge of variables (at time $t - \Delta t$) that lie just outside the boundaries of their domain. Under the current discretization scheme, each processor needs exactly one row of cells from each of its neighboring processor's domain, as illustrated in Fig.(3.10.2).

It is important to note that inter-processor communication is *significantly* slower than the computational speed of a processor itself. There are two factors to this: the first is latency, the time it takes between when a processor sends a request for data and when it receives it; the second is bandwidth, which determines the rate of transfer of information between the processors. Therefore, care must be exercised to minimize this overhead. In this work, we use the widely-accepted Message Passing Interface (MPI) standard [126] to handle these inter-processor communications in a reasonably efficient manner.
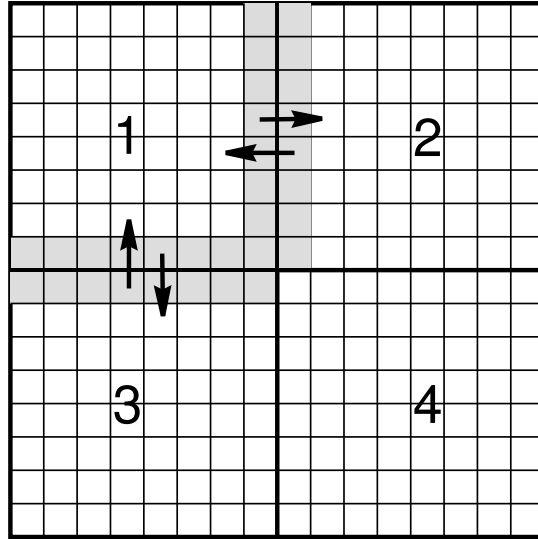
Figure 3.9: Information sent and received by a processor

There are certain parts of the code (such as input/output, convergence checks, and estimating global time steps) that are not amenable to parallelization. This constitutes an overhead, and we assign a separate processor (termed MASTER) to handle this. All the other processors (termed WORKERS) are exclusively involved in computation of the solution within their assigned domains, or are communicating with other processors for this purpose. The schematic of the calculations in our code is shown in Fig.(3.10).
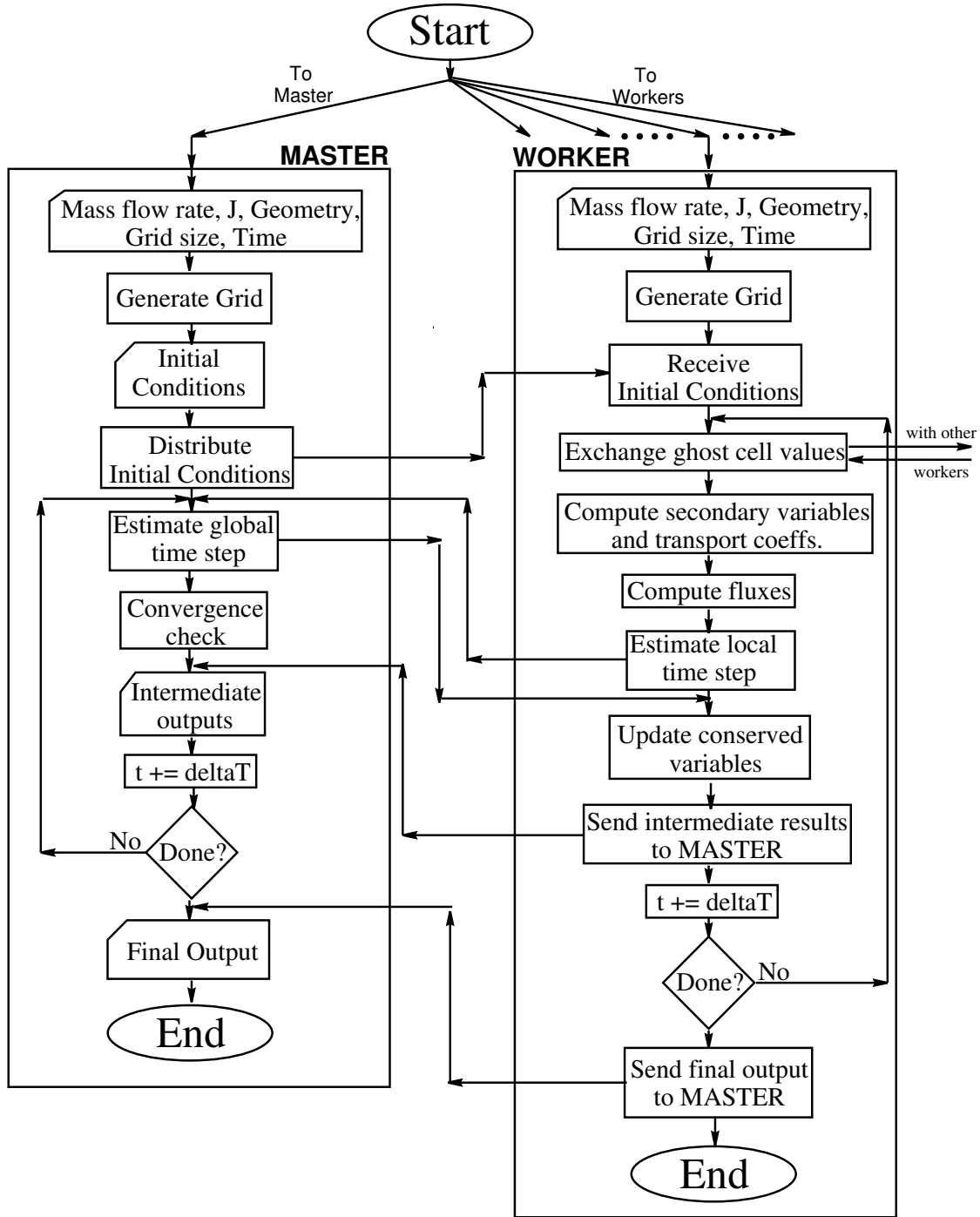
Figure 3.10: Flow chart of the parallel MHD code

3.10.3 Parallelization Results

Ideally, if a single processor takes τ amount of time to solve a problem, then N processors would only take τ/N to solve the same problem. Unfortunately, with the communication costs and overheads, this is not possible. In order to verify the effectiveness of the MPI algorithm with domain decomposition for parallelization, the 2-D heat diffusion heat equation

$$\frac{\partial T}{\partial t} = \nabla^2 T \, , \tag{3.48}$$

was solved on a 500×500 grid. This domain was decomposed into several parts, and the speed up from a single processor calculated was noted. The results from these tests are shown in Fig.(3.11).
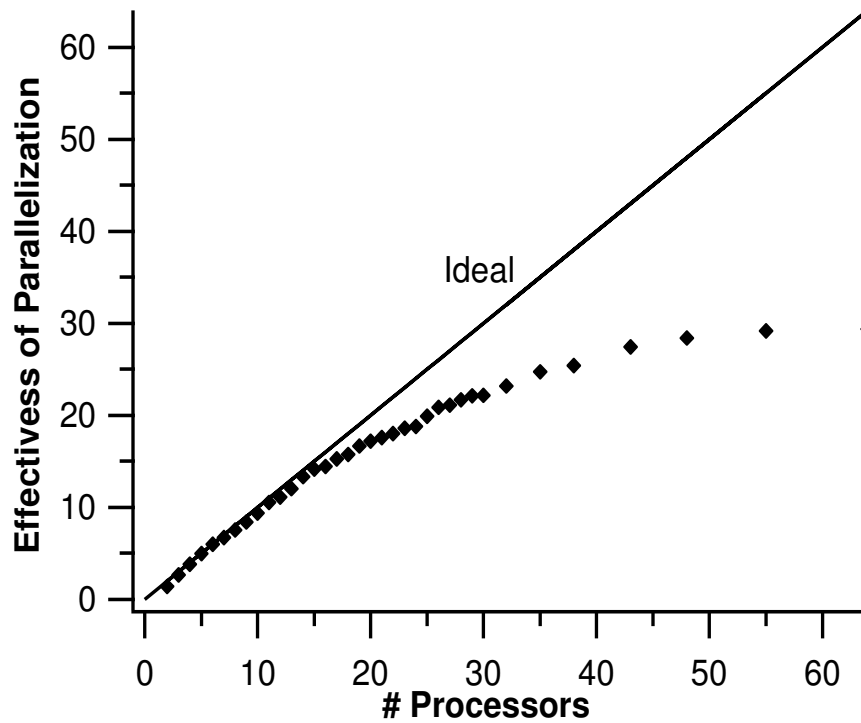
Figure 3.11: Effectiveness of parallelization by domain decomposition, for solving the thermal diffusion equation

The problem at hand, the simulation of plasma flows in a MPDT, was then run with 11 pro-

75

cessors (10 workers + 1 master). This parallelized code was 7.5 faster than the serial code. While improvements to this 70% parallelization efficiency are possible with some effort, it was not in the larger interest of this research and was not pursued.

3.11   Summary

The fundamental concepts of stability and convergence of a numerical solution were reviewed in the context of the techniques used in this work. The concept of local extremum diminishing (LED) schemes was introduced, and a new characteristics-splitting scheme, with flux-limited anti-diffusion to improve spatial accuracy was developed for the solution of the ideal MHD equations. This scheme was validated against unsteady (Riemann problem) and force-free equilibrium (Taylor state) test cases, and has demonstrated the ability the capture discontinuities monotonically, and good spatial accuracy in smooth regions of the solution. Standard central differencing techniques are used for the numerical solution of parabolic equations. These schemes are implemented on a non-orthogonal structured mesh, and computed on a parallel computing system. The next two chapters will discuss the applications of this code to simulate plasma flows in real MPDT/LiLFA configurations.

Chapter 4

GAS-FED MPDT SIMULATIONS

"Has anything escaped me? I trust that there is nothing of consequence which I have overlooked?"

Dr.Watson to Sherlock Holmes
in *The Hound of the Baskervilles*

This chapter describes how the governing equations developed in chapter 2 were solved, using the numerical techniques described in chapter 3, to simulate plasma flows in a gas-fed self-field MPDTs. The purpose of doing this is two-fold:

1. Validate the code by comparing its results with thrusters for which detailed experimental data exist, in order to make predictions on thrusters (such as the LiLFA) for which detailed experimental data does not exist, and

2. Aid in the understanding of thrust production and energy dissipation in gas-fed MPDTs.

The geometries of the gas-fed MPDTs chosen for simulation, and the relevant initial and boundary conditions for obtaining a solution are described in this chapter. The resulting profiles for many plasma parameters, obtained from the calculations, are compared to experimental data.

We will first simulate a MPDT configuration that is simple but without much experimental data, and then move on to a more complicated geometry for which there is more data.

4.1 Villani-H Thruster

The first geometry chosen for this simulation was one of the series of constant area coaxial thrusters used by Villani[18], shown in Fig.(4.1). The simplicity of its geometry makes it an attractive choice to validate a numerical code.

4.1.1 Geometry

The computational domain for simulating the flowfield in this thruster is shown in Fig.(4.2). Due to the assumption of axisymmetry, only half of the cross section, starting from the centerline (surface #1), had to be included in the simulation.

In this particular case, the cathode and the anode radii were 0.95 cm and 5.10 cm respectively. The cathode and the anode lengths were 26.4 cm and 20.0 cm respectively. For simplicity, the hemispherical tip of the cathode was represented as a flat tip (surface #8) in the simulation. For the same reason, the anode in the simulation has a sharp corner (interface of surfaces #4 and #5), instead of the rounded corner of the actual anode.

The location of propellant injection ports in the real thruster are shown in Fig.(4.1). Due to the complexity of the physical processes near the inlet region in MPDTs (to be discussed in §4.1.2), the simulation has pre-ionized propellant entering the domain uniformly (surface #6).

The real thruster would operate either in the unbounded vacuum of space or in a bounded vacuum of a test chamber. However, the computational domain has to be restricted to something much smaller in size (surfaces #2 and #3). In this case, it is truncated at one cathode length downstream of the tip of the cathode (52.8 cm), which is more than three anode diameters downstream of the anode plane. Issues regarding this truncation are discussed in §4.1.2.
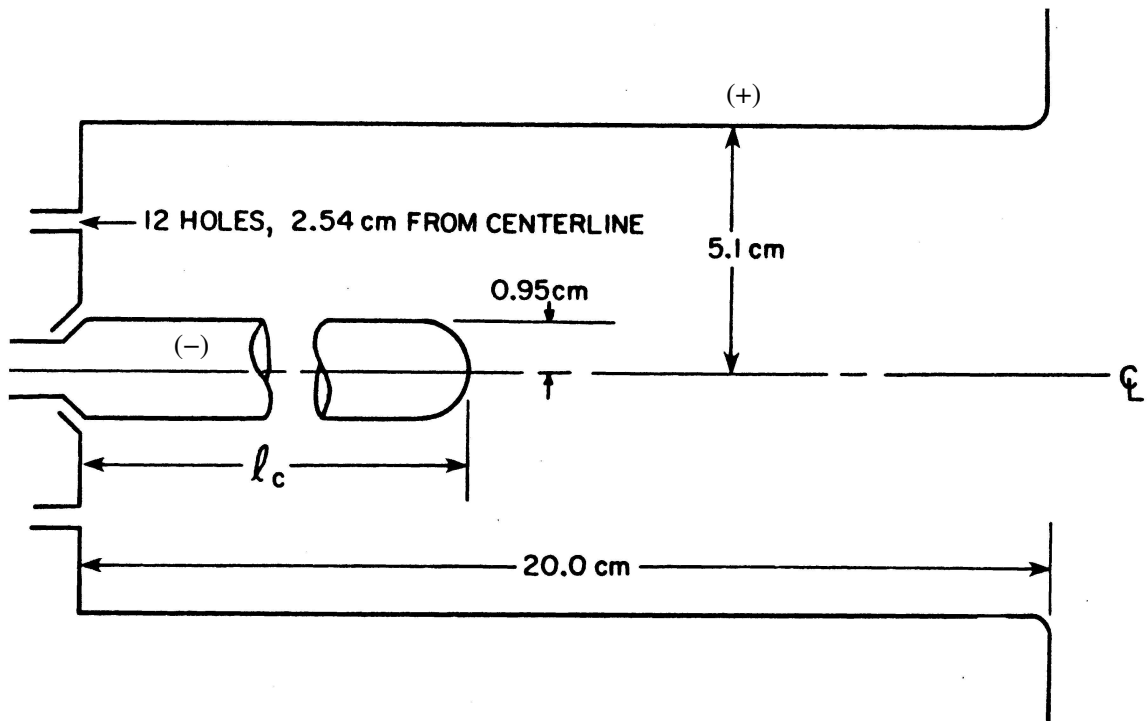
Figure 4.1: Geometry of the thruster chosen for simulation ($l_c = 26.4$ cm)
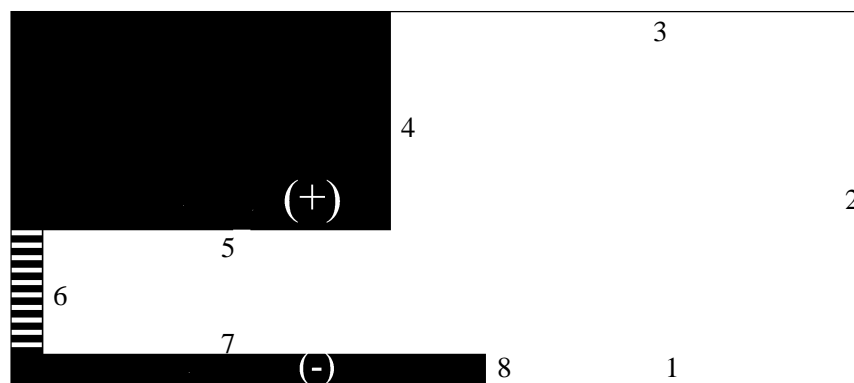
Figure 4.2: Schematic of the computational domain (not to scale)

4.1.2 Boundary Conditions

The set of governing equations (eqns.(3.36)) describe the evolution of many types of drastically different plasma flows. It is the role of the boundary conditions to distinguish one problem from another. For the particular MPDT simulation at hand, there are eight boundaries in the computational domain (see Fig.(4.2)), and they are of various types. This section will discuss the estimation of the convective and dissipative terms at each type of boundary.

Flow Properties

Freestream

The computational domain is assumed to be large enough such that there are no normal gradients in any of the flow properties at the free stream boundaries (surfaces #2 and #3).

Solid Walls

In reality, a sheath is formed at the interface of the plasma and the solid boundaries (surfaces #4, #5, #7, and #8). However, the sheath is a non-quasineutral region, and the fluid theory is not applicable there. Moreover, the size of the sheath region is typically of the order of a few Debye lengths, making it too small to be resolved by conventional grids. Therefore sheaths are currently ignored in this simulation. Discussion on inclusion of this effect will be made in §6.

At solid boundaries, all convective fluxes into the wall, given in eqn.(2.58), are zero because $\mathbf{n} \cdot \mathbf{u} = 0$.

However, diffusive fluxes are nonzero. To calculate thermal conduction into a wall, the equations require that either the temperature of the wall, or the net heat flux to the wall itself, be specified. Ideally, the simulation would self-consistently and continuously compute the heat transfer from the plasma to the wall, then the heat transfer within the metallic conductor, then calculate the temperature distribution of the wall, and from that information recompute the heat transfer from the plasma to the wall. Clearly, these calculations are computationally expensive, and may

be impractical. However, there isn't sufficient data to make good estimates of either of those quantities. Unlike the LiLFA (described in §1.3, and in refs.[40, 39]), high-power, inert gas, self-field MPDTs are generally operated in a quasi-steady mode, in which the pulse length are ~ 1 ms. The heat capacity of the plasma is typically not high enough to raise the temperature of the electrodes significantly in that duration. It is possible that there is a very thin layer that is hot enough to emit thermionically. Unfortunately, there have been no known reliable measurements of heat transfer or electrode temperature distribution in a quasi-steady pulse. In reality, there may be a thermal boundary layer in which the temperature varies from a few hundred Kelvin to more than an eV in a very small distance. Such sharp gradients may not be resolvable in simulations. Therefore judicious estimates for heat transfer or wall temperature has to be made. The results in §4.1.4 were obtained with the temperature of the wall fixed at 2500 K.

Centerline

At the axis of symmetry (surface #1), there are no radial convective fluxes. Moreover, there are no radial gradients. Therefore, there is no thermal conduction across the centerline.

Inlet

At the inlet (surface #6), a specified mass flow rate of the propellant enters at a specified temperature at sonic conditions. In reality, the propellant is injected as neutral gas at room temperature, and it gets almost fully ionized within a few millimeters from the inlet[98]. Classical theory cannot explain this high rate of ionization, and it has been proposed[127] that a non-Maxwellian electron energy distribution, resulting from plasma microturbulence, is the cause for this. Since this process cannot be modeled by fluid theory, the inlet temperature is chosen to be high enough (1.0 eV) such that the propellant is sufficiently ionized. Effectively, the backplate of the numerical model is not the true backplate, but a region located few millimeters downstream of it.

On this issue, the present simulation distinctly differs from that of ref.[68], and ref.[63]. In both these simulations, the propellant is injected at close to room temperatures, and ionization is allowed

to develop in a classical fashion. Therefore, in both ref.[68] and ref.[63], the plasma is only weakly ionized through most of the thruster channel. However, experimental measurements[98, 128] show that the propellant is fully ionized upstream in the channel. Therefore, in the present simulation, the plasma is set to be fully ionized at the inlet.

Field Properties

Freestream

The computational domain is chosen to be large enough such that all the current is enclosed within the domain. Thus, from Ampère's law, the magnetic field at the free stream boundaries (surfaces #2 and #3) is zero. Note that if the domain is too small making this assumption unreasonable, the simulation will yield unphysical results. For instance, the gasdynamic pressure is obtained by subtracting the contributions of magnetic field energy and kinetic energy from the total energy (refer to §2.3.4). If the magnetic field is artificially set to zero at the freestream boundaries, then there will be a corresponding unphysical increase in the gasdynamic pressure. Therefore, the domain has to be large enough to make this assumption reasonable.

Solid Walls

At all other boundaries, the magnetic field is computed purely from Faraday's law. Using Stokes' theorem it can be written as,

$$\int_A \frac{\partial \mathbf{B}}{\partial t} \cdot d\mathbf{A} = - \oint_C \mathbf{E} \cdot d\mathbf{l} \, . \tag{4.1}$$

In the cell-centered scheme used in this work, eqn.(5.1) implies that the evolution of the magnetic flux is specified by the contour integral of electric field around the cell. Therefore, the only information required is the electric field drop along the boundaries.

From classical electromagnetic theory[129], the jump in the magnetic field, $\mathbf{H}_2 - \mathbf{H}_1$, across an interface between two media has to satisfy the relation,

$$\hat{\mathbf{n}} \times (\mathbf{H}_2 - \mathbf{H}_1) = \mathbf{J}_s \, , \tag{4.2}$$

82

where $\mathbf{J}_s$ is the surface current per unit length. Due to the no mass flux condition, the potential drop at a wall (surfaces #4, #5, #7, and #8) is entirely resistive, and is given by,

$$\mathbf{E}_w = \eta_w \mathbf{j}_w \ . \tag{4.3}$$

At conducting boundaries (surfaces #4, #5, #7, and #8), all the current entering the discharge flows at the surface, at least in the transient case. Therefore, even though resistivity, η_w, for most conductors is very small compared to the plasma resistivity (in the 1 to 3 eV range - see fig.(2.3)),

$$
\begin{aligned}
\eta_{\text{plasma}} &\sim \mathcal{O}\left(10^{-3} - 10^{-4}\right) \text{Ohm.m} \ , \\
\eta_{\text{copper}} &= 1.7 \times 10^{-8} \text{ Ohm.m} \ , \\
\eta_{\text{tungsten}} &= 5.6 \times 10^{-8} \text{ Ohm.m} \ ,
\end{aligned}
\tag{4.4}
$$

the surface electric field is significant, due to the large current density in the transient case. In a true steady state, after the magnetic field has diffused into the conductor, the surface potential drop decreases to zero.

At insulated boundaries, the magnetic field diffuses into the wall instantaneously. Therefore, the jump in the magnetic field, and subsequently the surface current, is zero.

Centerline

At the axis of symmetry (surface #1), the inductive component of the electric field is zero because there is no flow across it. The resistive component can be related to the magnetic field from the point next to $r = 0$ using a simple Taylor series expansion, and is found to be,

$$E'_z|_{r=0} = \eta j_z|_{r=0} = \eta \frac{4 \left. B_\theta \right|_{\Delta r/2}}{\mu_o \Delta r} \ . \tag{4.5}$$

Inlet

At the backplate, which also serves as the inlet (surface #6), the total voltage drop is set as the boundary condition. Emulating a true constant current circuit, this applied voltage is adjusted every time step to maintain the specified amount of current to flow in the channel.

4.1.3 Initial Conditions

The governing equations (3.36) also require that the initial spatial distribution of the quantities be prescribed. The code is typically started with the entire domain filled with a background pressure of 10^{-4} Torr at a temperature of 300 K.

Then, the inlet boundary conditions, which represent a specified mass flow rate of fully ionized plasma, are imposed. After this plasma has filled the thrust chamber, the voltage at the backplate is made finite, introducing the effects of current and the magnetic field into the problem. For the calculations shown in §4.1.4, the current increased from 0 to 15 kA in $\sim 5\mu$s, and this rate is controlled by the adjustments to backplate voltage every time step.

As the arc hears the propellant, its ionization level (Z) and the ratio of specific heats (γ) change rapidly (see figs.(2.10,2.8)). If the current rise rate (dJ/dt) is too high, there may be a need to temper these rapid changes in the first few microseconds. For instance, let γ^* be the calculated value of γ at a time level $n + 1$, and γ^n be the old value at time level n. Then, the value of γ used at time level $n + 1$ is:

$$\gamma^{n+1} = \{\alpha\gamma^*\} + \{(1 - \alpha)\gamma^n\}\ , \tag{4.6}$$

where α is a relaxation parameter between 0 and 1. A similar method is used for introducing ionization effects.

4.1.4 Results

The results shown in this section are for the geometry in §4.2.1, with argon flowing in at 6.0 g/s and a discharge current levels of 15.0 kA and 20.0 kA. The J = 15.0 kA case corresponds to nominal operating conditions for the MPDT, since, from eqn.(2.8), $\xi = 1.0$. The J = 20.0 kA case corresponds to $\xi = 1.4$. The calculated profiles of various relevant quantities are shown in this section, with some comparisons to relevant measurements.

Density

The electron number densities within the chamber range from $\simeq 1 \times 10^{21}/m^3$ near the anode region, to $\simeq 3 \times 10^{21}/m^3$ near the cathode (see Fig.(4.3-I)). This increase may be attributed to the radial pumping force, $j_z B_\theta$, which pushes the plasma away from the anode, towards the cathode. This trend has been observed in experiments[28] and in previous simulations[30] in various MPDTs. As expected, this effect increases with increasing current, as seen in Fig.(4.3-I).
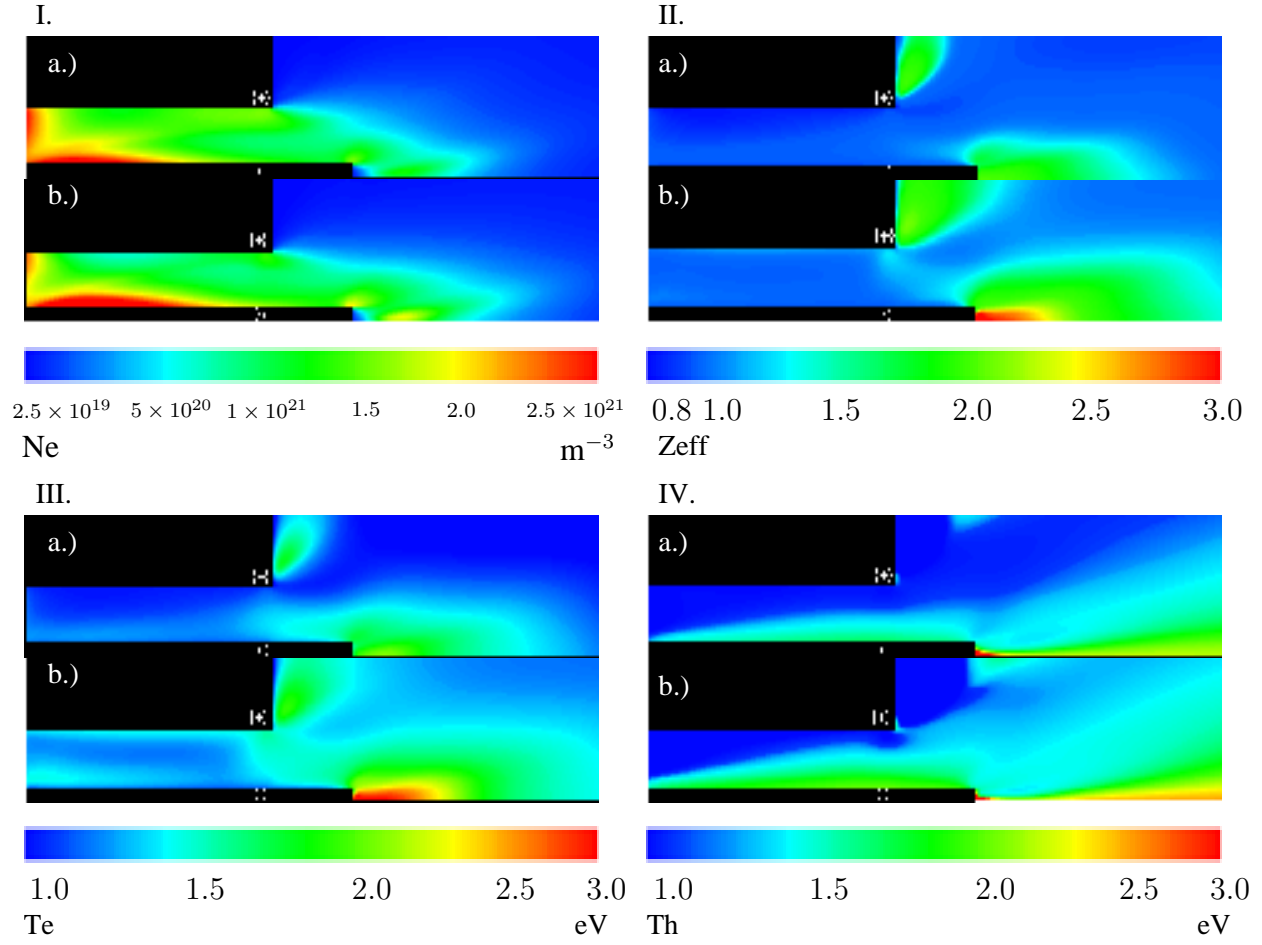
Figure 4.3: Panel I. shows the calculated values of electron number density (m^{-3}). Panel II. shows the calculated values of effective ionization fraction. Panel III. shows the calculated values electron temperature (eV). Panel IV. shows the calculated values ion temperature (eV). In each panel, the calculated values are shown for two different values of current: a.) J = 15.0 kA, and b.) J = 20.0 kA. The massflow rate $\dot{m}$ = 6.0 g/s or argon in all cases.

Ionization Levels

The effective ionization fraction is,

$$Z = \frac{n_e}{\displaystyle\sum_{i=0}^{i=N} n_i} \ ,$$ (4.7)

where n_e is the electron number density, and n_i is the density of the ith ionized species. The resulting distribution is shown in Fig.(4.3-II). The presence of Ar-III and a small amount of Ar-IV in the plume is in agreement with experimental observations (cf. ref.[12]) for these operating conditions. As expected, the fraction of higher levels of ionization increases with increasing current. From Fig.(4.3-II), it can be seen that the effective ionization fraction in the chamber is $Z \simeq 1.0$, indicating that the propellant is in a sufficiently high state of ionization to carry the current.

Electron Temperatures

The distribution of electron temperatures is shown in Fig.(4.3-III). Within the thrust chamber, T_e varies from about 1.0 to 1.5 eV. The lower values near the anode are probably due to the lower value of ηj^2 at higher r, and large heat transfer to the walls. Nevertheless, these numbers are in general agreement with measurement[130] at these operating conditions for argon MPDTs.

The hot spot at the tip of the anode, where T_e is about 2.0 eV, is probably due to the strong current attachment in that region, causing augmented values of Ohmic heating. The hot spot at the tip of the cathode, where T_e is about 2.0 eV for the $\xi = 1.0$ case and about 2.8 eV for the $\xi = 1.4$ case, may be due to stagnation, when the kinetic energy of the electron fluid is reduced and appears as thermal energy.

Ion Temperatures

The distribution of ion temperatures is shown in Fig.(4.3-IV). Within the thrust chamber, T_h varies from about 1.0 to 1.5 eV for the $\xi = 1.0$ case, and reaches 2.0 eV for the $\xi = 1.4$ case. The hottest

region of ion temperature occurs at the axis of symmetry. At the center of the cathode tip (r=0), the ion temperature exceeds 4.0 eV. A partial explanation for this region of high temperature may once again be related to stagnation. Another possible explanation could be that the axisymmetric assumption causes thermal conduction at the centerline to go to zero. If there are symmetry breaking oscillations in reality, then there would be thermal conduction that would reduce the temperature in that region[131]. Nevertheless, these numbers are reasonable for these operating conditions for argon MPDTs.

Velocities

The distribution of axial velocities in the domain are shown in Fig.(4.4-I). At the anode plane, the axial velocity ranges from 8.0 km/s to 15.0 km/s for the $\xi = 1.0$ case, and up to 18.0 km/s for the $\xi = 1.4$ case. The maximum velocity increases to a maximum (of 17.0 km/s for the $\xi = 1.0$ case, and up to 21.5 km/s for the $\xi = 1.4$ case) slightly further downstream. As expected, the velocity increases with decreasing radius, because of the similar trend in $\mathbf{j} \times \mathbf{B}$. The mass averaged velocities, (7.2 km/s for the $\xi = 1.0$ case and 13.5 km/s for the $\xi = 1.4$ case, is typical for MPDTs at this operating condition (see §4.2.3).

I.

a.)

b.)

1500   5000   10000   15000   21000
Vz   m/s

II.

a.)

b.)

0.1   0.5   1.0   1.5
Hall

III.

a.)

b.)

0.0   0.5   1.0   1.5
Anom
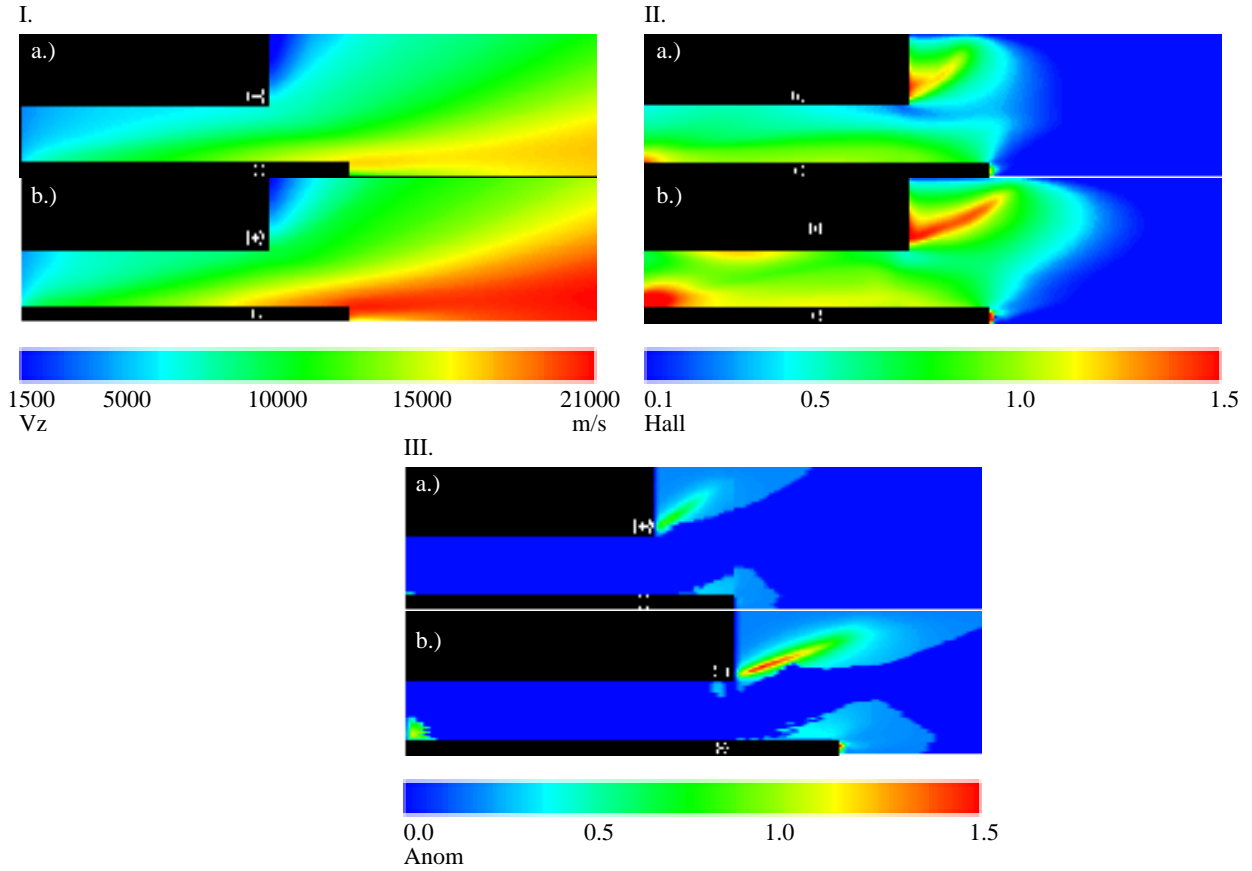
Figure 4.4: Panel I. shows the calculated values of axial velocity (m/s). Panel II. shows the calculated values of the electron Hall parameter. Panel III. shows the calculated ratios of anomalous to classical resistivity. In each panel, the calculated values are shown for two different values of current: a.) J = 15.0 kA, and b.) J = 20.0 kA. The mass flow rate $\dot{m} = 6.0$ g/s or argon in all cases.

Figure 4.5: Calculated velocity stream lines in the flow. J = 15.0 kA, $\dot{m} = 6.0$ g/s.

89
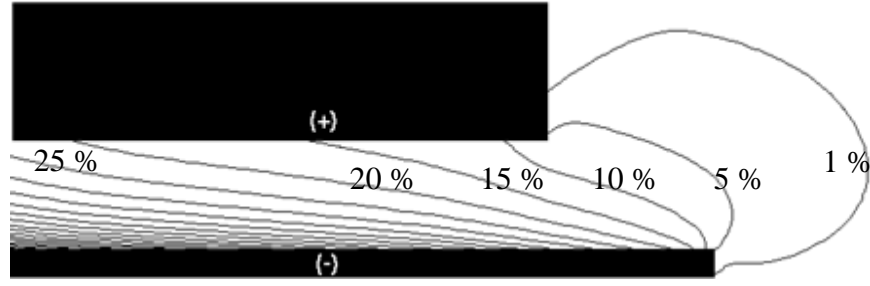
Figure 4.6: Calculated distribution of magnetic field (as % of maximum). J = 15.0 kA, $\dot{m}$ = 6.0 g/s.

To look at the effect of radial velocity on the flow, the velocity streamlines (where the velocity vector is a tangent at every point) are shown throughout the domain in Fig.(4.5) for the $\xi = 1.0$ case.

Magnetic Field & Enclosed Current

The spatial distribution of magnetic field strength in the domain is shown in Fig.(4.6), as a fraction of the maximum value. The maximum value attained, (0.26 T for the $\xi = 1.0$ case and 0.34 T for the $\xi = 1.4$ case), occurs at the intersection of the backplate and the cathode. Generally, B_θ varies as $1/r$ with radius and decreases linearly with axial distance. This is strictly true only for a uniform current distribution in the channel. However, the current and magnetic field propagate downstream via convection and diffusion, and their distributions are no longer uniform.

The enclosed current is calculated as,

$$J_{encl} = \frac{2\pi r B_\theta}{\mu_o} \ .$$

(4.8)

The measured and calculated current contours are compared in Fig.(4.7) for the $\xi = 1.0$ case. The tendency of the current lines to be blown downstream is clearly seen. This pattern is generally observed experimentally in many MPDT geometries. However, it is also evident that in the simulation the current has not propagated as far downstream as in the experiment. A possible explanation

90

is that the current in the experiment was allowed to attach on the outer surface of the anode, while
it was not permitted to do so in the simulation.
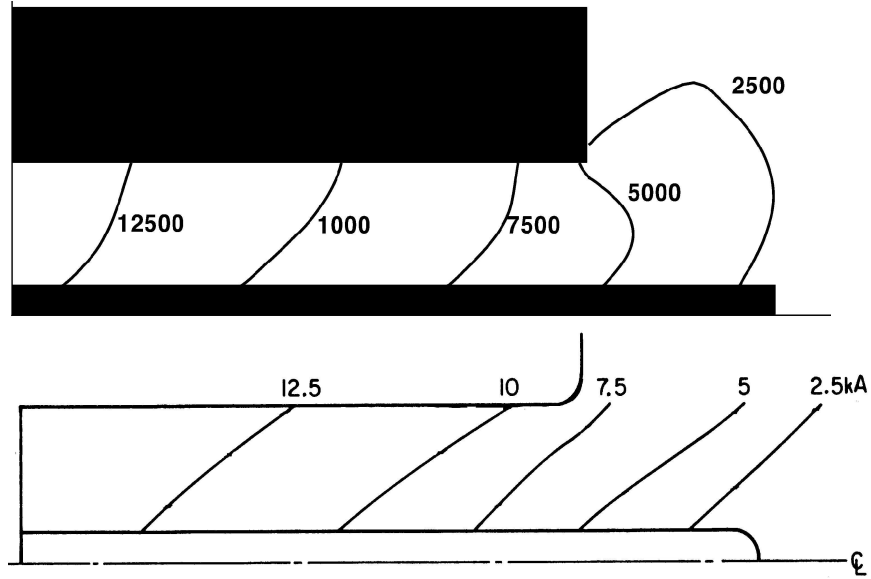
Figure 4.7: Calculated (top) and measured (bottom) current contours. J = 15.0 kA, $\dot{m}$ = 6.0 g/s.

Electric Field & Potential

The calculated values of radial and axial electric fields are shown in Fig.(4.8) for the $\xi = 1.0$ case.
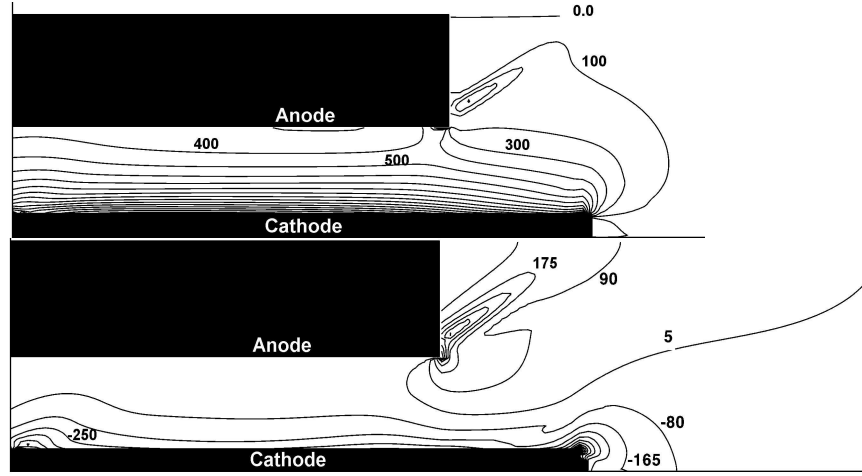
Figure 4.8: Radial and axial electric field contours (in Volts/m). J = 15.0 kA, $\dot{m}$ = 6.0 g/s.

By definition, the relationship between a static electric field and its potential is,

$$\mathbf{E}\left(r, z\right) = -\nabla\phi\left(r, z\right) \ . \tag{4.9}$$

So, the potential difference between any two points can be calculated as,

$$\phi\left(r_2\right) - \phi\left(r_1\right) = -\int_{r_1}^{r_2} \mathbf{E} \cdot d\mathbf{r} \ ,$$

$$\phi\left(z_2\right) - \phi\left(z_1\right) = -\int_{z_1}^{z_2} \mathbf{E} \cdot d\mathbf{z} \ . \tag{4.10}$$

In this calculation, the anode was set at a reference potential of 0. The potential at every other point in the domain was computed using eqn.(4.10). It is important to note that the predicted values of voltage do not include electrode drops, and are therefore cannot be compared to the measured value across the electrodes. They only serve to quantify the plasma part of the voltage drop. This simulation predicts a voltage drop across the plasma of 30.83 Volts. The true voltage drop is 56 Volts [18], and the difference can be attributed to the 25 Volts of anode drop that was measured. Since the experimental measurements indicate that the anode drop is 25 V, the calculated potential

contours were shifted by 25 V. Though this value is not a constant along the anode, it nevertheless allows comparison of calculations with measurements. These contours are shown in Fig.(4.9), with the unadjusted calculated values shown in parentheses. It can be seen that the region in space that corresponds to the 30 V contour in the experiment, roughly corresponds to the 33 V in the adjusted contour in the simulation. Similarly, the region in space that corresponds to the 40 V contour in experiment, roughly corresponds to the 45 V adjusted contour in calculation. Again, it is important to bear in mind that the calculated contours were shifted by an estimate for anode drop. The purpose of this is not to obtain any insight into the operation of the device, but merely to check if the simulation results are reasonable. Having verified it to be so, such adjustments will not be made in the subsequent calculations.
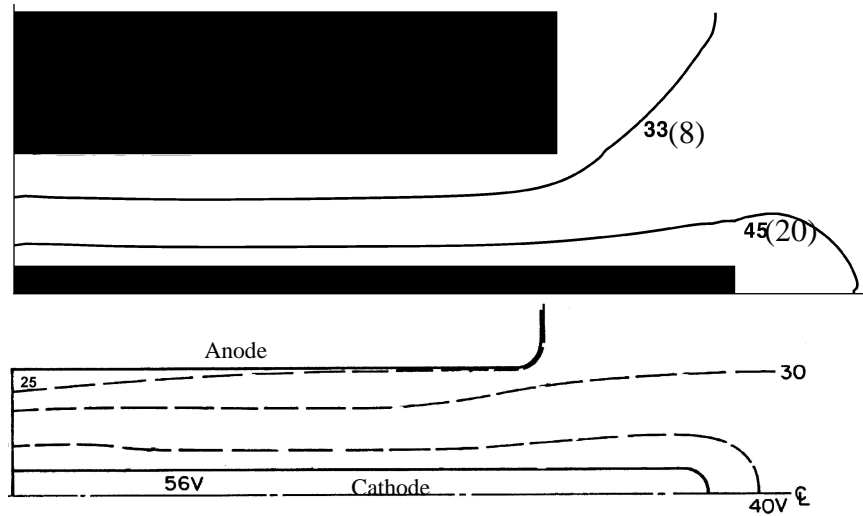
Figure 4.9: Calculated (top) and measured (bottom) potential contours. The numbers in paranthesis in the calculated contours are the values that are unadjusted for measured anode drop. $J = 15.0$ kA, $\dot{m} = 6.0$ g/s.

Hall Parameter & Anomalous Transport

The distribution of the electron Hall parameter in the domain is shown in Fig.(4.4-II). Within the channel, it varies from 0.3 to 1.2 for the $\xi = 1.0$ case, and up to 2.0 for the $\xi = 1.4$ case. Since the magnetic field and species temperatures increase with decreasing radius, so does the Hall parameter. Outside the channel, the Hall parameter is higher at the electrode tips than in any other region. Once again, referring to Fig.(4.6) and Fig.(4.4-III), the magnetic field is higher (cyclotron frequency is higher) and temperatures are higher (collision frequencies are lower) in those regions.

It is worth noting that these values of the electron Hall parameter are substantially lower than those observed in other MPDT configurations, such as the FSBT (mentioned in §2.2, and discussed in detail in §4.2). This is because, unlike in the FSBT where the anode is only a "lip", the anode here is along the entire length of the channel, leading to a more diffuse current attachment pattern. Moreover, the electrode lengths in this configuration are substantially longer than the corresponding dimensions of the FSBT. Therefore, there is much less canting of the current lines here than in the FSBT, reducing the pumping forces that starve the anode and increase the Hall parameter (see Fig.(4.11-e) in §4.2.3 for more on this issue.) This is consistent with the prediction of King[17] that increasing the electrode length precluded the occurrence of large Hall parameters.

As seen in Fig.(2.9), the ratio of anomalous resistivity to classical resistivity (eqn.(2.55)) is a strong function of the electron Hall parameter, beyond a cutoff, $u_{de}/v_{ti} \geq 1.5$. The ratio of anomalous resistivity to classical resistivity for this case is shown in Fig.(4.4-III). For the $\xi = 1.0$ case, since the Hall parameter is not very large in this particular geometry, the overall effect of anomalous transport is limited (cf. Fig.(2.9)). For the $\xi = 1.4$ case, the ratio of anomalous resistivity to classical resistivity exceeds 1.0 at the cathode base, and reaches 1.75 near the anode.

Thrust

By definition, the thrust is computed using the following relation,

$$T = \int_A u_z \left(\rho \mathbf{u} \cdot d\mathbf{A} \right) \,, \tag{4.11}$$

where the integral is performed over all the boundaries in Fig.(4.2).

As discussed in §2.2, the analytical expression for thrust is,

$$T = \frac{\mu_o}{4\pi} \left(\ln \frac{r_a}{r_c} + A \right) J^2, \tag{4.12}$$

where r_a and r_c are the radii of the anode and the cathode respectively. For this particular configuration, the appropriate value for the current attachment parameter, A, is 0.15 (refer to Villani[18]). Notice that A is much smaller than $\ln (r_a/r_c)$ (which is 1.68).

Using eqn.(4.15), the code predicts a thrust of 42.9 N. This compares well with the analytically calculated value is 41.2 N.

4.1.5 Summary

For the first set of simulations to validate this code, a simple constant area geometry was chosen for simulation. The drawback of this choice of geometry was the dearth of data available for it. In fact, the only available data were the current and potential contours. However, for those quantities, the results of the simulation were in good agreement with measurements. As far as the other plasma parameters, their values and distributions are within the reasonable range of values observed in experiments on similar geometries for these operating conditions.

Other researchers[61, 62, 63, 64, 65, 33] have found the ideal equation of state suitable to simulate MPDTs at lower current levels ($J^2/\dot{m} \leq 25.0$ kA^2/g/s). However, for higher current levels ($J^2/\dot{m} = 37.5$ to 66.7 kA^2/g/s in the simulations in this section), there are insufficient energy sinks with the ideal equation of state, and the simulation did not converge. A real equation of state was crucial to obtaining a realistic and stable solution.

The purpose of this set of simulations was to illustrate the application of the numerical techniques developed in this thesis to solve the governing equations of the physical model relevant to the simulation of plasma flows in real MPDT functioning at nominal operating conditions. Now that this has been accomplished, the stage is set to tackle a more interesting thruster that has been extensively studied.

4.2   Full-Scale Benchmark Thruster

The Princeton full-scale benchmark thruster (FSBT) is a MPDT that has been the subject of many experimental investigations [16]-[43] over the past three decades. Yet, there has not been a detailed numerical simulation of this device. It is now insightful to revisit this device with the improved numerical methods and computing capability discussed in §3 (also see refs.[132, 133, 134]), by comparing experimental measurements to results from this code.

For the purpose of this dissertation, the goal of this comparison is to validate this code so that it can be used to study the lithium Lorentz force accelerator (LiLFA)[40]. This study is presented in chapter 5.

Though the simulation technique described in chapter 3 remains unchanged, each thruster may require a unique treatment of boundary conditions. In §4.2.2 the boundary conditions imposed on the solver to calculate the flowfield in the FSBT will be discussed. In §4.2.3 the results from the simulation of plasma flows in the FSBT will be presented, and compared the results to experimental measurements. In §4.2.4 these aforementioned results will be used to investigate some underlying physical processes in the FSBT.

4.2.1 Geometry

A schematic of the Princeton full-scale benchmark thruster[43], with the relevant dimensions are given in Fig.4.10. For simplicity, the rounded corners of the anode lip and the cathode were truncated in the simulation. Note that in the simulation the thruster contains four mass injection ports - one at the base of the cathode (as in Fig.4.10) at a 45° angle, and three others r = 2cm, 3 cm, and 4 cm through the backplate directed normally into the chamber. In reality, several mass injections schemes were tested in experimental studies, and the version shown in Fig.4.10 has only one port through the backplate.
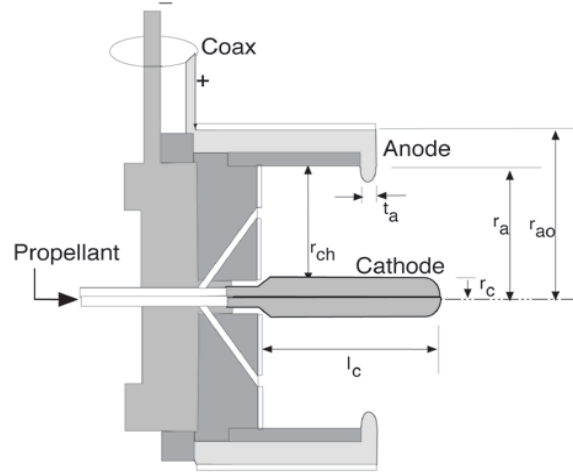
Figure 4.10: Princeton full-scale benchmark thruster, where r_c= 0.95 cm, r_a= 5.1 cm, r_{ao}=10.2 cm, r_{ch}= 6.4 cm, t_a= 0.95 cm, and l_c= 10.0 cm.

4.2.2 Boundary Conditions

The method used for estimation of the convective and dissipative terms at various boundaries remains mostly the same as in §4.1.2, where the details are found. However, unlike the Villani-H thruster discussed in §4.1.2, the FSBT has an insulated chamber. Therefore, the focus of this

97

section will be on the boundary between the plasma and the insulator.

Since all the enclosed current is downstream of the insulator (backplate and the inner wall of the chamber, in Fig.4.10), the stream function, $\psi = rB_\theta = \mu_o J_{tot}/2\pi$ is a constant at any given time at this boundary, and it depends only on the total current. The electric field along the backplate, required for Faraday's law, is then

$$E_r(r, 0) = E_r(r, \Delta z) + \Delta z \left(\frac{1}{r} \frac{\partial \psi}{\partial t} - \frac{\partial E_z}{\partial r} \right), \tag{4.13}$$

and the electric field along the chamber inner wall is

$$E_z(R_{ch}, z) = E_z(R_{ch} - \Delta r, z) + \Delta r \left(\frac{1}{r} \frac{\partial \psi}{\partial t} + \frac{\partial E_r}{\partial z} \right). \tag{4.14}$$

The abovementioned conditions, along with the ones described in §4.1.2 provide sufficient tools to calculate the flowfield in the FSBT.

4.2.3 Results

The relevant results from the simulation of the FSBT will be presented here. All the discussion in this chapter will be limited to argon propellant, with a mass flow rate of 6.0 g/s. The current in the simulations presented in this chapter varies from 12.0 kA to 20.0 kA (see Table 4.1) at this mass flow rate. The case with a total current of 16.0 kA (at $\dot{m} = 6.0$ g/s) corresponds to the nominal operating condition of $\xi \simeq 1.0$ (discussed in §2.2 - cf. ref.[76]), and therefore will be of special importance to this discussion.

A summary of some important results are presented in Table 4.1.

Density

The electron number density contours within the chamber are shown in Fig.(4.11-a), for the ξ = 1.09 case. It is to be noted that n_e increases towards the cathode inside the chamber. This is attributed to the action of the radial pumping force, $j_z B_\theta$, which pushes the plasma towards the

Current (kA)	ξ	T_{calc} (N)	T_{exp} (N)	$T_{EM}/T_{tot}(\%)$	V_{plasma} (V)	P_{in} (kW)
12.0	0.82	33.3	30.8	60	28.0	336.0
16.0	1.09	51.2	50.4	75	36.0	576.0
17.5	1.19	59.3	61.5	78	49.4	864.5
20.0	1.36	77.0	82.7	80	62.4	1248.0

Table 4.1: FSBT Simulation Summary ($\dot{m}$ = 6.0 g/s for all cases). The first column contains the current level (in kA), the second the corresponding non-dimensional value of the current, the third the calculated value of thrust (in N), the fourth the measured value of thrust (in N), the fifth the calculated ratio of electromagnetic thrust to total thrust. The sixth column contains the calculated values of voltage drop *in the plasma* (in V), and the seventh contains the calculated value of power input to the plasma (in kW).

cathode. This trend has been observed in experiments and in previous simulations[30]. The density in the thruster chamber ranges from $\simeq 2.0 \times 10^{20} \text{m}^{-3}$ near the chamber wall to $\simeq 5.0 \times 10^{21} \text{m}^{-3}$ near the cathode. Outside the chamber, on the centerline near the cathode, one also finds a region of high density ($\simeq 5.0 \times 10^{21} \text{m}^{-3}$), which is often termed as "cathode jet"[135]. In this simulation, the highest density, $\simeq 2.0 \times 10^{22} \text{m}^{-3}$, is found near the injection port on the base of the cathode. While there exist no detailed measurements of electron density in the FSBT, Turchi[135] measured them for a similar geometry (dubbed as "Configuration A") with a shorter cathode. As reported in Ref.[135], electron number densities near the cathode in the chamber, and on the centerline in front of the cathode are indeed around $\simeq 5.0 \times 10^{21} \text{m}^{-3}$ and are in accordance with the results of the simulation.

It is well known from experimental measurements[26, 28] that the anode region of the FSBT gets starved of charge carriers as the current is increased. This trend is seen clearly in the simulations. Fig.(4.11) shows the calculated values of electron number density (m^{-3}) near the anode for J
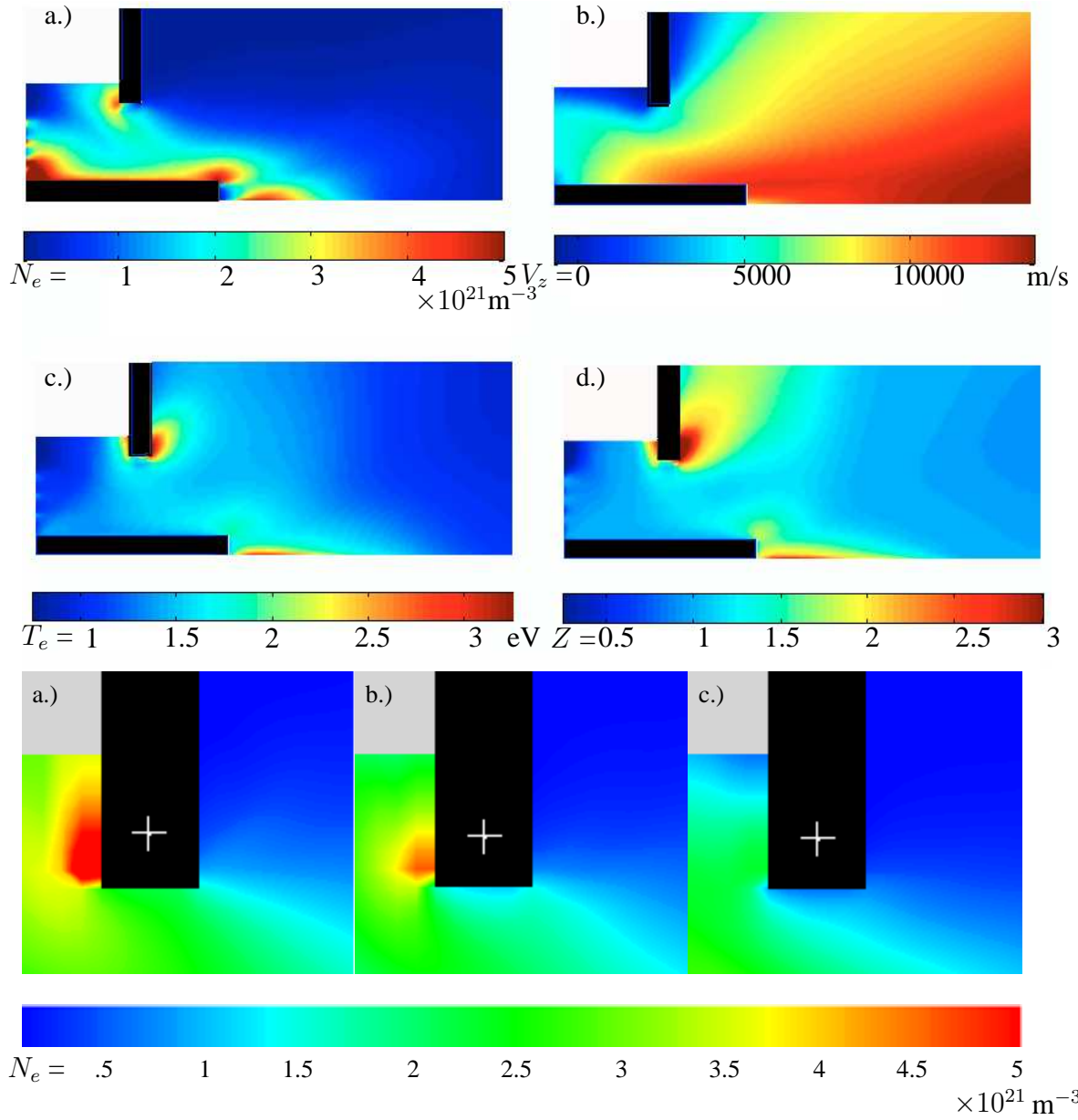
Figure 4.11: Panel a. shows the calculated values of electron number density (m^{-3}). Panel b. shows the calculated values of axial velocity (m/s). Panel c. shows the calculated values electron temperature (eV). Panel d. shows the calculated effective ionization fraction ($J = 16.0$ kA in panels a-d). Plots of the electron number density (m^{-3}) near the anode, shown in panel e ($J = 12.0$ kA), panel f ($J = 16.0$ kA), and panel g ($J = 20.0$ kA), indicate the starvation of the anode with increasing current ($\dot{m} = 6.0$ g/s in all plots).

= 12.0 kA (panel e), J = 16.0 kA (panel f), and J = 20.0 kA (panel g). This starvation could play an important role in understanding the performance-limiting onset of instabilities in the FSBT[26, 28].

Velocities

The contours of axial velocity are shown in Fig.(4.11-b). The range of values (8.0 to 13.0 km/s) is in the range of measured values of local velocities reported in ref.[130] for these conditions. On the centerline, Boyle[14] measured axial velocity increasing from 10 km/s to 13 km/s, with distance from 2 cm to 15 cm in front of the cathode. It can be seen in Fig.4.12 that this simulation also predicts a similar pattern and values.
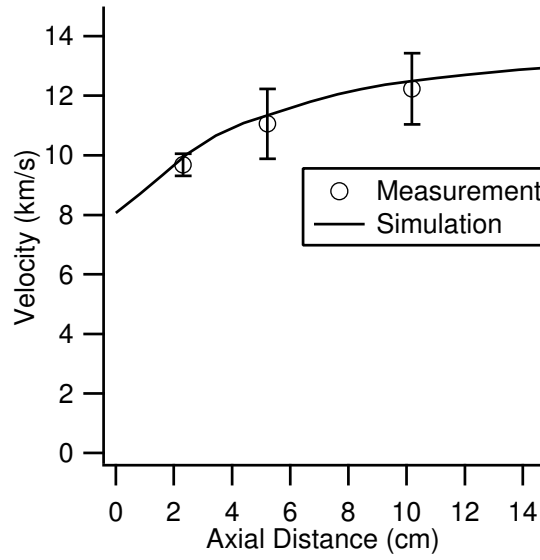
Figure 4.12: Comparison of measured[14] and calculated centerline velocities at J = 16.0 kA, $\dot{m}$ = 6.0 g/s.

Current

The calculated contours of enclosed current are shown in Fig.4.13, in comparison with experimental measurements[19]. For the sake of brevity, only the comparison at the most challenging of

101

the operating conditions listed in Table 4.1 (J = 20 kA) is shown. As evident from the figure, the simulation predicts the attachment locations of the 80%, 60% and the 40% contours accurately on both the cathode and the anode. For the 20% and the 10% lines, the attachment on the cathode is also predicted accurately. In the front face of the anode (in the plume), however, comparison is not possible because of the lack of data at that location. In any case, the continuum assumption (inherent in eqn.(2.58)) would limit the validity of the simulations in the low collisionality region of the plume.
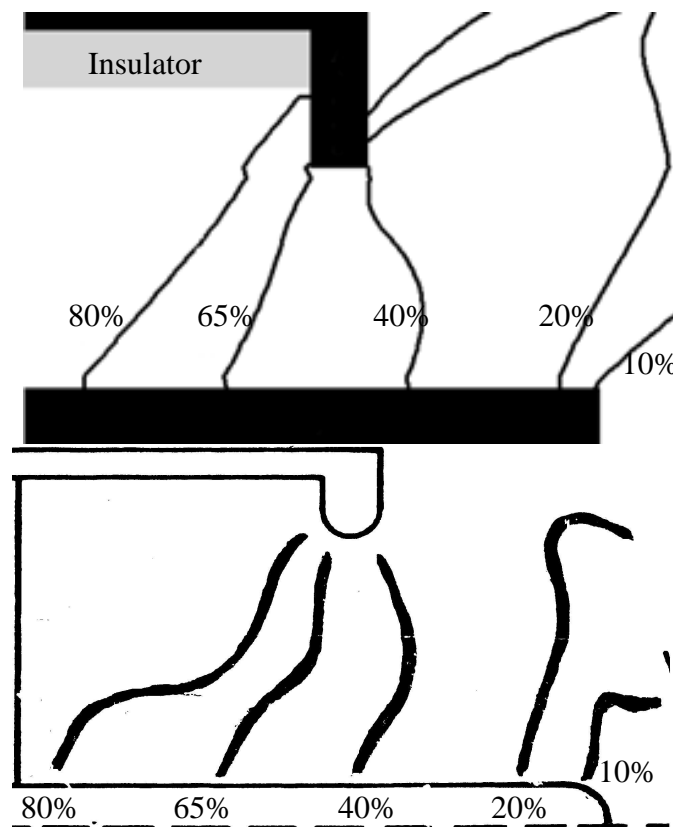
Figure 4.13: Panel "a" shows the calculated current contours for J = 20.0 kA, $\dot{m}$= 6.0 g/s, and panel "b" shows the measured current contours (obtained from Ref.[19]) at the same conditions.

Temperatures

The calculated values of electron temperature are shown in Fig.(4.11-c), for the $\xi = 1.09$ case. In the bulk of the chamber, T_e ranges from 1.0 to 1.75 eV, which is in the range of measurements in ref.[9]. The rear top end of the chamber has lowest values (0.75 eV), because it has the lowest Ohmic-heating rate. The highest values of $\simeq 3.5$ eV are found on the inner and outer faces of the anode. This can be explained by the large Ohmic heating caused by the high current density observed in that region. Diamant[28] measured temperatures around 2.5 eV near the anode at this condition, and they are in general agreement with the simulation, in that region. Temperatures of $\simeq 3.0$ eV are seen in the simulation in front of the cathode on the centerline.

For the $\xi = 1.36$ case (J = 20 kA), the near anode temperatures reach 4.5 - 5.0 eV. Measurements by Diamant[28] have shown that this is indeed the case.

Thrust and Voltage

By definition, the thrust is computed using the following relation,

$$T = \int_A u_z \left(\rho \mathbf{u} \cdot d\mathbf{A} \right) \ . \tag{4.15}$$

The calculated values of thrust are compared to measurements[43], and the results are presented in Table4.1. At the lowest current (12.0 kA, $\xi = 0.82$), the code over predicts thrust by 8%, and at the highest current (20.0 kA, $\xi = 1.36$), the code under predicts by 7%. At the nominal operating condition (16.0 kA, $\xi = 1.09$), the agreement is within 2%.

The plasma voltage drop is presented for various current levels in Table 4.1. For the nominal operating condition (J = 16.0 kA, $\dot{m} = 6.0$ g/s), this simulation predicts a plasma voltage drop of 36 V, as shown in Fig.4.14. It is important to note that the simulation did not include electrode fall voltages, and therefore one cannot compare the calculated *plasma* voltage to the measured *total* voltage[43] directly. Measurements[28] have shown repeatedly that the anode fall can be $\simeq 50$ V

at $\xi \simeq 1.0$, and this is a major energy sink in an MPDT. It is useful to note that the monotonic

increase of voltage with current is consistent with measurements[43].
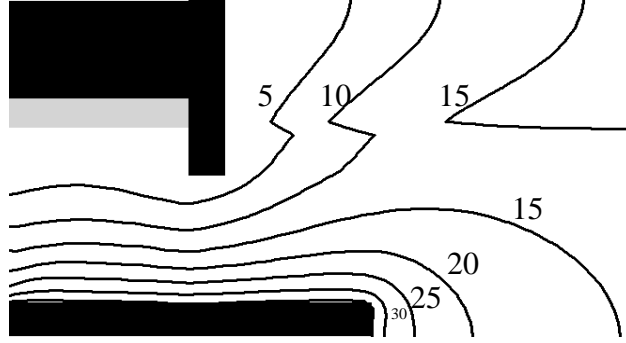
Figure 4.14: Calculated potential contours (in Volts) for J = 16.0 kA.

4.2.4   Insight into Other Physical Processes

As evident from the preceding section, this simulation has predicted many of the salient features

of the flowfield, and the results are in general agreement with measurements for many quantities.

Therefore, it is possible to delve into some underlying physical mechanisms in the MPDT. Unless

explicitly stated otherwise, the focus will be on the operation at J = 16.0 kA (at $\dot{m}$ = 6.0 g/s), since

this corresponds to the nominal operating condition of $\xi \simeq 1.0$.

Effect of the Anode Lip

The velocity streamlines in the FSBT are shown in Fig.4.15. The expansion of the streamlines past

the anode lip, and hence plume divergence, is evident from the figure. It is clear that the anode lip

is an obstruction to the streamlines, and its stagnation effect can be seen in the increased density

(Fig.4.11-a) and temperature (Fig.4.11-c) in that region.
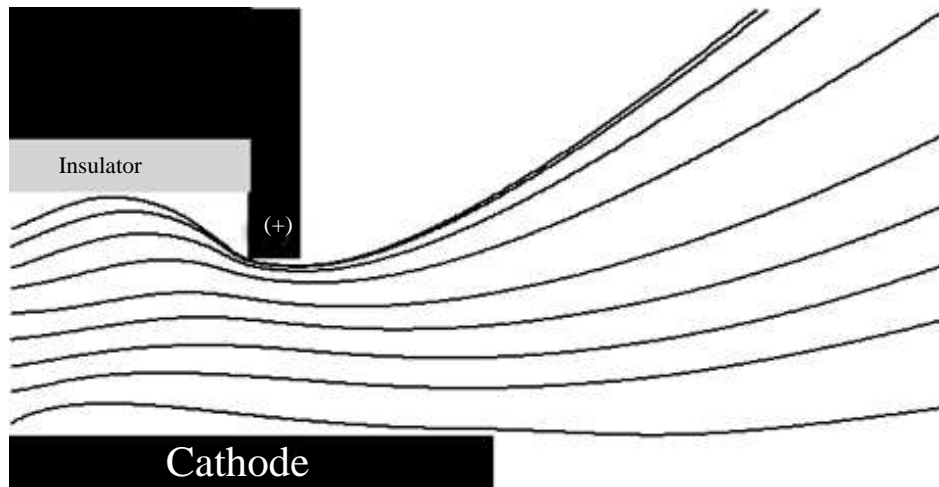
Figure 4.15: Calculated velocity streamlines for J = 16.0 kA, $\dot{m}$= 6.0 g/s.

In order to ascertain the effect of the anode lip on thrust, one needs to look at the mass flux, and the momentum flux in this thruster.

Cory[11] measured the mass flux at this operating condition for the "Configuration A" thruster (which has a similar geometry to the FSBT, but with a shorter conical cathode). The results of this simulation are compared to those measurements in Fig.(4.16). Generally, the agreement between the simulation and the data is very good. Except for the point on the centerline, the agreement is within 20%. Near the centerline, the measured mass flux is higher than that predicted by the simulation. This may be attributed to the difference in the cathode lengths in the experiment and the simulation.
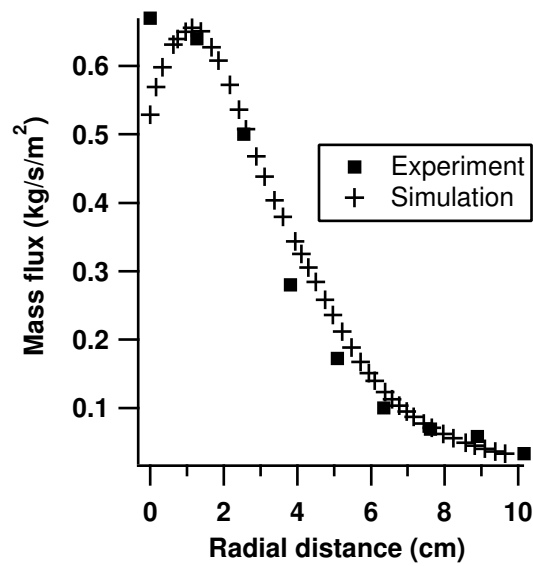
Figure 4.16: Mass flux at a distance of 12.5 cm from the anode plane. No error bars on the measurements were provided in the original work[11].

The flux of momentum was also calculated, and is shown in Fig.4.17.
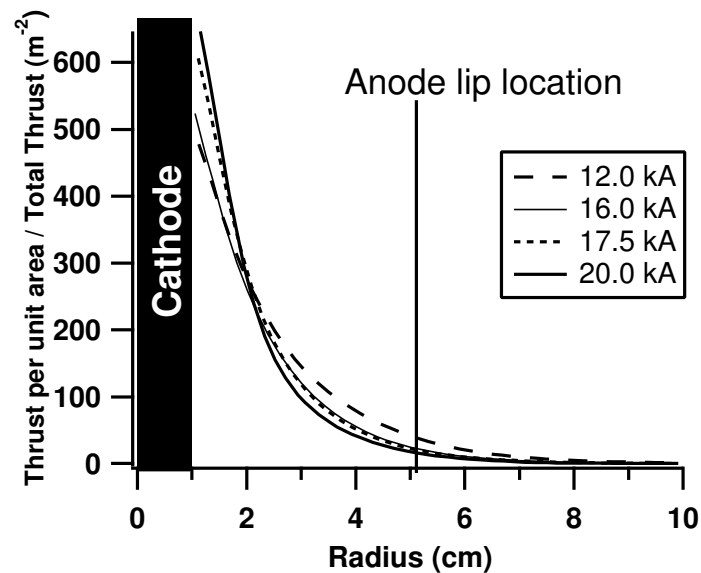
Figure 4.17: Calculated momentum flux at the cathode tip plane.

As seen in Fig.4.16, the flux of mass near the anode is relatively small. More importantly, as seen in Fig.4.17, the flux of momentum in the anode region is small compared to the cathode region. Due to a combination of the pumping force ($j_z B_\theta$) pushing the plasma towards the cathode, and the $1/r^2$ variation of the axial Lorentz force density ($j_r B_\theta$), the high speed jet is confined to the cathode region of the thruster, and the anode region does not play a significant role in the momentum flux. Furthermore, the results shown in Fig.4.17 clearly indicate that the contribution of the anode region in the thrust production decreases with increasing $J^2/\dot{m}$. Therefore, the anode lip is not a significant impediment to the production of thrust at these operating conditions.

Ionization Levels

The effective ionization fraction is shown in Fig.4.11-d. It is important to bear in mind that this simulation uses an equilibrium ionization model, and hence $Z = Z(n, T_e)$, and therefore an understanding of T_e distribution is important to understand the distribution of ionization levels. In the rear top end of the chamber, where the current density is low ($\simeq 5.0 \times 10^4 \mathrm{A/m^2}$), we find that the ionization level is low ($Z \simeq 0.25$), as expected. In the bulk of the chamber, $Z \simeq 1.0$. Near the inner face of the anode and the anode lip, where the current density is high, the effective ionization level ranges from 1.5 to 2.5. In the outer edge of the anode, current density is also very high, the ionization level is $\simeq 3.0$. The presence of these higher states of ionization (Ar-III and Ar-IV) has been shown by Bruckner[12] in the anode plane of the "Configuration A" thruster, for these operating conditions (argon at 6.0 g/s, J=16.0 kA).

Discharge Structure

In many experimental observations[16, 136] at nominal operating conditions, the luminous structure of the discharge was observed to have some invariant features, such as a "cathode jet", a luminous barrel which is larger at the base of the cathode and constricts towards the middle and

expands again at the cathode tip. All of these features can be seen in Fig.4.18. On the left panel of Fig.(4.18) are the calculated values electron density, while the right panel shows the observed argon ion emission from the discharge recorded photographically using an FSBT with transparent plexiglass walls [136]. The similarity in the calculated and observed structure of the discharge is striking. This is the first reported instance where numerical simulations of such thruster flows are compared directly to visual observations.
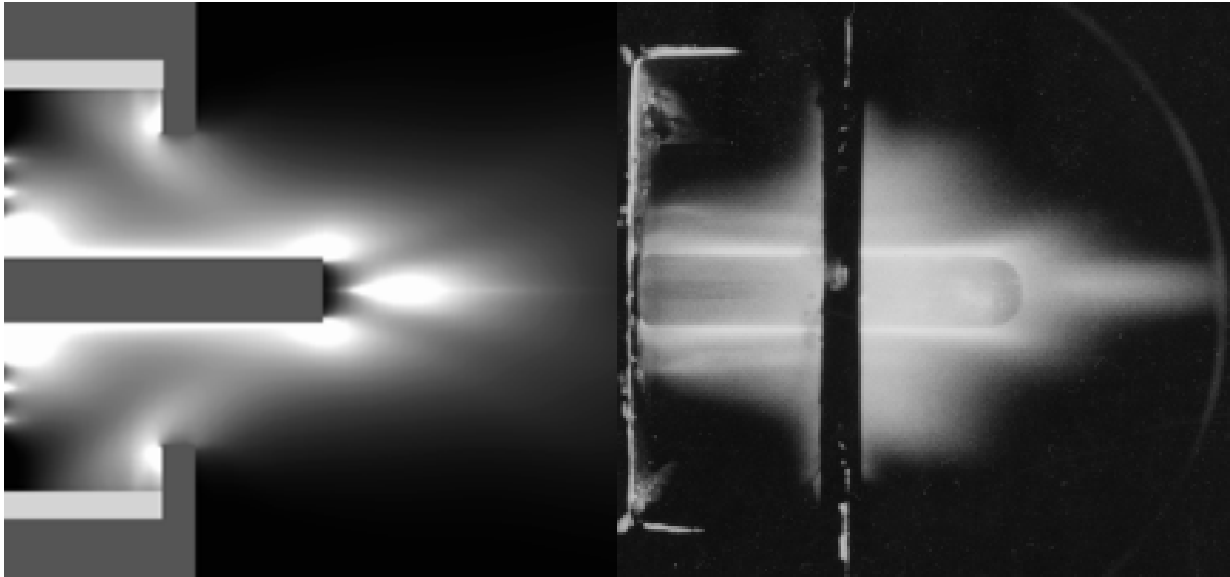
Figure 4.18: Left: Calculated electron number density (m^{-3}); Right: Photograph of light emission from FSBT discharge with transparent walls[136]. $J = 16.0$ kA, and $\dot{m} = 6.0$ g/s in both plots.

Current on the Cathode

The current distribution on the cathode is shown in Fig.4.19. Near the inlet, the surface current density has a value of $\simeq 550$A/cm^2, and quickly decreases to $\simeq 200$A/cm^2 along most of the cathode, only to rise again near its tip. This is compared with the measurements by Boyle[14] who measured similar values along the cathode, in Fig.4.19. However, while Ref.[14] reports that the current density at the cathode tip is in excess of 1000A/cm^2, the simulation only predicts

$\simeq 550\text{A/cm}^2$. This difference could be because the cathode in Ref.[14] was shorter than that of the FSBT, and had a conical tip, as opposed to the hemispherical tip of the FSBT. As seen in Fig.4.19, the longer cathode (simulation) has a greater surface area, and hence lesser current density. This may play a role in reducing erosion, as well as in decreasing Ohmic dissipation (to be discussed below).
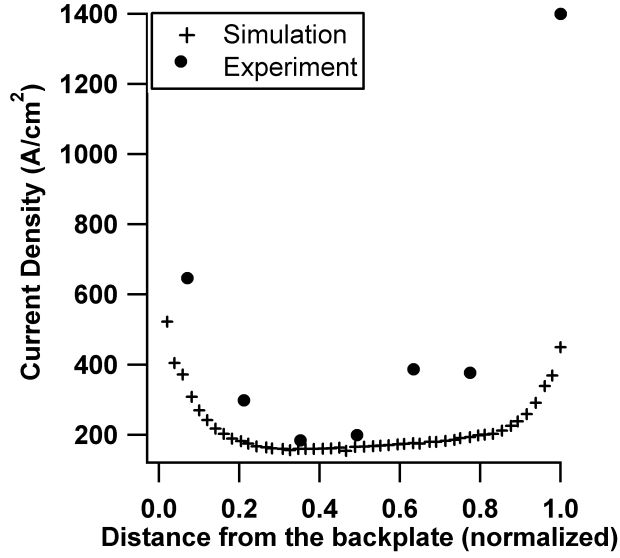
Figure 4.19: Surface current density on the cathode. Error bars on the measurement are not available in the original source[14].

Thrust Composition

The electromagnetic contribution to the thrust, T_{EM}, is

$$T_{EM} = \int (\mathbf{j} \times \mathbf{B}) dV. \tag{4.16}$$

The fractional contribution of the electromagnetic thrust to the total thrust is presented in Table 4.1. The other component, namely the electrothermal, is substantial when $\xi < 1.0$ (for instance, at $\xi = 0.82$, 40% of thrust is electrothermal). But the importance of electrothermal thrust decreases,

and the importance of electromagnetic thrust increases, with increasing current. From Table 4.1, it is clear that at $\xi \geq 1.0$ (which for argon is J = 16.0 kA for 6.0 g/s), the FSBT is predominantly an electromagnetic accelerator.

Energy Deposition

The total power deposited into the MPDT plasma can be split into kinetic power and dissipation,

$$\int \mathbf{j} \cdot \mathbf{E} dV = \int (\mathbf{j} \times \mathbf{B}) \cdot \mathbf{u} dV + \int \eta j^2 dV. \tag{4.17}$$

The second term on the right hand side is often termed the "dissipation integral"[18], and understanding and quantifying it is essential to improving the efficiency of the MPDT. All the three terms in eqn.(4.17) have been calculated for the FSBT, and the results are shown in Fig.4.20. Recall that these calculations do not include the power dissipated in the electrode fall, which can be a significant loss mechanism.

In a coaxial configuration, the current density is inversely proportional to the radius, and therefore the power deposition and the dissipation are large near the cathode. This is evident in Fig.4.20, where almost 45% of the dissipation occurs in the "inner flow" region[14] which is restricted to 1 cm around the cathode. As with thrust production (cf. §4.2.4), this near cathode region is an important one in energetics as well. For consistency, one can verify that the sum of all the input power in all the zones in Fig.4.20 add up to VJ (571 kW) (see Table 4.1).

It is worth noting that the shell near the cathode is the only region where the kinetic power exceeds the Ohmic heating (which is largely unrecovered because of the lack of a nozzle or any other mechanism to convert it into thrust).
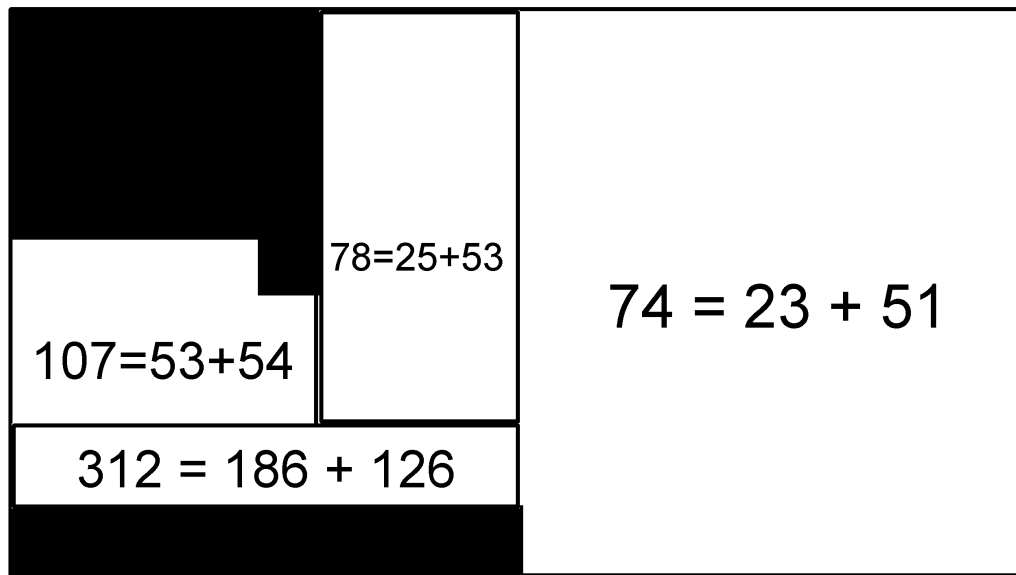
Figure 4.20: Power expenditure in various regions (kW). The values of each of the terms in eqn.(4.17) are shown in various regions.

4.2.5 Summary

While it was evident from §4.1 that this code produces a realistic description of the MPDT flow-field, this section strengthened the confidence in this code significantly. The calculated contours of density, ionization levels, velocity, mass flux patterns, enclosed current contours, cathode surface current density, and temperature all compared well with measurements at corresponding operating conditions. The calculated value of thrust matched with the measured value within 2% at the nominal operating condition.

Furthermore, the results of the code were able to provide insight into some physical mechanisms. Among the important observations are:

- Despite being a cause of stagnation in a part of the flow, the anode lip does not have a serious adverse effect on the thrust.

- The FSBT is predominantly an electromagnetic accelerator at its nominal operating condi-
  tion (J=16 kA, $\dot{m} = 6.0$ g/s of argon).

- The "inner flow" region 1 cm around the cathode plays an important role in the energetics.

Thus, the first two of the three goals set forth in the introduction (§1) have been accomplished. Now, armed with this code, it is appropriate to simulate the flowfield of the LiLFA and study its underlying processes.

Chapter 5

LiLFA SIMULATIONS

. . . I have promises to ̄keep,
And miles to go before I sleep,
And miles to go before I sleep.

Robert Frost
Stopping By Woods On A Snowy Evening

Now that the code, with its physical and numerical models, is known to reliably predict the flow-field of the MPDT that rely on self-field Lorentz forces, it can be used to study similar devices for which little experimental data exist.

5.1   Thruster Description

The lithium Lorentz force accelerator (LiLFA) is a plasma thruster[40, 37, 38, 39, 27] that uses the Lorentz force, produced by the interaction of current with self-induced magnetic fields, to accelerate lithium propellant (with barium additive), fed through multi-channel hollow cathodes, to high velocities ($10^4 - 10^5$ m/s) of interest to spacecraft propulsion. In particular, high-energy missions such as robotic and piloted exploration of the moon, mars and the outer planets, had been shown[137, 138, 6] to potentially benefit from the high specific impulse of the LiLFA and its

ability to efficiently process many hundreds of kilowatts of power from a nuclear power plant in a simple compact device (see §A for more information on this topic). Due to the LiLFA's promise, sustained efforts are being made in the US and Russia[40, 37, 38, 39, 27] to study it and improve its performance and lifetime.

While the work of Ageyev *et al.*[40] has demonstrated efficiency of 60% and I_{sp} of 4000 s, with 500 hours of erosion free operation at power levels up to 500 kW, there are no published records of systematic experimental or theoretical investigations of the underlying physical processes. Though the reported data (terminal characteristics (I_{sp}, and η) at the highest operating condition (J = 8.0 to 10.0 kA, $\dot{m}$ = 0.2 to 0.3 g/s)) are good for bolstering the technology readiness level of this device, lack of information on interior properties limits their utility for understanding plasma processes in the device. For this purpose, the code described earlier in this thesis was used to simulate the flowfield of the LiLFA. Since there are presently no experimental data for the LiLFA internal flowfields, the goal here is not comparison with experiments, but rather gain insight into some of the internal processes in the LiLFA. Moreover, the difficulty of obtaining measurements inside the thruster chamber, where the harsh environment of a high current (1-10 kA) discharge and condensing lithium render probing extremely difficult, further gives a motivation for relying on realistic numerical simulations to understand the internal processes.

5.2 Boundary Conditions

The computational domain used for the simulation is shown in Fig.(5.1). The dimensions were obtained from the NASA-JPL version of the LiLFA[139] (shown in Fig.(5.2)), which itself is based on the configuration of Ageyev *et al.*[40]. We will now discuss the evaluation of fluxes at surfaces #1 to 8 in Fig.(5.1).
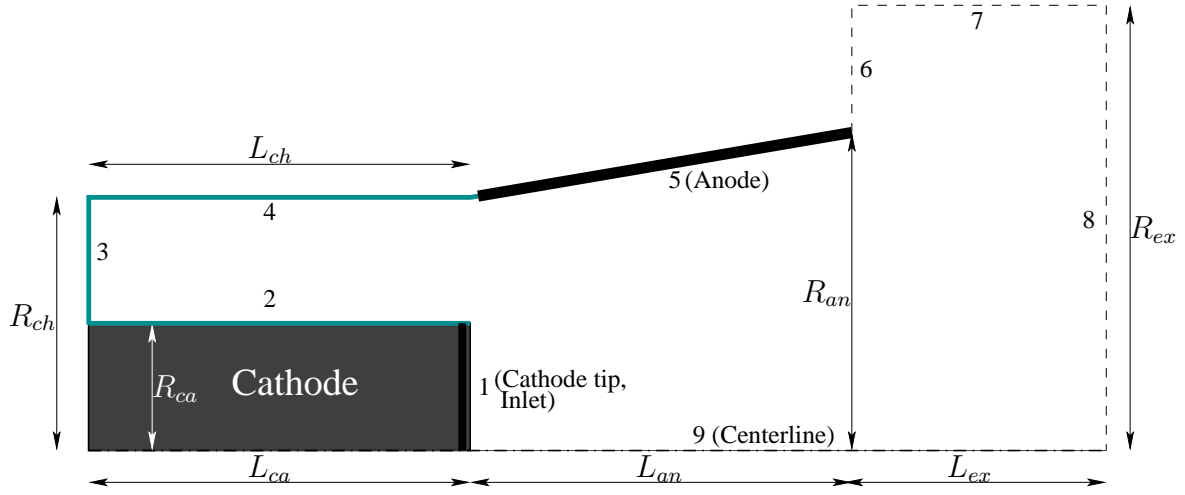
Figure 5.1: Computational domain of the Lithium Lorentz Force Accelerator (LiLFA), where $R_{ca}=$ 5.0 cm, $R_{ch}=$ 11.0 cm, $R_{an}=$ 13.4 cm, $R_{ex}=$ 20.0 cm, $L_{ca}=$ 26.0 cm, $L_{ch}=$ 26.0 cm, $L_{an}=$ 26.5 cm, and $L_{ex}=$ 22.5 cm.
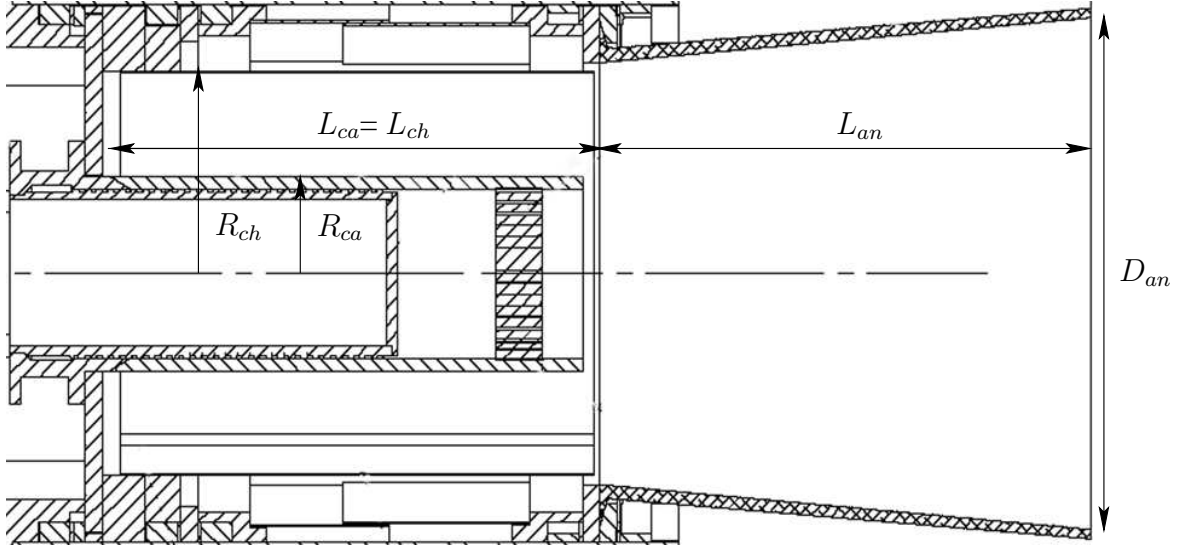
Figure 5.2: Scaled engineering drawing of the Lithium Lorentz Force Accelerator (LiLFA) (from ref.[139]), where $R_{ca}=$ 5.0 cm, $R_{ch}=$ 11.0 cm, $D_{an}=$ 27.0 cm, $L_{ca}=$ 26.0 cm, $L_{ch}=$ 26.0 cm, and $L_{an}=$ 26.5 cm.

115

5.2.1 Flow Properties

Inlet

Unlike gas-fed MPDTs, the propellant enters the LiLFA not through the backplate (surface #3) but through the cathode exit (surface #1 in Fig.(5.1)). The LiLFA uses a multi-channel hollow cathode[140, 141, 37, 40, 39, 142] inside which a stream of neutral lithium vapor is ionized efficiently, and ejected uniformly into the thruster through the cathode exit. Describing the operation of the hollow cathode[143] itself is beyond the scope of this work, which concerns only with what happens to the plasma once it enters the thrust chamber. Therefore, in this code, a specified mass flow rate (typically 0.25 g/s) of the ionized lithium plasma ($Z = 1$) enters at a specified temperature ($T_e = T_h = 0.75$ eV) through surface # 1.

Solid Boundaries

A standard solid-body boundary condition, $\mathbf{n} \cdot \mathbf{u} = 0$, is applied at the cathode outer surface (#2), backplate (#3), chamber inner surface (#4), and the anode nozzle (#5). Note that at the anode, $\mathbf{n}$ and $\mathbf{u}$ have both radial and axial components.

Anode Exit Freestream

After the plasma exits the thruster, it expands downstream as a plume because the exit pressure is greater than the ambient pressure. At the anode exit plane, the plume could expand upstream (through surface #6 in Fig.(5.1)). The flow through this plane could be either subsonic or supersonic. If the flow is subsonic, one needs to specify pressure, density, or temperature outside of the domain. In this code, an outside temperature of $T_{out} = 300$ K is specified. If the flow through surface #6 is supersonic, information out of the domain cannot affect the solution inside the domain. In that case, normal gradients of all relevant quantities are set to zero.

Freestream

At the other freestream boundaries, #7 and #8 in Fig.(5.1), all normal gradients of the flow proper-

ties are set to zero.

Centerline

At the axis of symmetry, all convective fluxes and radial gradients are set to zero.

5.2.2 Field Properties

The magnetic field is computed from Faraday's law, which through Stokes theorem can be written

as,

$$\int_A \frac{\partial \mathbf{B}}{\partial t} \cdot d\mathbf{A} = - \oint_C \mathbf{E} \cdot d\mathbf{l} \,. \tag{5.1}$$

In the cell-centered scheme used in this work, eqn.(5.1) implies that the evolution of the magnetic

flux is specified by the contour integral of the electric field around a cell. Therefore, the only

information required is the electric field along the boundaries.

Inlet

As described earlier, all the propellant enters the thruster through the cathode exit (surface #1

in Fig.(5.1)). Consequently, all the current attaches there. Faraday's law requires estimation of

electric field at this boundary to compute the evolution of magnetic field in the plasma adjacent to

this boundary. This can be estimated as,

$$E_r|_{z_{ca}} = E_r|_{z_{ca}+\Delta z} + \Delta z \left(\frac{\mu_o}{2\pi r} \frac{dJ}{dt} - \left(\frac{E_z|_{r+\Delta r} - E_z|_r}{\Delta r} \right) \right), \tag{5.2}$$

where $E_r|_{z_{ca}+\Delta z}$, $E_z|_{r+\Delta r}$ and $E_z|_r$ are computed self consistently in the plasma adjacent to this

boundary.

117

Cathode Outer Surface

In reality, the outer surface of the cathode (surface #2 in Fig.(5.1)) is made of a refractory metal (typically tungsten). But because there is little or no propellant upstream of the cathode exit, there is no current attachment on the outer surface of the cathode. So, in this code, this surface is modeled as an insulator to prevent current attachment in the near-vacuum region. Estimation of electric field at an insulating boundary is described in the following part.

Chamber Inner Surface

The thruster designs in ref.[40] and in Fig.(5.2) have a shield in the inner surface of the chamber (surface #4 in Fig.(5.1)), and there is no current attachment on it. So, as at the cathode outer surface, there is a need to evaluate the electric field at an insulating surface. Since all the current is downstream of these insulators, the electric field is

$$E_z(R_{ch}, z) = E_z(R_{ch} - \Delta r, z) + \Delta r \left(\frac{1}{r} \frac{\partial \psi}{\partial t} + \frac{\partial E_r}{\partial z} \right). \tag{5.3}$$

Anode Nozzle

Due to the no mass flux condition, the electric field at the anode is entirely resistive, and is given by,

$$\mathbf{E}_w = \eta_w \mathbf{j}_w . \tag{5.4}$$

The surface current, $\mathbf{j}_w$, is computed from Ampère's law in the usual manner.

Freestream

The freestream region was chosen far enough down stream (22.5 cm) of the thruster exit that all the current was enclosed within the domain. Thus, from Ampère's law, the magnetic field at the free stream boundaries is zero.

Centerline

Due to symmetry, the inductive component of the electric field is zero, because there is no flow across it. However, the resistive component is finite. This can be obtained from the value of the magnetic field at a point close to $r = 0$, through a simple Taylor series expansion [144],

$$E_z|_{r=0} = E_z'|_{r=0} = \eta j_z|_{r=0} = \eta \frac{4 \, B_\theta|_{\Delta r/2}}{\mu_o \Delta r} \ . \tag{5.5}$$

With the abovementioned boundary conditions, all the pieces are in place for the simulation of the flowfield in the LiLFA.

We will simulate three cases that correspond to operation at nominal condition ($\xi = 1$, J = 4.5 kA, $\dot{m} = 0.25$ g/s), above that condition ($\xi = 1.34$, J = 6.0 kA, $\dot{m} = 0.25$ g/s) and below it ($\xi = 0.67$, J = 3.0 kA, $\dot{m} = 0.25$ g/s).

5.2.3 Electron Density

The electron number density contours within the thruster are shown in Fig.(5.7-I) for three current levels. In all cases, it can be seen that the highest density is at the inlet, as expected. The notable decrease of n_e at the anode, with increasing ξ, is discussed in §5.3. As ξ increases, the plasma column in front of the inlet becomes more pronounced. This, in conjunction with the depletion of propellant near the anode, points to the increasing effect of the electromagnetic pinch with increasing current. The density in the column in front of the inlet varies from $3.5 \times 10^{20} \mathrm{m}^{-3}$ at the inlet, to $5.0 \times 10^{19} \mathrm{m}^{-3}$ at 15 cm downstream of the inlet, for the J = 4.5 kA (ξ=1.0) case. Radially, there is a sharp drop in density, since the expanding plasma is constricted by the pinch. At the cathode plane, the density drops sharply from $2.0 \times 10^{20} \mathrm{m}^{-3}$ at $r = R_{ca}$ to $1.0 \times 10^{19} \mathrm{m}^{-3}$ just 3 cm away. It is apparent that the pinch affects both the radial and the axial density distribution in the thruster.

There is also an indication in the $\xi = 0.67$ case that there is a weak shock present in the nozzle
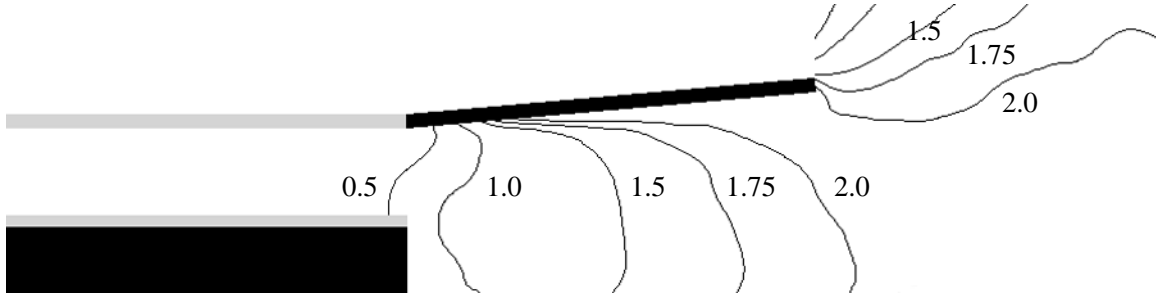
Figure 5.3: Calculated Mach number contours for $\xi = 1.0$ (J = 4.5 kA and $\dot{m} = 0.25$ g/s).

near the exit. This is seen more clearly in the velocity plots shown in Fig.(5.7-II).

5.2.4 Velocity

The contours of axial velocity are shown in Fig.(5.7-II), and the contours of Mach number for the ξ = 1.0 case are shown in Fig.(5.3). At the exit plane, velocity ranges from 16.0 to 24.0 km/s for the $\xi = 1.0$ case. The fact that the calculated value of thrust for this case is within 2% of the prediction of analytical models (see Fig.(5.8)) gives more credibility to the simulated values.

It is evident from the velocity plot of the $\xi = 0.67$ case (Fig.(5.7-II-a)) that there is a weak shock, denoted by the dotted line, which decelerates the flow in the thruster. This adverse effect only occurs for the sub-nominal condition $\xi = 0.67$. For $\xi \geq 1$, Figs.(5.7-II-b,c) show no such deceleration of the flow.

5.2.5 Current and Potential

The calculated contours of enclosed current are shown in Fig.(5.4) for three different current levels. It is evident that with increasing ξ the current lines get increasing blown downstream, as has been observed in numerous MPDT experiments[14, 18, 23]. This is to be expected because as the current increases the magnetic Reynolds number grows, leading to increased downstream convection of the magnetic field.
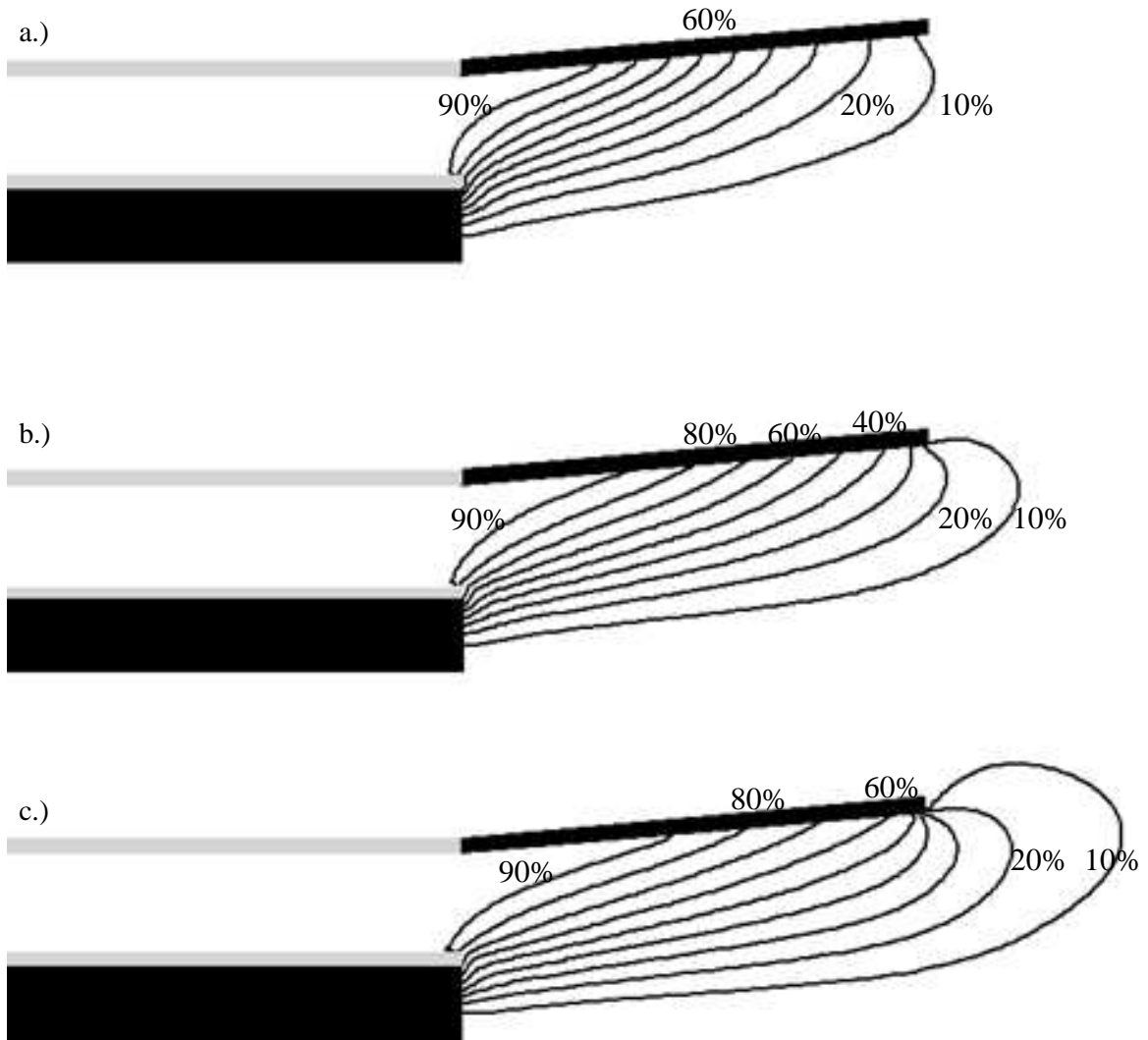
Figure 5.4: Calculated enclosed current contours (% of total) for, a.) $\xi = 0.67$, b.) $\xi = 1.0$, and c.) $\xi = 1.34$.

The calculated values of the potential are shown in Fig.(5.5) for three values of ξ. For the nominal operating condition ($\xi = 1.0$, J = 4.5 kA, $\dot{m} = 0.25$ g/s), this simulation predicts a plasma voltage drop of 17.4 V. It is important to note that our MHD model does not include the non-quasineutral electrode sheaths, and therefore the calculated voltage corresponds to the drop across the quasineutral plasma only. Anode fall could be a significant energy sink in the MPDT, where they have been quantified experimentally. However, they have never been studied directly in the LiLFA variant. Tikhonov *et al.*[145] estimate the anode fall to be 8 V and the cathode fall to be 3 V over a wide range of operating conditions for a similar thruster, and compare these numbers to experiments. Thus, adding these estimates of electrode falls (8 + 3 = 11 V) to our calculated value of plasma drop (17.4 V at $\xi = 1.0$) results in a total voltage drop of 28.4 V. This compares favorably to the measured value of 25 V at $\xi = 1.0$. It is useful to note that the monotonic increase of voltage with current predicted by the code is consistent with measurements[40].

5.2.6 Electron Temperature

The calculated values of electron temperature are shown in Fig.(5.6) for three current levels. For the $\xi = 1.0$ case, in the bulk of the chamber, T_e ranges from 2.0 to 3.5 eV. For the $\xi=1.34$ case, the electron temperature reaches 7 eV. This is significantly higher than the corresponding temperature of the argon plasma in the FSBT[146]. This can be explained by the differences in the electronic structure between argon and lithium. Argon has many electronic energy levels available to absorb energy without increasing the temperature much - a fact reflected in the low value of the ratio of specific heats ($\gamma \simeq 1.15$). However, lithium does not have sufficient electronic energy levels available to absorb energy at these temperatures. Consequently, its ratio of specific heats ($\gamma \simeq 1.6$) is very close to the ideal value (5/3) at these temperatures.

It is evident from Fig.(5.6) that, with increasing ξ, the region of highest temperature moves upstream towards the cathode exit plane ($R_{ca} < r < R_{an}$ at $L = L_{ca}$). This is the result of high

122
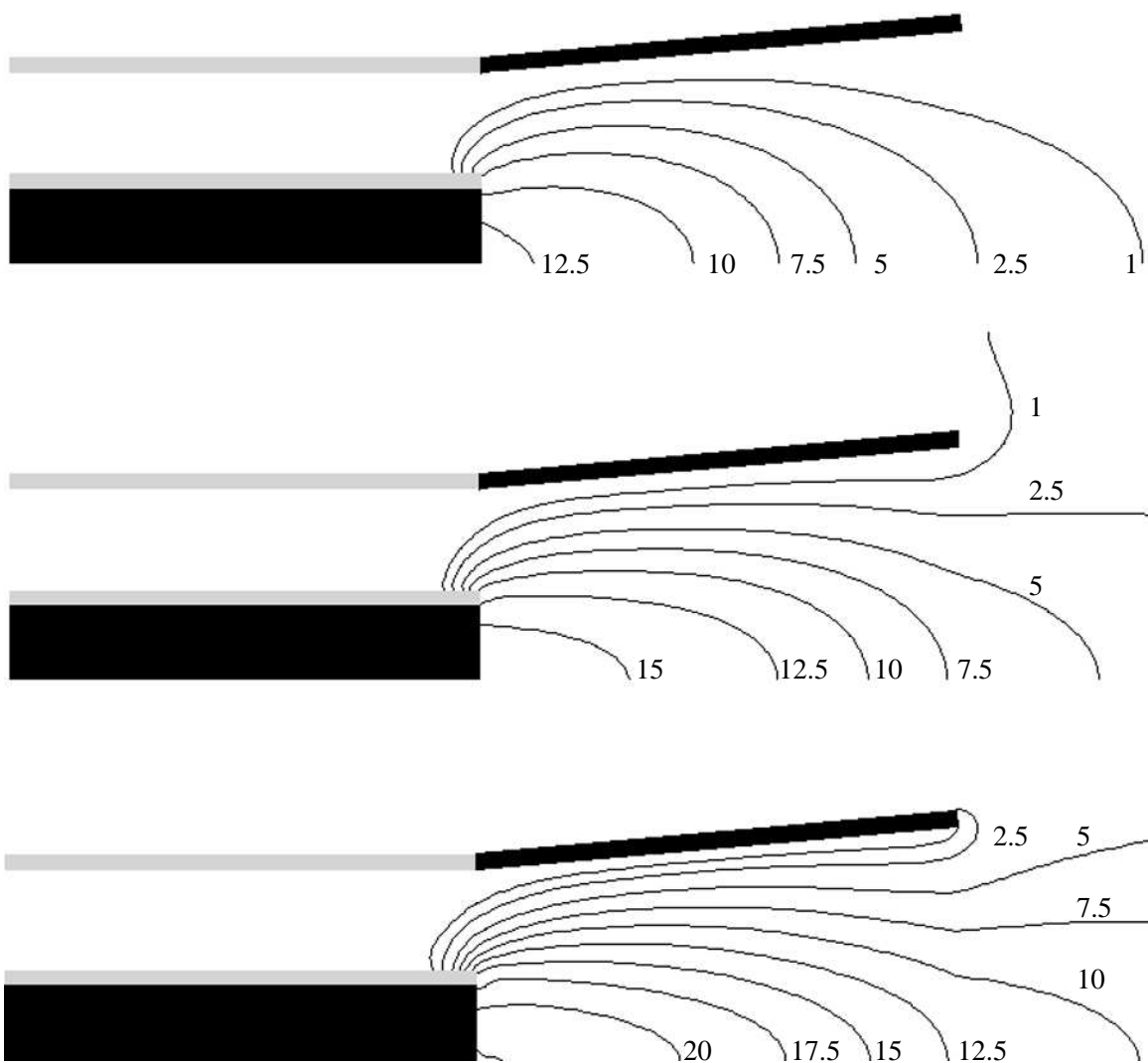
Figure 5.5: Calculated potential contours (V) for, a.) $\xi = 0.67$, b.) $\xi = 1.0$, and c.) $\xi = 1.34$.
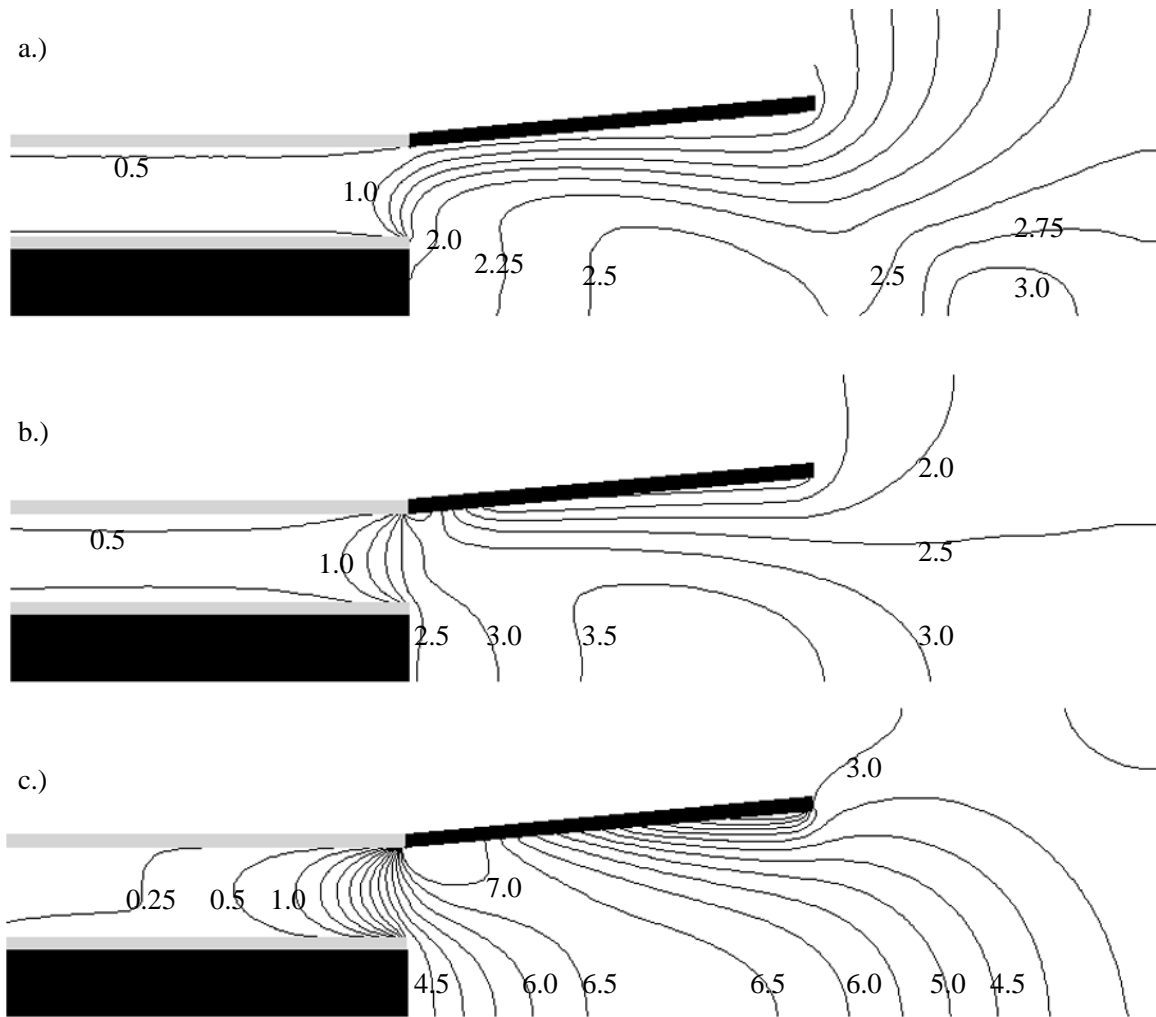
Figure 5.6: Calculated electron temperature contours (eV) for, a.) $\xi = 0.67$, b.) $\xi = 1.0$, and c.) $\xi = 1.34$.

anomalous collision frequency and heating in this region, and will be discussed in the next section.

As seen in Fig.(5.7-I), there exists a low density plasma ($n_e \sim 10^{19}/\text{m}^3$) in the non-divergent part of the channel. Since there is no current attachment and Ohmic heating, the temperature is low (≤ 0.5 eV) here. The simulation shows that the upstream flux of plasma into this region decreases with increasing ξ, and consequently the density and the temperature also decrease.

5.2.7 Anomalous Transport

Enhanced energy dissipation in plasma thrusters, due to exchange of momentum between particles and waves induced by microinstabilities, has been documented[96, 97] in gas-fed MPDTs with argon as propellant[146]. However, this effect has never been investigated in lithium plasma thrusters.

The ratio of anomalous resistivity to classical resistivity in the LiLFA is shown in Fig.(5.7-III). For the $\xi = 0.67$ case (Fig.(5.7-III-a)), the overall effect of anomalous transport is limited because operation at this condition is below the threshold for predominantly electromagnetic acceleration. For the higher ξ cases (Fig.(5.7-III-b,c)), anomalous resistivity exceeds classical resistivity at the cathode exit region and throughout the rear of the anode. This is to be expected because that is the region of highest magnetic field (Fig.(5.4)) and low density (Fig.(5.7-I)), and therefore the region of high Hall parameters that mark the escalation of anomalous transport. In the upstream and downstream regions of the anode, anomalous transport is negligible because the $u_{de}/v_{ti} \geq 1.5$ threshold is not satisfied due to lack of sufficient current[96, 97].

As discussed earlier, the highest values of anomalous resistivity occur at the cathode exit plane, and this leads to the high temperatures observed in this region seen in Fig.(5.6-c).
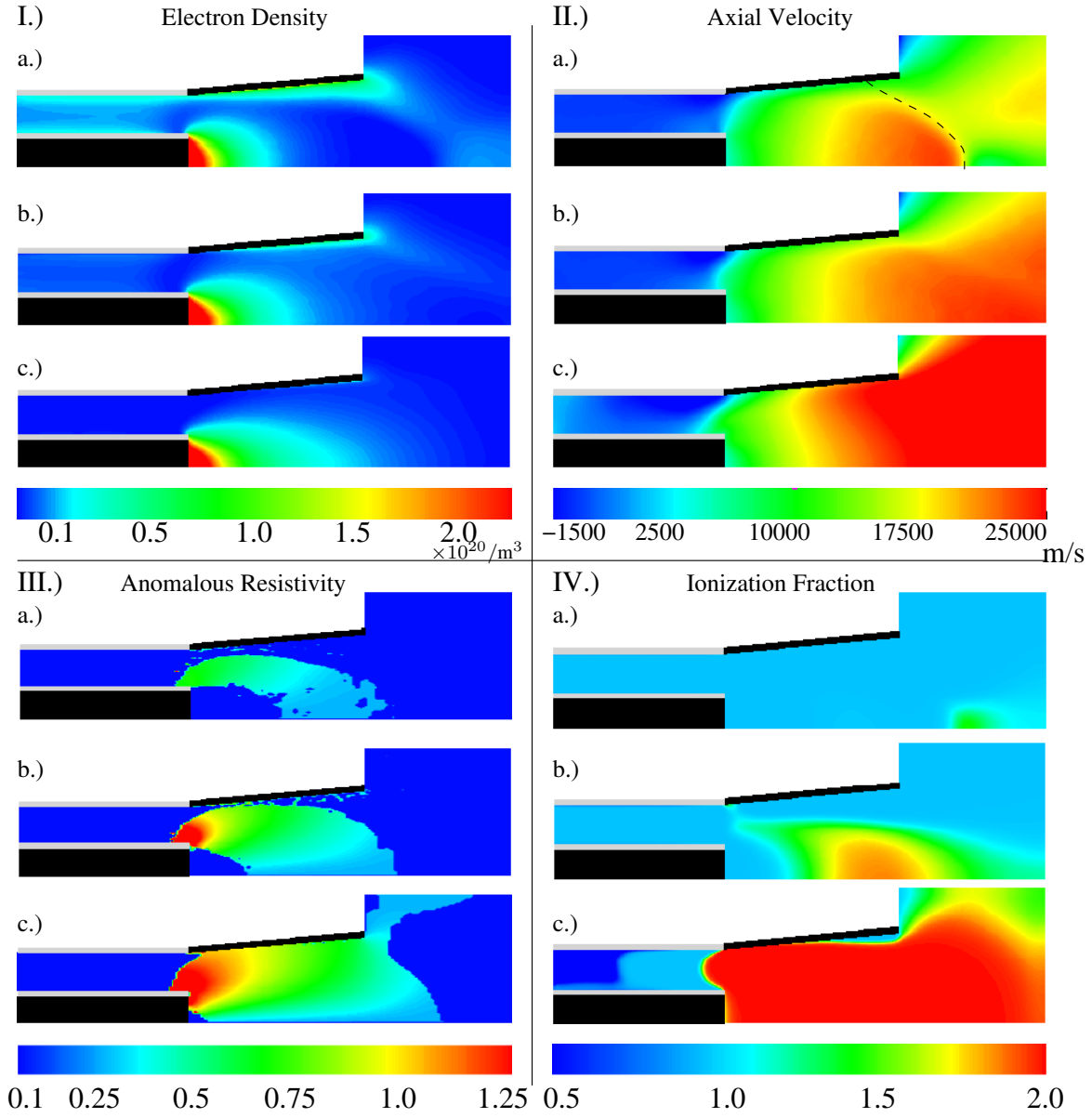
Figure 5.7: Panel I shows the calculated values of electron number density (m^{-3}). Panel II shows the calculated values of axial velocity (m/s), and the dotted line in II-a indicates a weak shock. Panel III shows the calculated ratio of anomalous to classical resistivity. Panel IV shows the calculated effective ionization fraction. In each panel, the calculated values are shown for three different values of current: a.) $\xi = 0.67$, J = 3.0 kA, b.) $\xi = 1.0$, J = 4.5 kA, and c.) $\xi = 1.34$, J = 6.0 kA. The mass flow rate $\dot{m} = 0.25$ g/s in all cases.

5.2.8 Ionization

The effective ionization fraction is shown in Fig.(5.7-IV). It is important to bear in mind that this simulation uses an equilibrium ionization model, and hence $Z = Z(n, T_e)$ (see Fig.(2.10)), and therefore an understanding of T_e distribution (shown in Fig.(5.6)) is important to understanding the distribution of ionization levels.

Two features stand out when observing these plots: i) there is significant amount of second ionization when $\xi \geq 1$, and ii) there is a rapid change in ionization structure after ξ exceeds 1.

First, though the second ionization level of lithium is very high (75.6 eV), the equilibrium ionization model predicts doubly ionized lithium at temperatures above 5 eV. This is because the high-energy electrons at the tail, and not the bulk electrons, of the Maxwellian distribution are responsible for ionization. It is also important to note that the ionization of lithium at this temperature ($Z = 2.0$) is much less than the corresponding ionization level of argon ($Z \simeq 5.0$). For the $\xi = 1.0$ case, the correspondence between Fig.(5.7-IV-b) and Fig.(5.6-b) is clearly seen.

Second, a notable difference in ionization structure is seen between the $\xi = 1.0$ case and the $\xi = 1.34$ case. As we mentioned earlier, the upstream plasma flux into the non-divergent part of the channel surrounding the cathode decreases with increasing ξ, consequently decreasing the temperature levels there (see the region upstream of the anode in Fig.(5.7-I) and Fig.(5.6) for increasing current levels). The equilibrium ionization model shown in Fig.(2.10) indicates that the ionization level changes rapidly with temperature (high $\partial Z / \partial T_e$) at $T_e \simeq 4$ eV. The 4 eV threshold is crossed in going from the $\xi = 1.0$ case to the $\xi = 1.34$ case.

5.3 Insight into Physical Processes

Having described the main features of the simulation results, we now turn our attention to extracting physical insight into the underlying physical mechanisms in the LiLFA. Unless explicitly stated

otherwise, the focus will be on the operation at J = 4.5 kA (at $\dot{m} = 0.25$ g/s), since this corresponds to the nominal operating condition of $\xi = 1$.

5.3.1 Thrust Composition

The numerical simulation allows unique insight into the breakdown of thrust, and the scaling of its various components. The calculated values of thrust from the simulation are compared to predictions by the analytical models of Tikhonov *et al.*[145, 77], and the results are presented in Fig.(5.8) (the Tikhonov scaling law relies on an estimate of upstream value of the speed of sound, a_o, which is usually evaluated at a temperature between 1 eV to 2 eV).

Over a range of conditions, with $36.0 \leq J^2/\dot{m} \leq 144.0$ kA$^2/g/s$ $(0.67 \leq \xi \leq 1.34)$, the code's predicted thrust agrees well with the analytical model. At $\xi \geq 1$, the agreement is within 2%. Below the nominal operating current, at $\xi = 0.67$, the code under predicts thrust by 5%, which is likely due to the existence of a velocity-reducing shock in the simulation (see Fig.(5.7-II-a)) that is not accounted in the analytical model.

The thrust produced by the LiLFA can be broken down into three components,

$$T = \int_{in} \rho u_z \left(\mathbf{u} \cdot d\mathbf{A} \right) + \int_V \mathbf{j} \times \mathbf{B} \, dV + \int_A p \left(\hat{z} \cdot d\mathbf{A} \right). \tag{5.6}$$

The first term is the thrust produced by the jet of plasma entering the thruster from the multi-channel hollow cathode. In our simulation, the entire mass flow rate of the propellant ($\dot{m} = 0.25$ g/s in this simulation) enters uniformly at the sonic condition, with $T_e = T_h = 0.75$ eV, and therefore the first term in eqn.(5.6) accounts for 1.37 N of thrust for all current levels.

The second term, the volume integral of the Lorentz body force, can be treated as the surface integral of the magnetic stress tensor[2, 76],

$$\int_V \mathbf{j} \times \mathbf{B} \, dV = \int_V \nabla \cdot \bar{\bar{\mathcal{B}}}_M \, dV = \int_S \bar{\bar{\mathcal{B}}}_M \cdot d\mathbf{S}. \tag{5.7}$$

128

a.)   b.)   c.)

Total thrust (simulation) = 3.1 N   Total thrust (simulation) = 4.4 N   Total thrust (simulation) = 5.9 N
Total thrust (theory)   = 3.2 N   Total thrust (theory)   = 4.3 N   Total thrust (theory)   = 5.8 N
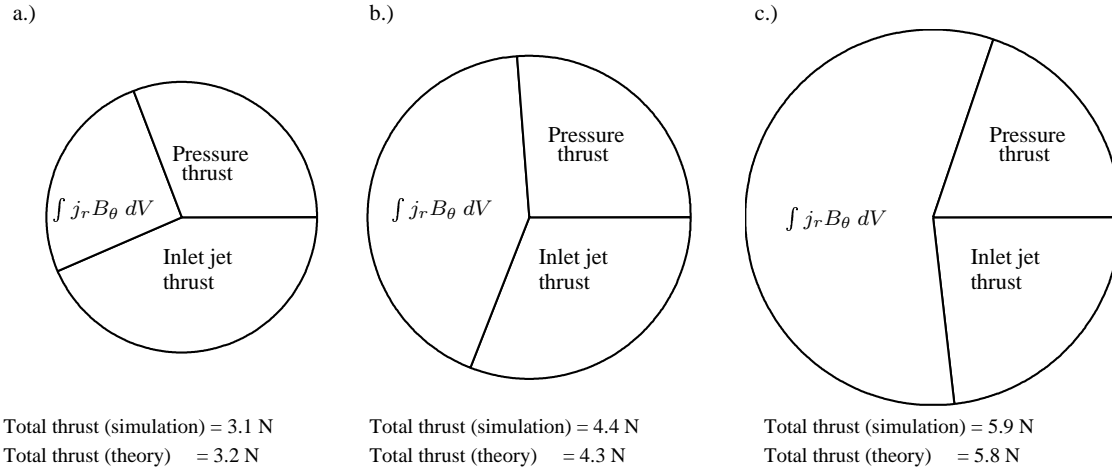
Figure 5.8: Thrust components and the total thrust from the simulation are compared to the analytical value of total thrust, for a.) $\xi = 0.67$, b.) $\xi = 1.0$, and c.) $\xi = 1.34$. The part labeled $\int j_r B_\theta \, dV$ is the so-called "blowing" contribution. The relative size of each pie is in direct proportion to its total thrust.

Because we are interested in the axial component of force (commonly referred to as "blowing"[2]), this term has to be integrated over the inlet surface and the backplate between the cathode and the anode. The blowing contribution from the inlet surface increases from 6% at $\xi = 0.67$ to 14% at $\xi = 1.34$, while that from the backplate increases from 20% at $\xi = 0.67$ to 43% at $\xi = 1.34$. This scaling, as well as that of other components, is represented in the pie charts of Fig.(5.8).

The third term represents the thrust produced by gasdynamic pressure acting on the surfaces of the thruster. The radial component of the Lorentz body force contributes to thrust through unbalanced pressure distribution of the pinched gas on the surrounding surfaces. As before, this has to be integrated over the inlet surface and the backplate between the cathode and the anode. At the inlet surface, its relative contribution to total thrust decreases from 25% to 20%, though it increases in absolute magnitude. At the backplate, its relative contribution decreases from 5% at $\xi = 0.67$ to less that 0.1% at $\xi = 1.34$, and so does its absolute contribution. This is consistent

129

a.) b.) c.)

Enthalpy & Ionization

Undirected kin. power

Thrust power

Total power = 41.7 kW

Enthalpy & Ionization

Undirected kin. power

Electrode

Thrust power

Total power = 78.3 kW

Enthalpy & Ionization

Undirected kin. power

Electrode thermal conduction

Thrust power

Total power = 135.6 kW
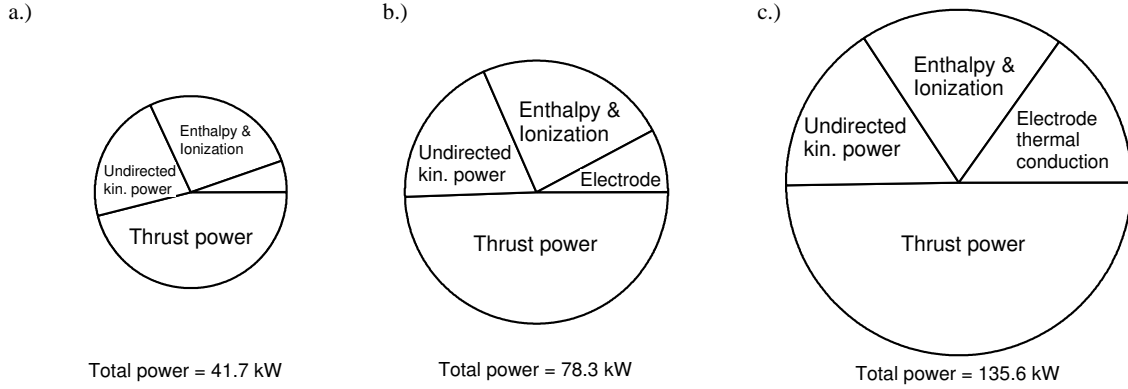
Figure 5.9: Calculated power deposition fractions at, a.) $\xi = 0.67$, b.) $\xi = 1.0$, and c.) $\xi = 1.34$, with the total input power for each case given below. Power expended in radiation is $< 0.1\%$ in all three cases. The relative size of each pie is in direct proportion to its total power.

with the decrease in plasma density with increasing ξ at the backplate (cf. Fig.(5.7-I)).

At $\xi = 1.0$, the fraction of the total thrust that is associated with electromagnetic blowing ($\int j_r B_\theta dV$) is 44%. This is noticeably smaller than the corresponding case for the Full-Scale Benchmark Thruster (FSBT), where that fraction is 75%[146], and conversely the electromagnetic pinching ($\int j_z B_\theta dV$) is less significant than in the LiLFA.

The effect of operation at $\xi \geq 1$ is a significant increase the importance of electromagnetic blowing, and a decrease in the importance of gasdynamic and pressure contributions to thrust.

5.3.2 Energy Deposition

The breakdown of various energy sinks, and their scaling with ξ, are shown in the pie charts of Fig.(5.9), where each pie chart shows the relative contribution of the thrust power (calculated as $T^2/2\dot{m}$), undirected kinetic power (calculated as $\int (\rho u^2) u_r dA$), enthalpy and ionization power (calculated as $\int \frac{p}{\gamma-1} \mathbf{u} \cdot \mathbf{dA}$), and electrode thermal conduction power (calculated as $\int k \nabla T_e \cdot \mathbf{dA}$). The power lost in heating, electronic excitation, and ionization of the propellant stream amounts to

27% of the total power for the $\xi = 0.67$ case, but reduces to 20% for the $\xi = 1.34$ case. Tikhonov *et al.*[145] suggest that this number drops to 12% at higher current levels. Some of this power could possibly be recovered as directed kinetic energy. It can be observed from Fig.(5.9) that some 20% of the power is carried away in the form of undirected kinetic energy over the range of ξ that was considered here. The simulation also indicates that the fractional power conducted to the electrodes increases from 5% at $\xi = 0.67$ to 15% at $\xi = 1.34$. This can be attributed to the increase in temperatures, especially near the anode, over that range of ξ (see Fig.(5.6)). The magnitude and scaling of the actual power lost to the electrodes could well be affected by the electrode sheaths that were not included in the simulation. The fraction of the total power expended in thrust increases from 45% at $\xi = 0.67$ to 51% at $\xi = 1.34$. Since our simulation does not include electrode drops, which could be a significant energy sink, that fraction is not the same as the thrust efficiency of the device.

The above observations, especially the pie charts in Fig.(5.9), lead us to the following qualitative conclusions: with increasing ξ, the input power becomes approximately equipartitioned between thrust power and losses, as shown in pie chart 'c' of Fig.(5.9). Furthermore, the lost power itself becomes approximately equipartitioned between the three loss mechanisms, which are undirected kinetic power, enthalpy and ionization, and electrode thermal conduction.

In order to visualize the spatial distribution of the useful power (work expended by the electromagnetic blowing force), we calculate

$$P_{blow} = j_r B_\theta u_z \ dV, \tag{5.8}$$

and show it in Fig.(5.10) at $\xi = 1.0$. The figure indicates that the outer edge of the cathode is the region in which most of the work done by the electromagnetic blowing force is expended. This can be explained as follows: the magnetic field, which drops as $1/r$ between $R_{ca} < r < R_{an}$, is maximum along the outer surface of the cathode. Since the current attaches only at the cathode tip (see Fig.(5.4)), the product of current and magnetic field is highest in this region.

131
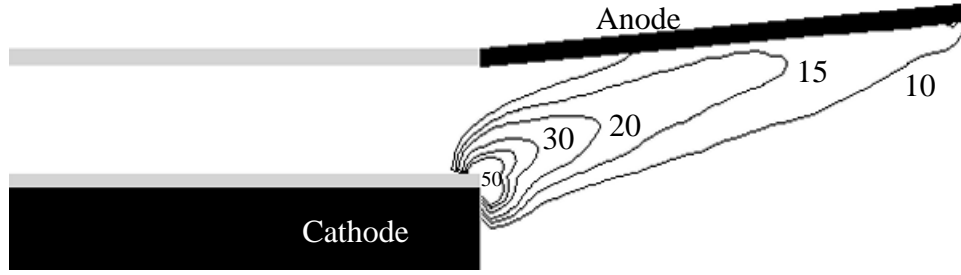
Figure 5.10: Contours of blowing power expenditure (in watts) at $\xi = 1.0$.

5.3.3   Anode Starvation and Current Conduction Crisis

Several experimental studies[16, 22, 19] of high-current plasma accelerators have confirmed the occurrence of performance-limiting oscillations that are onset above a particular value of current, called the "onset current" (J^*). Operation above this onset current results in notable increase in electrode ablation and a shift from a steady terminal voltage to one with high-frequency oscillations of substantial amplitude that can reach up to 100% of anode voltage. It is known[147, 148, 30, 149] that the onset phenomenon is related to the depletion of propellant near the anode. The results of our code can be used to shed some light on this phenomenon.

Theoretically, the ratio of gasdynamic to magnetic pressure, β, equals 1 at the boundary of a pinched plasma enclosing all the mass and all the current[74] (see Fig.(5.11)) ($\dot{m} = \rho = p = 0$ outside). At the inlet, the current is axial and the plasma is enclosed in a free-boundary cylinder, as in the case of a classical pinch, of radius R_{ca}, and expands further downstream. Korsun[150] and Tikhonov *et al.*[145] calculate the radius of the free boundary, $R(z)$, which encloses all the propellant mass using quasi-1D ideal MHD theory ($\beta = 1$ on this boundary). Above the onset current (J^*), the pinching force causes this free boundary to move away from the anode ($R(z) < R_{an}$), preventing current conduction to the anode. This is illustrated in Fig.(5.12). It is believed[148, 30, 149] that this anode-starvation crisis is resolved by the discharge through a transition from diffuse arc attachment at the anode to a mode in which the current attaches in spots. These spots are be-
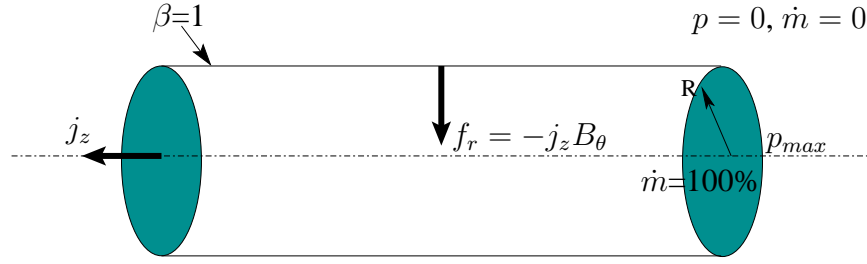
Figure 5.11: Schematic of plasma constrained by magnetic pressure.
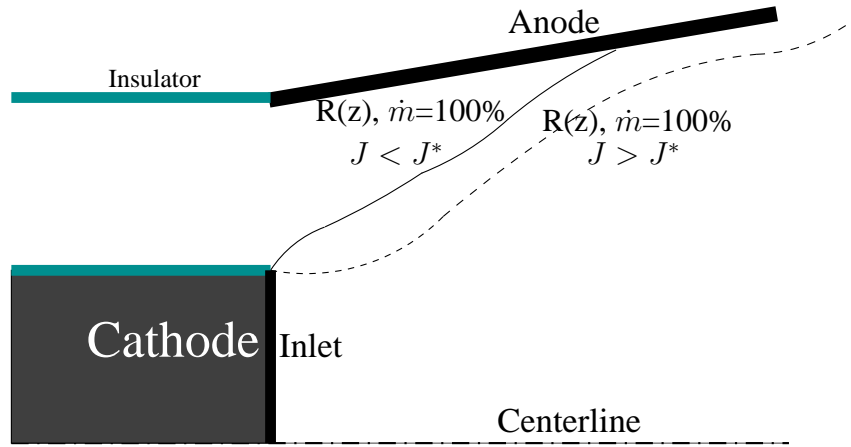
Figure 5.12: Schematic of the "free boundary" (which encloses all the mass), and its variation with discharge current.

lieved to supply, through material evaporation, the required mass for current conduction, and their high-frequency motion is reflected as high-amplitude oscillations in the terminal voltage.

We now present, for the first time, a quantitative illustration of the role the $\beta = 1$ line plays in the anode starvation mechanism that leads to onset. It is important to note that in a real plasma pinch with finite resistivity and transport, the $\beta = 1$ line may not contain 100% of the mass. Fig.(5.13) shows that in our simulation, the $\beta = 1$ line coincides to the line enclosing approximately 95% of the mass, over the investigated range of ξ. This is especially the case for the region immediately downstream of the cathode where the pinch is expected to occur. Therefore,
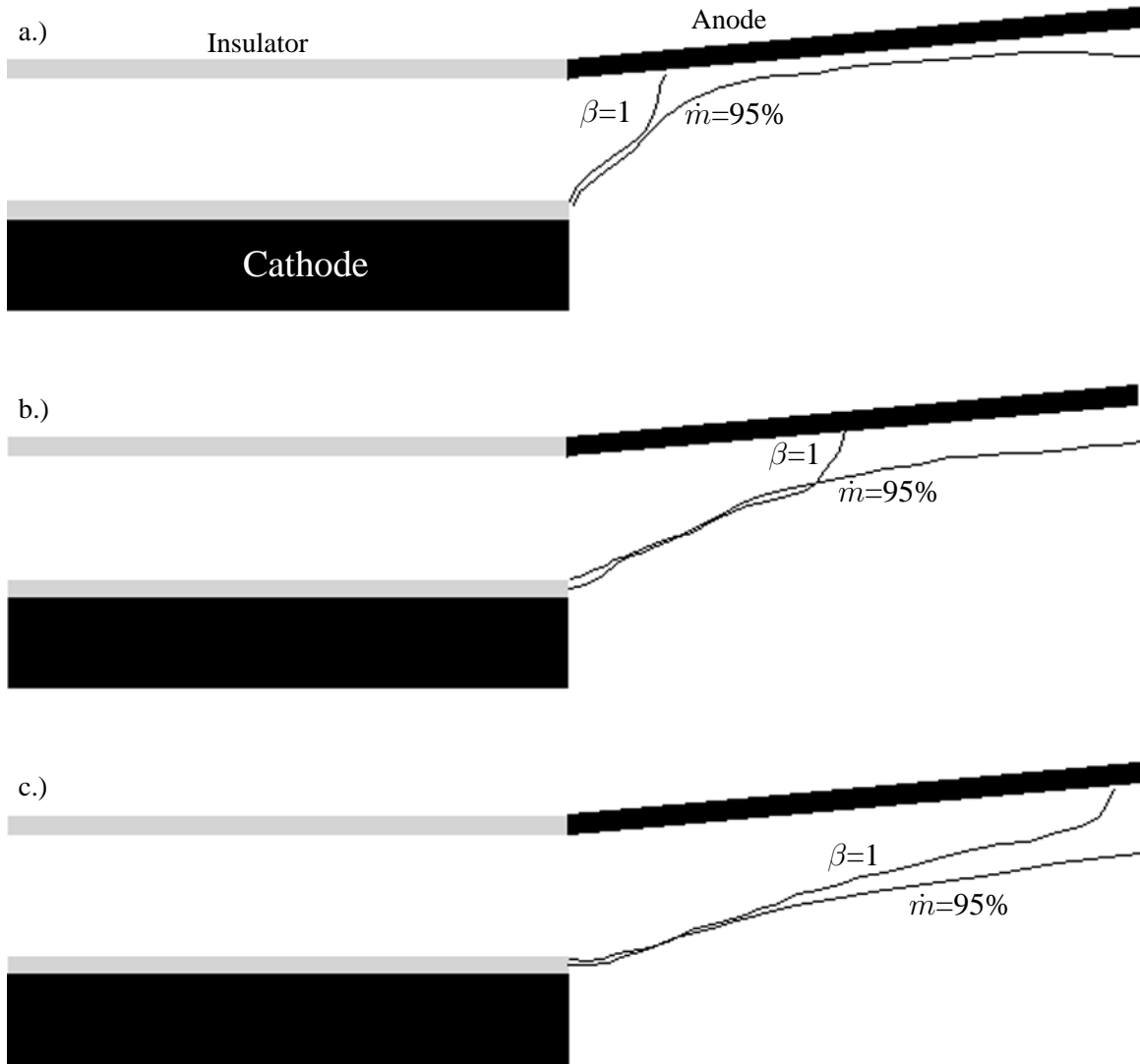
Figure 5.13: Relative location of the $\beta = 1$ line to the 95% enclosed mass flux line is shown for, a.) $\xi = 0.67$, b.) $\xi = 1.0$, and c.) $\xi = 1.34$.

Fig.(5.13) shows that with increasing ξ, the downstream end of the $\beta = 1$ line slides further downstream along the anode, thus leading eventually to an anode starvation crisis, as could be anticipated for operation at a value of $\xi > 1.34$ (see Fig.(5.13-c)). This is a clear illustration of the anode starvation mechanism and the role the $\beta = 1$ line plays in the onset phenomenon - a role that had been suspected through analytical theories of Korsun[150] and Tikhonov *et al.*[145]. Another interesting observation, obtained by comparing Fig.(5.13) and Fig.(5.4), is that only 70% of the current is enclosed by the $\beta = 1$ line, implying that some 30% of the current is conducted by only 5% of the propellant. This underscores the importance of anode starvation in the current conduction crisis reached at a high value of total current.

Fig.(5.14) further illustrates, more quantitatively, the relationship between the $\beta = 1$ line and anode starvation. The figure shows a plot of electron density profile along the anode at three values of ξ, with an asterisk on each curve denoting the location of the point where the $\beta = 1$ line intersects the anode. When that point meets the downstream end of the anode, as almost the case for the $\xi = 1.34$, the current conduction crisis is expected to occur. At that condition, Fig.(5.14) shows that the electron density has dropped a factor of five with respect to the maximum density for $\xi = 0.67$.

In the experiments by Ageyev *et al.*[40], the discharge voltage was observed to increase sharply above J = 6.5 kA at this mass flow rate. Our simulations show that at J = 6.0 kA, the $\beta=1$ line in the simulation extends to the downstream tip of the anode (see Fig.(5.13c)), indicating that the current will be prevented from attaching to the anode at a current not much higher than 6.0 kA. This has implications for thruster design. Since the $\beta=1$ line encompasses 95% of the propellant, it roughly delineates the free boundary of the plasma inside the LiLFA, and can be used to design an anode contour that delays onset for a given set of conditions. The design exercise, however, is beyond the scope of this paper.
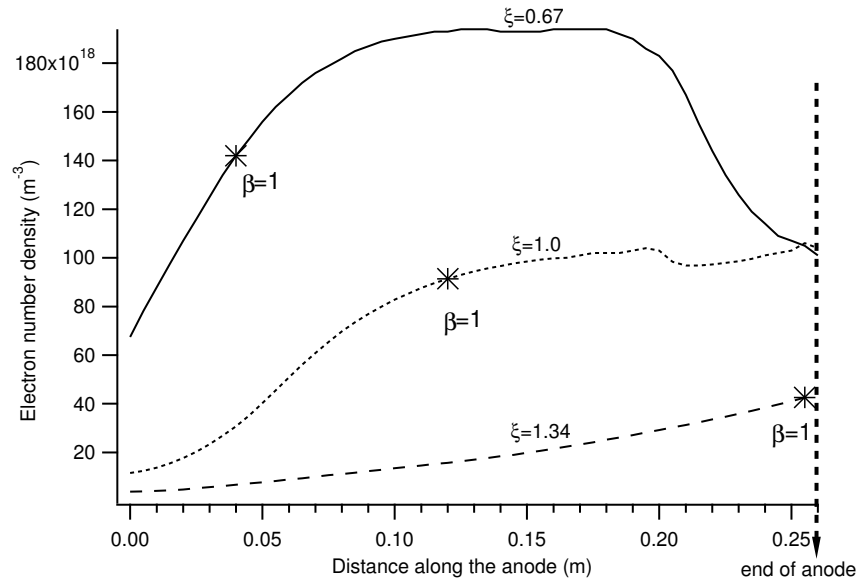
Figure 5.14: Plots of calculated electron number density (m^{-3}) at the anode indicate starvation of the anode with increasing current ($\dot{m} = 0.25$ g/s in all plots). The location of $\beta = 1$ is marked on these plots to show its relevance to this starvation.

5.4 Summary

A specialized axisymmetric plasma-fluid simulation code using the state of the art numerical techniques[132] was previously validated[146] using experimental data with an argon self-field MPDT, and used here to simulate flows in the lithium Lorentz force accelerator. The goals were: i) to provide detailed flowfields inside the thruster chamber, where internal probing is extremely difficult, and, ii) to provide insight into the nature and scaling of thrust composition, energy deposition, and the onset phenomenon. In particular, the following observations and conclusions can be drawn:

- The flowfields of density, velocity, ionization, and anomalous resistivity show distinct features that have strong qualitative dependence on the total current, as it is raised through the nominal condition ($0.67 \leq \xi \leq 1.34$). In particular, for operation at a sub-nominal condition ($\xi = 0.67$), there exists a shock in the thruster that decelerates the flow. However, this detrimental structure is not present at $\xi \geq 1$.

- For operation at and above the nominal condition ($\xi = 1$) the simulations show pinching of the plasma towards the centerline, an increase in the importance of anomalous resistivity, with an associated increase in electron temperature.

- The effect of operation at $\xi \geq 1$ is a significant increase the importance of electromagnetic blowing, and a decrease in the importance of gasdynamic and pressure contributions to thrust.

- With increasing ξ, the input power becomes approximately equipartitioned between thrust power and losses. Furthermore, the lost power itself becomes approximately equipartitioned between the three loss mechanisms, which are undirected kinetic power, enthalpy and ionization, and electrode thermal conduction.

- The $\beta = 1$ line was shown to approximately correspond to the free boundary of a classical pinch that gets exacerbated with increasing total current. The motion of this line with increasing ξ was shown to provide a clear illustration of the anode starvation mechanism that leads to the current conduction crisis called onset.

With this all the three goals set forth in the introduction (§1.1) have been accomplished. Nevertheless, there are many topics to be pursued. These will be discussed in the next chapter.

Chapter 6

CONCLUDING REMARKS

We shall not cease from exploration
And the end of all our exploring
Will be to arrive where we started
And know the place for the first time.

T. S. Eliot
Little Gidding

6.1   What are the contributions of this thesis?

One objective of this thesis was to develop a numerical simulation model that incorporates the state-of-the-art in numerical methods and physical models governing plasma flows, in order to study MPDTs and LiLFAs.

For this purpose, a new numerical scheme for the accurate computation of plasma flows of interest to propulsion was developed and validated against standard test problems. The scheme treats the flow and the field in a self-consistent manner, and conserves mass, momentum, magnetic flux and energy. The characteristics-splitting scheme, which was developed from concepts used for the solution of Euler equations, was used to solve the ideal MHD equations. The ability of this scheme to capture discontinuities monotonically was demonstrated. Flux-limited anti-diffusion

was used to improve spatial accuracy away from discontinuities.

On top on the ideal MHD model, relevant diffusive and dispersive effects, such as resistivity with Hall effect, and electron and ion thermal conduction were included. Furthermore, effects of thermal non-equilibrium between electrons and ions were incorporated. Anomalous transport effects, which account for momentum transfer between waves and particles in finite-β MPD flows, were included in the transport models. Real equation of state models, to account for energy deposition into internal modes, were developed for argon and lithium, and were found to have significant effects on producing realistic and stable solutions. Multi-stage equilibrium ionization models were used to obtain ionization levels and species densities for argon and lithium plasmas. With the inclusion of anomalous transport effects and real equation of state models, the complexity of the physical model in this code exceeds that of the most persistent efforts at other institutions to simulate MPDT flows. There is no documentation of any existing code that was validated against standard MHD test cases. Furthermore, unlike many other previous MPDT flow simulation codes, this one uses modern numerical methods for the solution of the governing equations.

These schemes were adapted to non-orthogonal mesh systems to allow for flexibility in modeling various geometries. The resulting code was then modified to run on parallel computing platforms, giving it the ability to tackle computationally challenging problems.

The primary objective of this thesis was to then use this code to obtain detailed flowfields for, and gain insight into the operation of real high-power plasma thrusters. For this purpose, this solver was then used to simulate the flowfields in a constant area coaxial MPDT, the full-scale benchmark thruster (FSBT) and the lithium Lorentz force accelerator (LiLFA), at various operating conditions, with $J^2/\dot{m}$ ranging from 24.0 kA^2/g/s to 66.7 kA^2/g/s for argon and 36.0 kA^2/g/s to 144.0 kA^2/g/s for lithium. The resulting profiles of densities, velocities, species temperatures, along with current and potential contours and were found to be realistic, when compared with existing data on MPDTs. The values of thrust predicted by the simulation were in excellent agreement

with measurements and analytical models.

Based on the confidence gained from realistic simulations that compared well with experimental data and photographic observations, these results were then used to analyze the underlying acceleration and dissipation mechanisms in the FSBT and the LiLFA. The composition of thrust was analyzed, insight into energy expenditure was gained, and the performance limiting current conduction crisis caused by anode starvation was investigated in both the FSBT and the LiLFA.

With that, the goals stated in the introduction have been attained.

Nevertheless, there remains plenty of room for improvement in physical modeling and numerical capabilities, as well as phenomena to explore. These are outlined in the subsequent section.

6.2   What remains to be done?

6.2.1   Computational Methods

In order improve the utility of this code for practical applications, some improvements can be made to the computational methods described in this these.

Presently, due to the overhead cost associated with parallel computing, the CPU utilization efficiency is only about 70%. With increasing number of processors, this efficiency drops to about 50%, as shown in Fig.(3.11). Though it is possible to get this number closer to 100%, it is not clear if it is worth the effort. This could be a topic of future investigation.

Presently, the time-dependent simulation goes through $\mathcal{O}(10^6)$ time steps to reach steady state. The time step is limited by the diffusive processes, namely resistivity and thermal conduction. These can be treated implicitly, allowing for much larger time steps. However, this may interfere will the effectiveness of the parallel computation process.

However, if only the steady state solution is needed, there is another alternative. It is possible to sacrifice time-dependent solutions by resorting to "local time stepping"[151], where each com-

putational cell uses a time step which is based on the local numerical stability criterion. Though the intermediate solutions provided by this method will be unphysical, they will converge to the correct steady state solution. The pros and cons of this approach have to be investigated.

6.2.2 Physical Models

The list of possible improvements to the physical model can be extensive.

The results presented here were obtained using a multi-level equilibrium ionization model for both argon and lithium propellents. There have been other indications[59, 60, 56, 61, 62] that, for the conditions of interest to gas-fed MPDT plasmas, the solution of flow fields using the seemingly restrictive assumption of equilibrium ionization may yield results that are sufficiently close to reality, at least for the case with argon as propellant. In the LiLFA simulations, however, the calculated ionization levels were higher than expected. This could be an artifice of the inlet boundary condition assumption, or could be due to the limitation of the equilibrium ionization model. Though there have been attempts[31, 30] to model ionizational nonequilibrium in argon-fed MPDTs, there has not been a detailed study of the state of ionization in the LiLFA. Given the importance of the ionization levels on the energetics and other plasma phenomena, this warrants further study.

As mentioned earlier, in the simulation of gas-fed MPDTs, a specified mass flow rate of the propellant enters at a specified temperature at sonic conditions at the inlet. In reality, the propellant is injected as neutral gas at room temperature, and it gets almost fully ionized within a few millimeters from the inlet[98]. Classical theory cannot explain this high rate of ionization, and it has been proposed[127] that a non-Maxwellian electron energy distribution, resulting from plasma microturbulence, is the cause for this. Since this process cannot be modeled by fluid theory, the inlet temperature in our simulation is chosen to be high enough (1.0 eV) such that the propellant is sufficiently ionized. Effectively, the backplate of the numerical model is not the true backplate of the FSBT, but a region located few millimeters downstream of it. Though this approach provides

sufficiently realistic results of the flowfield, it will be useful to develop a self-consistent model of ionization to incorporate into this code.

Since this code solves the governing equations in a time-dependent manner, it can be extended to the simulation of pulsed plasma thrusters (PPT) as well. Without delving into the details of physical processes in PPTs, it is clear that the most important additions to the code for this purpose should be a finite-rate ionization model, and a model for circuit equation[152].

In the current model, viscosity is neglected because its effect was argued to be insignificant. Given good physical models for the coefficient of viscosity, this effect can be introduced into the code without much difficulty. As mentioned in §2.3.2, there are theories in the literature that suggest that viscosity is important in thrust production[22] and energy dissipation[30, 29]. Incorporating viscosity into this code would enable it to test the propositions. On a similar note, the current model uses a scalar model for thermal conduction whereas it is a tensor in reality. Therefore, it will be interesting to implement the tensor model to see the effects of anisotropic thermal conduction.

As briefly mentioned in §4.1.2, there are two issues that remain to be explored in the application of boundary conditions: diffusion into the electrodes, and sheaths.

Ideally, a simulation would self-consistently and continuously compute the heat transfer from the plasma to the wall, then the heat transfer within the metallic conductor, then calculate the temperature distribution of the wall, and from that information recompute the heat transfer from the plasma to the wall. Clearly, these calculations are computationally expensive, and may be impractical. While the time-scale for the stabilization of plasma processes is $\mathcal{O}(100\mu s)$, the time-scale for equilibration of electrode thermal processes is ~ 10 minutes. Heiermann et al.[64] have attempted to do these calculations, but give no indicators to usefulness of a full-blown simulation.

On that note, it might be interesting to model the diffusion of the magnetic field into the electrodes as well. From the ratio of resitivities of the plasma ($\sim 10^{-3}-10^{-4}$ Ohm.m) and the electrode

143

($\sim 10^{-8}$ Ohm.m), it can be shown that the time scale for the penetration of magnetic field into the electrode is four to five orders of magnitude longer than in the plasma. For quasi-steady discharges (with pulse lengths ~ 1 ms) discussed in §4 it was assumed that the field does not penetrate the skin of the conductor. For the steady-state discharges (with run times of hours) discussed in §5 this work assumed the field had penetrated the conductor. Though these are perfectly reasonable assumptions, it might be interesting to see the effect of the time-dependent field diffusion into the electrode on the plasma.

In reality, there exists a non-quasineutral sheath at the interface of plasma and a solid boundary. For the plasma conditions of interest, the typical dimension of this quasineutral region, in which a large fraction of the voltage drop occurs, is $\sim \mathcal{O}(10^{-5})$m. Clearly, this cannot be self-consistently computed because: i) the physical processes in this region are beyond the regime of MHD theory, and ii) the dimensions are too small to be captured by grids. Therefore, the only way to include this effect is to superimpose an analytical sheath model as a boundary condition. Though an attempt was made by Boie *et al.*[56], it was later discontinued. Ideally, this model will incorporate the effect of thermionic emission, and possible effects of magnetic field, on a high-voltage sheath in an unsteady plasma.

While developing the equation of state model for lithium (§2.3.6), the effect of inter-particle potential was ignored in the calculation of the translational partition function. It might be worthwhile to investigate its effect of the plasma flowfield.

The most important, and the most urgent, improvement to this code should be to include applied magnetic fields. Currently, this code handles only self-induced magnetic field in the azimuthal direction. However, for many reasons, it is crucial to apply magnetic fields in the radial and axial directions:

1. Many MPDTs and LiLFAs require an applied field to have high efficiencies at relatively low power levels (< 250 kW). In fact, there has been far more experimental work done[153, 39,

142, 154, 77] on the applied-field LiLFA than the self-field version. The mechanism of thrust production in the applied-field thrusters is significantly different from the self-field version, and one cannot simply extrapolate from the latter to the former.

2. In some cases[26, 40] it has been established that using an applied magnetic field extends the regime of stable operation of the MPDT/LiLFA. A properly designed external magnetic field (B_r, B_z) which intercepts the anode surface can minimize voltage by: a.) enhancing electron mobility to the anode, since it is easier to conduct current along the field line (B_r) rather than across it, b.) a radial magnetic field can oppose the electromagnetic pinch by reducing axial current and by creating a swirl that ameliorates the effect of the pinch[155].

3. Properly designed magnetic nozzles can be useful in recovering the power lost in enthalpy at the exhaust. Magnetic nozzles are also prevalent in other plasma applications, and other plasma thruster concepts[156].

For the abovementioned reasons, adding applied magnetic fields to this code will immensely enhance its utility in practical thruster research. Self-field MPDTs and LiLFA in coaxial geometry only have the azimuthal component of the magnetic field (B_θ). However, applied magnetic fields in these devices are primarily in the radial and axial directions (B_r, B_z), and this code must be adapted to handle them. In addition, applied-field LiLFAs can have a substantial swirl velocity (V_θ), rendering the flowfield three dimensional. However, Mikellides *et al.*[80, 81] have shown that by assuming the swirl velocity to vary only in the radial and axial directions $(V_\theta(r, z))$, it is possible to get valuable insight into the operation of applied-field MPDTs. The feasibility of this approach to simulating applied-field LiLFA has to be investigated.

Throughout the course of this research, the stumbling block for this code has been regions of very low density. Quite often these regions also have substantial magnetic fields, resulting in large values of the Hall parameter. In these regions, due to low collisionality, the underlying continuum assumption breaks down. Simulating the flowfield entirely using a kinetic code is impractical, if

not impossible. However, it is possible to develop a hybrid code that treats the electrons using a fluid model and the ions using a kinetic model[157], and use it as a plug-in into this code when necessary.

The utility of this code can be extended into studying various MPDT/LiLFA/PPT research issues such as thermal modeling, near-electrode plasma characterization and electrode thermal management to understand erosion processes, propellant selection, active turbulence control, near-field plume model as a source for far-field plume simulations that study the role of plasma interactions and contamination of spacecraft, and other contentious issues in overall design optimization.

As a final note, it is worth noting that the code developed for this thesis can be used to study plasma flows in other propulsion devices such as the Variable Specific Impulse Magnetoplasma Rocket (VASIMR) [156], railguns[158], as well as non-propulsive applications such as plasma flow switch ciruit breakers[159] and Z-pinch devices for fusion[160].

Bibliography

[1] K.E. Tsiolkovsky. "Exploration of the Universe with Reaction Machines". *The Science Review*, 5, 1903. English translation from the website of *Tsiolkovsky State Museum of the History of Cosmonautics*.

[2] R.G. Jahn. *Physics of Electric Propulsion*. McGraw-Hill, 1968.

[3] National Aeronautics and Space Administration. The Vision for Space Exploration. *Annual Report*, 2004.

[4] A. C. Ducati, G. M. Giannini, and E. Muehlberger. "Experimental Results in High-Specific Impulse Thermo-Ionic Acceleration". *AIAA J.*, 2(8):1452–1454, 1964.

[5] R. G. Jahn and E. Y. Choueiri. Electric propulsion. *Academic Press Encyclopedia of Physical Science & Technology*, 2000.

[6] K. Sankaran, L. Cassady, A. D. Kodys, and E. Y. Choueiri. A Survey of Propulsion Options for Cargo and Piloted Missions to Mars, in "Astrodynamics, Space Missions, and Chaos". *Annals of the New York Academy of Sciences*, 1017:450–467, 2004.

[7] E. Stuhlinger. *Ion propulsion for space flight*. McGraw-Hill, 1964.

[8] E. Y. Choueiri, A. J. Kelly, and R. G. Jahn. "Mass Savings Domain of Plasma Propulsion for LEO to GEO transfer". *J. Spacecraft & Rockets*, 1993.

[9] P. J. Turchi. *"The Cathode Region of a Quasi-Steady Magnetoplasmadynamic Arcjet"*. PhD thesis, Princeton U., 1970.

[10] M. S. DiCapua. *"Energy Deposition in Parallel-Plate Plasma Accelerators"*. PhD thesis, Princeton U., 1971.

[11] J. S. Cory. *"Mass, Momentum and Energy Flow from an MPD Accelerator"*. PhD thesis, Princeton U., 1971.

[12] A. P. Bruckner. *"Spectroscopic Studies of the Exhaust Plume of a Quasi-Steady MPD Accelerator"*. PhD thesis, Princeton U., 1972.

[13] H.C. Martinache. *"A Theory on the Parallel-Plate Plasma Acceleration"*. PhD thesis, Princeton U., 1974.

[14] M. J. Boyle. *"Acceleration Processes in the Quasi-Steady Magnetoplasmadynamic Discharge"*. PhD thesis, Princeton U., 1974.

[15] A. J. Saber. *"Anode Power in a Quasi-Steady MPD Thruster"*. PhD thesis, Princeton U., 1974.

[16] L. K. Rudolph. *"The MPD Thruster Onset Current Performance Limitation"*. PhD thesis, Princeton U., 1980.

[17] D.Q. King. *"Magnetoplasmadynamic Channel Flow for Design of Coaxial MPD Thrusters"*. PhD thesis, Princeton U., 1981.

[18] D. D. Villani. *"Energy Loss Mechanisms in a Magnetoplasmadynamic Arcjet"*. PhD thesis, Princeton U., 1982.

[19] J. W. Barnett. *"Operation of the MPD Thruster with Stepped Current Input"*. PhD thesis, Princeton U., 1985.

[20] D. D. Ho. "Erosion Studies in a (MPD) Thruster". Master's thesis, Princeton U., 1981.

[21] D. I. Kaplan. "Performance Chatacteristics of Geometrically-Scaled Magnetoplasmady-namic (MPD) Thrusters". Master's thesis, Princeton U., 1982.

[22] M. J. Wolff. "A High Performance Magnetoplasmadynamic Thruster". Master's thesis, Princeton University, 1984.

[23] J. H. Gilland. "The Effect of Geometric Scale upon MPD Thruster Behavior". Master's thesis, Princeton University, 1988.

[24] W. A. Hoskins. "Asymmetric Discharge Patterns in the MPD Thruster". Master's thesis, Princeton University, 1990.

[25] E. Y. Choueiri. *"Electron-Ion Streaming Instabilities of an Electromagnatically Accelerated Plasma"*. PhD thesis, Princeton U., 1991.

[26] A. D. Gallimore. *"Anode Power Deposition in Coaxial MPD Thrusters"*. PhD thesis, Princeton U., 1992.

[27] J. E. Polk. *"Mechanisms of Cathode Erosion in Plasma Thrusters"*. PhD thesis, Princeton U., 1995.

[28] K. D. Diamant. *"The Anode Fall in a High Power Pulsed MPD Thruster"*. PhD thesis, Princeton U., 1996.

[29] D. J. Heimerdinger. *"Fluid Mechanics in a Magnetoplasmadynamic Thruster"*. PhD thesis, MIT, 1988.

[30] E. H. Niewood. *"An Explanation for Anode Voltage Drops in an MPD"*. PhD thesis, MIT, 1993.

[31] E. J. Sheppard. *"Ionization Nonequilibrium and Ignition in Self-Field Magnetoplasmadynamic Thrusters"*. PhD thesis, MIT, 1992.

[32] P. G. Mikellides. *"A Theoretical Investigation of Magnetoplasmadynamic Thrusters"*. PhD thesis, Ohio State U., 1994.

[33] J. Heiermann. *"A finite volume method for the solution of magnetoplasmadynamic conservation equations"*. PhD thesis, U. Stuttgart, Germany, 2002.

[34] K. Toki and K. Kuriki. On-orbit demonstration of a pulsed self-field magnetoplasmadynamic thruster system. *J. Prop. Power*, 16(5):880–886, 2000.

[35] R. A. Moore, G. L. Cann, and L. R. Gallagher. Performance of Hall Arc Jets with Lithium Propellant, Part I. *AFAPL-TR-65-48*, 1965.

[36] D. B. Fradkin. *"Analysis of Acceleration Mechanisms and Performance of an Applied Field MPD Arcjet"*. PhD thesis, Princeton U., 1973.

[37] S. D. Grishin, A. K. Litvak, S. N. Ogorodnikov, and V. N. Stepanov. "Intermediate-power steady-state plasma accelerator". *Sov. Phys. Tech. Phys.*, 22(2):280–285, 1977.

[38] J. E. Polk and T. J. Pivirotto. Alkali Metal Propellants for MPD Thrusters. *Conference on Advanced SEI Technologies, AIAA-91-3572*, September, 1991.

[39] V. Kim, V. Tikhonov, and S. Semenikhin. "Fourth Quarterly (Final) Report to NASA-JPL: 100-150 kW Lithium Thruster Research". *Technical Report NASW-4851*, 1997.

[40] V.P. Ageyev and V.G. Ostrovsky. "High-Current Stationary Plasma Accelerator of High Power". In *Proceedings of the 23rd International Electric Propulsion Conference*, Seattle, WA, USA, 1993. IEPC-93-117.

[41] K.E. Clark and R.G. Jahn. "Quasi-Steady Plasma Acceleration". *AIAA Journal*, 8:216–220, 1970.

[42] Akihiro Sasoh and Y. Arakawa. "Electromagnetic Effects in an Applied-Field Magneto-plasmadynamic Thruster". *Journal of Propulsion and Power*, 8:98–102, 1992. January-February.

[43] E.Y. Choueiri and J.K. Ziemer. "Quasi-Steady Magnetoplasmadynamic Thruster Performance Database". *Journal of Propulsion and Power*, 17:967–976, 2001. September-October.

[44] LaPointe Michael R. and Pavlos G. Mikellides. Design and operation of mw-class mpd thrusters at the nasa glenn research center. In *Joint Propulsion Conference*, Indianapolis, IN, USA, July, 2002. AIAA 2002-4113.

[45] R. Myers, M. Mantentiek, and M. LaPointe. MPD Thruster Technology. *Conference on Advanced SEI Technologies, AIAA-91-3568*, September, 1991.

[46] T. Wegmann et. al. Experimental comparison of steady-state nozzle type and cylindrical MPD thrusters at high current levels. In *International Electric Propulsion Conference*, Seattle, WA, USA, 1993. IEPC 93-122.

[47] E. Y. Choueiri. *Advanced Problems in Plasma Propulsion*. Princeton U. Lecture Notes, 1998.

[48] K. V. Brushlinskii, N. I. Gerlakh, and A. I. Morozov. "Calculation of two-dimensional unsteady plasma flows of finite conductivity in the presence of the Hall effect". *Magnitnaya Gidrodinamika (Magnetohydrodynamics)*, 1, 1967.

[49] K. V. Brushlinskii and A. I. Morozov. "On the Evolutionary of Equations of Magnetohydrodynamics Taking the Hall Effect into Account". *PMM Journal of Applied Mathematics and Mechanics*, 32:957–959, 1968.

[50] K. V. Brushlinskii, N. I. Gerlakh, and A. I. Morozov. "Effect of Finite Conductivity on Stationary Self-Contracting Plasma Flows". *Soviet Physics - Doklady*, 13:588–590, 1968.

[51] K. Toki I. Kimura and M. Tanaka. "Current Distribution on the Electrodes of MPD Arcjets". *AIAA J.*, 20(7):889, 1982.

[52] T.Ao and T. Fujiwara. Numerical and experimental study of an MPD thruster. *IEPC-84-08*, 1984.

[53] T. Miyasaka and T. Fujiwara. Numerical prediction of onset phenomenon in a 2-dimensional axisymmetric MPD thruster. *AIAA-99-2432*, 1999.

[54] J.M.G. Chanty and M. Martinez-Sanchez. Two-dimensional numerical simulation of MPD flows. *AIAA-87-1090*, 1987.

[55] M. LaPointe. Numerical simulation of geometric scale effects in cylindrical self-field MPD thrusters. *NASA-CR-189224*, 1992.

[56] C. Boie, M. Auweter-Kurtz, H.J. Kaeppeler, and P.C. Sleziona. Application of adaptive numerical schemes for MPD thruster simulation. *IEPC-97-115*, 1997.

[57] G. Caldo. "Numerical Simulation of MPD Thruster Flows with Anomalous Transport". Master's thesis, Princeton University, 1994.

[58] E.Y. Choueiri. "Anomalous resistivity and heating in current-driven plasma thrusters". *Phys. Plasmas*, 6(5):2290, 1999.

[59] M. Auweter-Kurtz et al. "Numerical Modeling of the Flow Discharge in MPD Thrusters". *J. Propulsion & Power*, 1989.

[60] H. O. Schrade, P. C. Sleziona, T. Wegmann, and H. L. Kurtz. "Basic Processes of Plasma Propulsion: Final Report". *AFOSR: 91-0118*, 1991.

[61] J. Heiermann, M. Auweter-Kurtz, J. J. Kaeppeler, A. Eberle, U. Iben, and P. C. Sleziona. Recent improvements of numerical methods for the simulation of MPD thruster flow on adaptive meshes. *IEPC-99-169*, 1999.

[62] J. Heiermann, M. Auweter-Kurtz, C.A. Coclici, A. Eberle, C.C. Munz, and P.C. Sleziona. Advanced finite volume methods for the simulation of MPD propulsion. *AIAA-99-2346*, 1999.

[63] J. Heiermann and M. Auweter-Kurtz. "Numerical and Experimental Investigation of the Current Distribution in Self-Field MPD Thrusters". In *Proceedings of the 37th Joint Propulsion Conference*, Salt Lake City, UT, 2001. AIAA-01-3498.

[64] J. Heiermann and M. Auweter-Kurtz. "Numerical Investigation of the Electrodes in High Power Self-Field MPD Thrusters". In *Proceedings of the 33rd Plasmadynamics and Lasers Conference*, Maui, HI, 2002. AIAA-02-2102.

[65] J. Heiermann, M.Auweter-Kurtz, and P.C. Sleziona. "Adaptive Computation of the Current-Carrying Plasma in an MPD Rocket Thruster". In *Time-Dependent Magnetohydrodynamics: Anayltical, Numerical, and Application Aspects*, 1998.

[66] H. P. Wagner, H. J. Kaeppeler, and M. Auweter-Kurtz. "Instabilities in MPD thruster flows: 2. Investigation of drift and gradient driven instabilities using multi-fluid plasma models". *Journal of Physics D: Applied Physics*, 31:529–541, 1998.

153

[67] P.J. Turchi, P.G. Mikellides, K.W. Hohman, R.J. Leiweke, I.G. Mikellides, C.S. Schmahl, N.F. Roderick, and R.E. Peterkin Jr. Progress in modeling plasma thrusters and related plasma flows. *IEPC-95-159*, 1995.

[68] M.R. LaPointe and P.G. Mikellides. "High Power MPD Thruster Development at the NASA Glenn Research Center". In *Proceedings of the 37th Joint Propulsion Conference*, Salt Lake City, UT, 2001. AIAA-01-3499.

[69] P. G. Mikellides. "Modeling and Analysis of a Megawatt-Class Magnetoplasmadynamic Thruster ". *Journal of Propulsion and Power*, 20(2):204–210, 2004.

[70] M. H. Frese. "A Two-Dimensional Magnetohydrodynamic Simulation Code for Complex Experimental Configurations". *Mission Research Corporation report to Air Force Weapons Laboratory*, AFWL/PA 87-626 : AMRC-R-874, 1987.

[71] D.C. Lilekis and R.E. Peterkin Jr. Effects of azimuthal injection asymmetry of MPD thruster performance using the MACH3 code. *IEPC-95-2677*, 1995.

[72] Jeffrey and Taniuti. *Nonlinear Wave Propagation With Applications to Physics and Magnetohydrodynamics*. Academic Press, 1964.

[73] R. S. Myong. *"Theoretical and Computational Investigation of Nonlinear Waves in Magnetohydrodynamics"*. PhD thesis, U. Michigan, 1996.

[74] R. J. Goldston and P. H. Rutherford. *Introduction to Plasma Physics*. Institute of Physics Publishing, 1995.

[75] H. Maecker. "Plasma Jets in Arcs in a Process of Self-Induced Magnetic Compression". *Z. Phys.*, 141(1):198–216, 1955.

[76] E.Y. Choueiri. "The Scaling of Thrust in Self-Field MPD Thrusters". *J. Prop. Power*, 14(5):744–753, 1998.

[77] V. B. Tikhonov and S. A. Semenihin. "Research on Plasma Acceleration Processes in Self-Field and Applied Magnetic Field Thrusters". In *Proceedings of the 23rd International Electric Propulsion Conference*, Seattle, WA, USA, 1993. IEPC-93-076.

[78] M. Mitchner and C.H. Kruger. *Partially Ionized Gases*. Willy-Interscience, 1973.

[79] F.F. Chen. *Plasma Physics and Controlled Fusion*. Plenum Press, 1984.

[80] P. G. Mikellides, P. J. Turchi, and N. F. Roderick. Applied-Field Magnetoplasmadynamic Thrusters, Part 1: Numerical Simulations Using the MACH2 Code. *J. Prop. Power*, 16(5):887–893, 2000.

[81] P. G. Mikellides and P. J. Turchi. Applied-Field Magnetoplasmadynamic Thrusters, Part 2: Analytic Expressions for Thrust and Voltage. *J. Prop. Power*, 16(5):894–901, 2000.

[82] Yu. P. Raizer. *Gas Discharge Physics*. Springer, 1997.

[83] S. C. Brown. *Basic Data of Plasma Physics*. American Institute of Physics, 1994.

[84] R. J. LeVeque, D. Mihalas, E. A. Dorfi, and E. Müller. *Computational Methods for Astrophysical Fluid Flow*. Springer, 1998.

[85] D. E. Post, R. V. Jensen, C. B. Tarter, W. H. Grasberger, and W. A. Lokke. Steady State Radiative Cooling Rates for Low-Density High-Temperature Plasmas. *PPPL-1352*, 1972.

[86] W. G. Vincenti and C.H. Kruger. *Introduction to Physical Gas Dynamics*. Kruger Publishing, 1965.

[87] W. M. Sparks and D. Fischel. *"Partition Functions and Equations of State in Plasmas"*. NASA SP-3066, 1971.

[88] E. Y. Choueiri. "A Scaling Strategy for the Preliminary Design of MPD Thrusters". Master's thesis, Syracuse University, 1983.

[89] J. A. Blink. "Lithium Equation-of-State". *Lawrence Livermore Laboratory Report*, EMA 82-176, 1983.

[90] J. C. Boettger and S. B. Trickey. "Equation of state and properties of lithium". *Physical Review B*, 32(6):3391–3398, 1985.

[91] J. C. Boettger. "Sesame Equation of State Number 2293, Li". *Los Alamos National Laboratory Report*, LA-11338-MS, 1988.

[92] G. E. Rolader and J. H. Batteh. "Thermodynamic and Electrical Properties of Railgun Plasma Armatures". *IEEE Transactions on Plasma Science*, 17(3):439–445, 1989.

[93] C. E. Moore. *"Atomic Energy Levels"*. National Standard Reference Data System, 1971.

[94] W. L. Wiese, M. W. Smith, and B. M. Glennon. *Atomic Transition Probabilities*. National Standard Reference Data System, 1966.

[95] E.Y. Choueiri. "Instability of a current-carrying finite-beta collisional plasma". *Phys. Review E*, 64(6), 2001.

[96] E.Y. Choueiri, A. J. Kelly, and R.G. Jahn. Current-driven plasma acceleration versus current-driven energy dissipation: Part ii: Electromagnetic wave stability theory and experiments. *IEPC-91-100*, 1991.

[97] D.L. Tilley, E.Y. Choueiri, A. J. Kelly, and R.G. Jahn. "Microinstabilities in a 10-kilowatt Self-Field Magnetoplasmadynamic Thruster". *J.Prop.Power*, 12(2):381, 1996.

[98] T. M. Randolph. "Measurement of Ionization Levels in the Interelectrode Region of an MPD Thruster". Master's thesis, Princeton University, 1994.

[99] M. N. Saha. "Ionization in the Solar Chromosphere". *Phil. Mag.*, 40:472, 1920.

[100] J. L. Kerrebrock and M. A. Hoffman. "Nonequilibrium Ionization Due to Electron Heating". *AIAA J.*, 2:1072, 1964.

[101] S. Suckewer. "Excitation and Ionization of Atoms and Ions in a Non-Thermal Plasma. II: Ionization Equilibrium". *J. Phys. B*, 3:390–398, 1970.

[102] J. Vlcek. "A Collisional-Radiative Model Applicable to Argon Discharges Over A Wide Range of Conditions: Formulation and Basic Data". *J. Phys.D*, 22:623, 1988.

[103] V. Kaufmann and W. Whaling. "Improved Wavelengths and Energy Levels of Doubly-Ionized Argon (Ar III)". *J. Res. Natl. Inst. Stand. Technol.*, 101:691, 1996.

[104] J.U. Brackbill and D.C. Barnes. "The effect of nonzero $\nabla \cdot \mathbf{B}$ on the numerical solution of the magnetohydrodynamic equations". *J. Comp. Phys*, 35:426, 1980.

[105] K.G. Powell. An approximate Riemann solver for magnetohydrodynamics (that works in more than one dimension). *NASA ICASE Report 94-24*, 1994.

[106] E. Godlewski and P. A. Raviart. *Numerical Approximation of Hyperbolic Systems of Conservation Laws*. Springer, 1996.

[107] L. Martinelli. *"Calculations of Viscous Flows With a Multigrid Method"*. PhD thesis, Princeton U., 1987.

[108] J. von Neumann. "A Method for the Numerical Calculation of Hydrodynamic Shocks". *J. Appl. Phys.*, 21:232–237, 1950.

[109] C. B. Laney. *Computational Gasdynamics*. Cambrigde, 1998.

[110] H. L. Royden. *Real Analysis*. MacMillan, 1968.

[111] A. Harten. "High Resolution Schemes for Hyperbolic Conservation Laws". *J. Comp. Phys*, 49:357–393, 1983.

[112] A. Jameson. "Analysis and Design of Numerical Schemes for Gas Dynamics, 1: Artificial Diffusion, Upwind Biasing, Limiters and Their Effect on Accuracy and Multigrid Convergence". *Comp.Fluid.Dyn*, 1995.

[113] S.K. Godunov. "Finite Difference Method for Numerical Computation of Discontinous Solution of the Equations of Fluid Dynamics". *Matematicheskii Sbornik*, 47:15–21, 1959.

[114] S.K. Godunov. "Symmetric Form of the Equations of Magnetohydrodynamics". *Numerical Methods for Mechanics of Continuum Medium*, 1972.

[115] S. C. Jardin. *Computational Methods in Plasma Physics*. Princeton U. Lecture Notes, 1998.

[116] P. Roe. "Approximate Riemann Solvers, parameter Vectors, and Difference Schemes". *J. Comp. Phys*, 43:357, 1981.

[117] P. Roe. "Characteristics-Based Schemes for the Euler Equations". *Annual Review of Fluid Mechanics*, 18:337, 1986.

[118] P. Cargo and G. Gallice. "Roe Matrices for Ideal MHD and Systematic Construction of Roe Matrices for Systems of Conservation Laws". *J. Comp. Phys*, 136:446, 1997.

[119] N. Aslan. "Two-dimensional solutions of MHD equations with an adapted Roe method". *Int. J. Num. Meth. in Fluids*, 23(11):1211, 1996.

[120] B. van Leer, C. H. Tai, and K. G. Powell. Design of optimally smoothing multi-stage schemes for the euler equations. *AIAA-89-1933*, 1989.

[121] G.A Sod. "A Survey of finite-difference methods for systems of nonlinear conservation laws". *J. Comp. Phys*, 27:1, 1978.

[122] M. Brio and C.C. Wu. "An Upwind Differencing Scheme for the Equations of Ideal Magnetohydrodynamics". *J. Comp. Phys*, 1988.

[123] J.B. Taylor. "Relaxation of Toroidal Plasma and Generation of Reverse Magnetic Fields". *Physical Review Letters*, 1974.

[124] U. Shumlak. Development of an advanced implicit algorithm for MHD computations on parallel supercomputers. *AFRL-SR-BL-TR-00-0654*, 1999.

[125] S. G. Sheffer. *"Parallel Computation of Supersonic Reactive Flows with Detailed Chemistry Including Viscous and Species Diffusion Effects"*. PhD thesis, Princeton U., 1997.

[126] W. Gropp, E. Lusk, and A. Skjellum. *Using MPI*. MIT Press, 1999.

[127] E.Y. Choueiri and H. Okuda. "Anomalous ionization in MPD thrusters". In *Proceedings of the 23rd International Electric Propulsion Conference*, Seattle, WA, USA, 1993. IEPC-93-067.

[128] V. A. Abramov, I. U. P. Dontsov, V. I. Kogan, P. E. Kovrov, A. I. Morozov, A. K. Vinogradova, and I. U. A. Zaveniagin. "Investigation of Electron Temperature and Plasma Radiation in a Quasi-Steady High-Current Discharge Between Coaxial Electrodes". In *Proceedings of the 8th International Conference on Phenomena in Ionized Gases*, 1968.

[129] J.D. Jackson. *Classical Electrodynamics*. Wiley, 1975.

[130] A. J. Kelly and R. G. Jahn. "Pulsed Electromagnetic Acceleration: JPL contract no.954997". *MAE Report*, 1692.23, 1986.

[131] R. G. Jahn. Personal communication. *Princeton University*, 2000.

[132] K. Sankaran, L. Martinelli, S.C. Jardin, and E.Y. Choueiri. "A Flux-Limited Numerical Method for the MHD Equations to Simulate Propulsive Plasma Flows". *Int. J. Num. Meth. Eng.*, 53(5):1415–1432, 2002.

[133] K. Sankaran, E.Y. Choueiri, and S.C. Jardin. "Application of a New Numerical Solver to the Simulation of MPD Flows". In *Proceedings of the 36th Joint Propulsion Conference*, Huntsville, AL, 2000. AIAA-2000-3537.

[134] K. Sankaran, S.C. Jardin, and E.Y. Choueiri. "Parallelization and Validation of an MHD Code for the Simulation of Self-Field MPDT Flows". In *Proceedings of the 27th International Electric Propulsion Conference*, Pasadena, CA, 2001. IEPC-01-127.

[135] P. J. Turchi and R. G. Jahn. "Cathode Region of a Quasi-Steady MPD Arcjet". *AIAA J.*, 9(7), 1971.

[136] R. G. Jahn, W. F. von Jaskowsky, and K. E. Clark. "Pulsed Electromagnetic Acceleration". *MAE Report*, 1467a, 1979.

[137] R. Frisbee and N. Hoffman. "SP-100 Nuclear Electric Propulsion for Mars Cargo Missions". In *Proceedings of the 29th Joint Propulsion Conference*, Monterey, CA, 1993. AIAA-93-2092.

[138] J. Polk, R. Frisbee, S. Krauthamer, V. Tikhonov, S. Semenikhin, and V. Kim. "Technology requirements for high-power Lithium Lorentz Force Accelerators". In *14th Symposium on Space Nuclear Power and Propulsion*, pages 1505–1513, Albuquerque, NM, 1997.

[139] J. E. Polk. Personal communication. *NASA-JPL*, 2003.

[140] L.I. Ageyev, S.D. Grishin, V.G. Mikhalev, S.N. Ogorodnikov, and V.N. Stepanov. Characteristics of high-current plasma sources with a hollow cathode. *Radio Engineering and Electronic Physics-USSR*, 20(9):67–71, 1975.

[141] G.V. Babkin, V.G. Mikhalev, E.P. Morozov, and A.V. Potapov. An experimental investigation of a plasma in a multichannel cathode. *Journal of Applied Mechanics and Technical Physics*, 17(6):767–770, 1976.

[142] G. Popov, V. Kim, V. Tikhonov, S. Semenikhin, and M. Tibrina. "The Fourth (Final) Quarterly Report on the Milestones". *NASA-JPL-960938*, 1998.

[143] M. Krishnan, R. G. Jahn, W. F. von Jaskowsky, and K. E. Clark. "Physical Processes in Hollow Cathodes ". *AIAA Journal*, 15(9):1217–1223, 1977.

[144] K. Sankaran. "Simulation of MPD Flows Using a Flux-Limited Numerical Method for the MHD Equations". Master's thesis, Princeton University, 2001.

[145] N. V. Belan, V. P. Kim, A. I. Oranskii, and V. B. Tikhonov (Translated into English by R. Spektor). *Stationary Plasma Thrusters*. Kharkov Aviation Institute, 1989.

[146] K. Sankaran, E.Y. Choueiri, and S.C. Jardin. "Comparison of Simulated Plasma Flowfields to Experimental Measurements for a Gas-Fed Magnetoplasmadynamic Thruster". *Journal of Propulsion and Power (accepted for publication in April 2004)*, 2004. (accepted for publication).

[147] F. G. Baksht, B. Ya. Moizhes, and A. B. Rybakov. "Critical mode in a coaxial plasma accelerator with external magnetic field". *Soviet Physics Technical Physics*, 21(2):150–152, 1976.

[148] A.D. Gallimore, A.J. Kelly, and R.G. Jahn. "Anode Power Deposition in Magnetoplasmadynamic Thrusters". *J. Propulsion & Power*, 9(3):361–368, 1993.

[149] Kevin D. Diamant, Edgar Choueiri, and R.G. Jahn. "The role of spot mode transition in the anode fall of pulsed MPD thrusters". *J. Propulsion & Power*, 14(6):1036–1042, 1998.

[150] A. G. Korsun. "Current limiting by self magnetic field in a plasma thruster". *Soviet Physics Technical Physics*, 19:124–126, 1974.

[151] C. Dawson and R. Kirby. "High Resolution Schemes for Conservation Laws with Locally Varying Time Steps". *SIAM Journal on Scientific Computing*, 22(6):2256–2281, 2001.

[152] J. K. Ziemer. *"Performance Scaling of Gas-Fed Pulsed Plasma Thrusters"*. PhD thesis, Princeton U., 2000.

[153] A. W. Blackstock, D. B. Fradkin, D. J. Roehling, and T. F. Stratton. "A Cesium MHD Arc Jet". *Journal of Applied Physics*, 39(7):3201–3209, 1968. June.

[154] G. Popov, V. Kim, V. Tikhonov, S. Semenikhin, and M. Tibrina. "The Fourth (Final) Quarterly Report on the Milestones (a)(4) and (a)(5)(D) of SoW of Contract No 960938 Between RIAME-MAI and JPL to NASA-JPL (Items 8 and 9 of Delivery Schedule)". *RIAME-MAI Technical Report, Moscow, Russia*, 1998.

[155] R. P. Hoyt, J. T. Scheuer, K. F. Schoenberg, R. A. Gerwin, R. W. Moses Jr., and I. Hennis. "Magnetic Nozzle Design for Coaxial Plasma Accelerators". *IEEE Transactions on Plasma Science*, 23(3):481–494, 1995.

[156] F. R. Chang Diaz, J. P. Squire, R. D. Bengston, B. N. Breizman, F. W. Baity, and M. D. Carter. The physics and engineering of the VASIMR engine. *AIAA-00-3756*, 2000.

[157] D. W. Swift. "Use of a Hybrid Code for Global-Scale Plasma Simulation". *Journal of Computational Physics*, 126:109–121, 1996.

[158] M. H. Frese. The internal structure and dynamics of the railgun plasma armature between infinitely wide ablating rails. *Los Alamos Natl. Lab. Technical Report: LA-SUB-93-178*, 1993.

[159] J. Buff, M. H. Frese, A. J. Giancola, R. E. Peterkin, and N. F. Roderick. "Simulations of a plasma flow switch". *IEEE Transactions on Plasma Science*, PS-15:766–771, 1987.

[160] U. Shumlak. A near-term, z-pinch fusion space thruster. *AIAA-2000-3368*, 2000.

[161] The Planetary Society. Nuclear Space Initiative: A Planetary Society White Paper. *The Planetary Report*, 2002.

[162] K. Sankaran, L. Cassasy, A. D. Kodys, and E. Y. Choueiri. A Survey of Propulsion Options for Cargo and Piloted Missions to Mars. *International Conference on New Trends in Astrodynamics*, 2003.

[163] J. E. Polk, R. Y. Kakuda, J. R. Anderson, J. R. Brophy, V. K. Rawlin, M. J. Patterson, J. Sovey, and J. Hamley. Validation of the NSTAR ion propulsion system on the Deep Space 1 mission. *AIAA-99-2274*, 1999.

[164] E. Stuhlinger and J.C. King. Concept for a Manned Mars Expediction with Electrically Propelled Vehicles. *Electric Propulsion Development: Progress in Astronautics and Aeronautics*, 9:647–664, 1963.

[165] E.P. Coomes, D.Q. King, and M.J. Patterson. PEGASUS: A Multi-Megawatt Nuclear Electric Propulsion System. *Third Annual Symposium on Space Nuclear Power*, 1986.

[166] D.Q. King and J.C. Sercel. A Review of the Multi-Megawatt MPD Thruster and Current Mission Applications. *AIAA-86-1437*, 1986.

[167] J.H. Gilland and R.M. Myers. Multimegawatt Electric Propulsion System Design Considerations. *AIAA-90-2552*, 1990.

[168] John S. Clark et. al. Nuclear electric propulsion: A "better, safer, cheaper" transportation system for human exploration of mars. In *Space Technology and Application International Forum*, Albequrque, NM, USA, 1994. January 9-13.

[169] D.G. Pelaccio, G.A. Rauwolf, G. Maggio, S. Patel, and K. Sorenson. An Examination of Emerging In-Space Propulsion Concepts for One-Year Crewed Mars Misisons. *Annual Symposium on Space Nuclear Power*, 2002.

[170] Robert H. Frisbee, Nathan J. Hoffman, and Kathy H. Murray. Sp-100 dynamic power and lithium propellant MPD nuclear electric propulsion technology requirements. In *Space Technology and Application International Forum*, Albequrque, NM, USA, 1994. January 9-13.

[171] R.H. Frisbee and N.J. Hoffman. Electric Propulsion Options for Mars Cargo Missions. *AIAA-96-3173*, 1996.

[172] James E. Polk et. al. Technology requirements for high-power lithium lorentz force accelerators. In *Space Technology and Application International Forum*, Albequrque, NM, USA, 2001.

[173] M. Noca, J.E. Polk, and R. Lenard. An Evolutionary Strategy for the Use of Nuclear Electric Propulsion. *Annual Symposium on Space Nuclear Power*, 2000.

[174] G. Woodcock et al. Benefits of nuclear electric propulsion for outer planet exploration. *AIAA-02-3548*, 2002.

[175] M. Martnez-Sanchez and J.E. Pollard. Spacecraft electric propulsion- an overview. *Journal of Propulsion and Power*, 14:688–699, 1998. September-October.

[176] E. Braden, I. Johnson, and T. Crain. RAPTOR: (RAPid Trajectory Optimization Resource). *Personal communication*, 2002.

[177] I. Johnson. The Davidon-Fletcher-Powell Penalty Function Method: A Generalized Iterative Technique for Solving Parameter Optimization Problems. *NASA-TN-D-8251*, 1976.

[178] H. Tahara, H. Yasui, Y. Kagaya, and T. Yoshikawa. Development of a Quasi-Steady MPD Arcjet Thruster for Near-Earth Missions. *AIAA-87-1001*, 1987.

[179] Matthew T. Domonkos, Michael J. Patterson, and Robert S. Jankovsky. Ion engine and hall thruster development at the NASA Glenn Research Center. In *International Mechanical Engineering Congress*, New Orleans, LA, USA, November 17-22 2002. IMECE 2002-34444.

[180] Steven Oleson et al. Mission Advantages of NEXT: NASA's Evolutionary Xenon Thruster. In *AIAA Joint Propulsion Conference*, Indianapolis, IN, July 7-10 2002. AIAA 2002-3969.

[181] S. Nakanishi and E.V. Pawlik. "Experimental Investigation of a 1.5-m-diam Kaufman Thruster". *Journal of Spacecraft and Rockets*, 5:801–807, 1968. July.

[182] C.L. Dailey and R.H. Lovberg. Pulsed Inductive Thrusters Performance Database for Megawatt Class Engine Applications. *AIAA-93-0103*, 1993.

[183] J.D. Huba. *NRL Plasma Formulary*. Naval Research Laboratory, 1994.

[184] K.G. Powell et al. An upwind scheme for magnetohydrodynamics. *AIAA-95-1704*, 1995.

[185] K.G. Powell et al. A solution-adaptive upwind scheme for ideal magnetohydrodynamics. *J. Comp. Phys*, 154:284–309, 1999.

Appendix A

PROPULSION OPTIONS FOR MISSIONS TO MARS[1]

A.1   Introduction

For the first time in over a decade NASA has been given the green light to pursue nuclear options for spacecraft propulsion. The Nuclear Space Initiative (NSI), approved under NASA's FY2003 budget, is a multi-year program expected to total \$2 billion with one goal being the development of space nuclear systems capable of 10-100 kW of power in space over the next ten years[161]. This initiative promises to open up the outer solar system to exploration by reducing spacecraft weight (propellant mass savings) and transit times (5 years versus 10 years to Pluto, with respect to chemical thrusters, at high power levels), and by providing a power supply to do science once the spacecraft arrives at the destination. As a result, the surface of Mars may now be accessible for long-term robotic and human exploration. The first-phase of a study comparing near-term propulsion options for a two-stage (cargo & piloted) mission to Mars was described in ref.[162].

---

[1]The work in this text was the contribution of the author and L. Cassady, A. D. Kodys and E. Y. Choueiri of Princeton University.

A condensed form of that study is presented here.

Because of their high exhaust velocities, electric propulsion (EP) systems can provide significant propellant savings over chemical thrusters for high ΔV missions[1] like this one, and have been popular in such mission studies. With the success of the ion thruster as the primary propulsion system on the Deep Space 1 mission[163], and other recent EP enabled missions, the field of electric propulsion has now come of age as a reliable and efficient way of accomplishing relatively low energy missions. Currently, various types of EP devices, resistojets, arcjets, ion thrusters, Hall thrusters, and to a lesser extent, pulsed plasma thrusters, are routinely used for station keeping and maneuvering satellites. However, research on high-power electric propulsion has stagnated over the last two decades. As a consequence of the revival of interest in nuclear space systems, high-power propulsion options, first investigated in the 1960s to early 1980s (cf. ref.[2]) and then abandoned or continued at lower power levels due to lack of power in space, are receiving renewed attention.

A.1.1   Review of Previous Studies

Since the dawn of the space age, many mission studies have been performed on expeditions to Mars. Stuhlinger *et al.*[164] were among the first to propose the use of electric propulsion for missions of this kind. In the last two decades, several noteworthy studies have examined the advantages and disadvantages of various propulsion systems for a mission to Mars.

Coomes *et al.*[165] propose the use of a magnetoplasmadynamic thruster operating at a power level of 6 MW for a piloted mission, and calculate a trip time of 600 days for Earth to Mars at this power level. King *et al.*[166] also examine the use of a MPDT for a similar mission and propose systems with input power up to 200 MW that can accomplish Earth-Mars round trip in less than a year. It is also suggested that MPDTs can offer trip time savings over chemical thrusters at power levels of 10 MW or higher. Gilland *et al.*[167] compare the use of MPDTs versus an array of

ion thrusters for a similar mission, using a curve-fit for η_{th} vs. I_{sp} for the performance of these thrusters. Clark *et al.*[168] examine a 8 MW piloted (35 mT) fast trajectory mission for trip time, safety and reliability, abort options, and other costs. Pelaccio *et al.*[169] provide a technology readiness assessment of various thrusters for such a mission.

Clark *et al.*[168] also consider 4 MW minimum energy trajectory for a Mars cargo mission. They estimate that an array of ion thrusters offer significant mass savings over nuclear thermal systems, while maintaining comparable trip times. Frisbee *et al.*[170, 171] assess the technology readiness and development requirements for dynamic power conversion, power processing, and thrusters for Mars cargo mission. Polk *et al.*[172] examine the lithium Lorentz force accelerator technology for reusable orbit transfer vehicle with a parametric study of required power level, specific mass of power plant and performance to focus technology development. Noca *et al.*[173] consider robotic missions to outer planets with power levels ranging from 100 kW to 1 MW, using ion engines. Woodcock *et al.*[174] consider three outer planetary missions with small payloads, and consider the use of various propulsion systems.

As described above, a lot of work has been done on investigating propulsion options for missions to Mars. However, the abovementioned studies either perform the analysis with *extrapolated data*, and/or look at the problem from the perspective of research guidelines for a *specific thruster*. Therefore, there is a need for a comparison of multiple propulsion options for this mission using measured performance data only, and that is the goal of this study.

A.1.2   Outline

The piloted mission to Mars mission, is described in detail in §A.2. As will be described in §A.3.1, this study is limited to thrusters that have been successfully operated (thrust measured) in the laboratory to keep with the near-term (10-20 years) spirit of the study and to perhaps provide some insight into technology drivers. The results of the mission analysis will be presented in §A.4.

Following that, in §A.6, we will briefly discuss the propulsion options that were not considered in this analysis.

A.2 Mission Description

Though ref.[162] considers a two-stage mission to Mars, only the piloted mission is discussed here. This mission involves transporting the crew and supplies, totaling 60 metric tons of payload from a low-Earth orbit (LEO) to Mars orbit. The propulsion systems for this mission would have a total power supply of $\mathcal{O}(1 \text{ MW})$ available, and the trip time must be less than one year, due to human health factors.

A.3 Propulsion Options

In this section, the propulsion systems that may be suitable for this mission will be briefly described. Because of their high I_{sp}, EP systems are naturally attractive candidates for this type of mission. Within the family of electric propulsion devices, several types of thrusters, conceptually, have the ability to process 100s of kilowatts to megawatts of power at reasonably high efficiencies. In table (A.4), the thrusters that have met the selection criteria §A.3.1 are listed. Further information on these devices can be obtained from recent surveys, such as refs.[175, 5]. First, the criteria used to select the thrusters will be described below.

A.3.1 Selection Criteria

While a variety of propulsion systems have been proposed for interplanetary missions, this analysis is restricted only to those that have:

1. been successfully characterized in a laboratory as a thruster (i.e., thrust and efficiency have

been measured directly),

2. demonstrated a *potential* for attaining a significant lifetime ($\mathcal{O}(100$ hours$)$),

3. the ability process at least 500 kW per thruster for the piloted mission, so that the number of thrusters per spacecraft is reasonable.

Since, at present, there do not exist conclusive lifetime assessment tests of *any* of the devices, consideration is given only to those that have operated with tolerable erosion for 100 hours.

At high power levels, measured thrust and efficiency data is available for only three main classes of thrusters, Hall thrusters, thermal arcjets, and magnetoplasmadynamic thrusters (MPDT). The only EP device to date to have demonstrated the ability to operate at megawatt power levels with a single (or reasonably small number of) thruster is the MPDT. For the MPDT two distinct variations exists differing in propellant and electrode design, both of which have been operated in the laboratory and will be discussed here.

Few thrusters have demonstrated performance at power levels of $\mathcal{O}$ (MW), and have survived many hours of laboratory testing. Consequently, the field narrowed down to gas-fed magnetoplasmadynamic thrusters (MPDT) and lithium Lorentz force accelerators (LiLFA). They will be briefly described in the subsequent sections.

Other promising thruster concepts, such as the ion thruster, Pulsed Inductive Thruster (PIT), and the VAriable Specific Impulse Magnetoplasma Rocket (VASIMR), that did not meet our selection criteria are discussed in §A.6.

A.4   Mission Analysis

The mission simulation is accomplished with RAPTOR (RAPid Trajectory Optimization Resource), an optimization program developed at NASA-Johnson Space Center for low-thrust, interplanetary missions[176]. The code analyzes the three parts of an interplanetary mission: the spiral to escape

from low Earth orbit, the heliocentric transfer, and the spiral to a circular orbit about the arrival planet. In the spiral phase, the code merely propagates the position of the spacecraft, without optimizing the trajectory. Throughout the spirals, thrust is directed along the velocity vector. The escape spiral begins with a circular orbit and is propagated until the vehicle has acquired a positive energy. The capture spiral is modeled in the reverse manner. The heliocentric portion is an optimization code based on the Davidon-Fletcher-Powell Penalty Function Method[177].

Thruster	Power (MW)	Thrust (N)	I_{sp}	Efficiency (%)	Reference
LiLFA	0.5	12	4077	60	[40]
H-MPDT-1*	1.5	26.3	4900	43	[178]
H-MPDT-2*	3.75	88.5	3500	43	[178]
H-MPDT-3*	7.5	60.0	6000	25	[43]
Argon MPDT	0.5	25.5	1099	28	[46]

Table A.1: Summary of performance of thrusters chosen for this study (* denotes quasi-steady data.)

The position and velocity of the departure and arrival planets are the boundary conditions. Given these, the code minimizes the total acceleration of the interplanetary trajectory. RAPTOR contains a genetic algorithm to converge on the proper Lagrange multipliers, trip length and departure date for the heliocentric code.

More details of how the code was used for this mission analysis will be given in §A.4.2.

A.4.1   Assumptions

In order to simplify our analysis, we have made the following assumptions for the present study, some of which will be relaxed in future studies.

171

1. The specific mass of the power supply, α_p, is assumed to be 4.0 kg/kW for all the cases. This is within the range of previous studies such as ref.[171] and ref.[167].

2. The specific mass of the thrusters for the piloted mission were all assumed to be 0.35 kg/kW [172]. Since many of the thruster considered in this study are still laboratory models, it is not easy to arrive at an accurate estimate for α_t. The influence of this assumption on the result is yet to be determined, since the mass of the thruster is expected to be only a small fraction of the total mass.

3. The arrival date on Mars orbit was fixed to be the same for all cases.

4. The piloted mission was analyzed at a power level of 7.5 MW, irrespective of the optimum power level of the thruster.

A.4.2 Calculations

For the thrusters that met our selection criteria (§A.3.1), we selected the highest measured performance data that was available and used it as input into the RAPTOR code. A summary of the thruster data is presented in table (A.4). As noted there, the data for the three types of hydrogen MPDT were obtained in a quasi-steady mode of operation, and it is expected to be a good indication of the steady-state performance as well[2].

For this study, we did not use the genetic algorithm to optimize the departure date due to the large amount time required to calculate the shortest trip. The dates of 12/1/2016 for the cargo, and 12/1/2018 for the piloted missions, were chosen as the arrival date at Mars (before the spiral) because those dates are expected to be near the minimum for those missions. The genetic algorithm was used to find the Lagrange multipliers and trip length that best satisfied the mission.

Given an initial mass in Earth orbit, the RAPTOR code can determine the final mass, or given a payload to Mars, the code can find the initial mass required. Since we have chosen a payload,

172

RAPTOR will be run in latter mode. First, RAPTOR executes the spiral in to Mars orbit to determine that portion's duration and the propellant the maneuver requires. The heliocentric code then uses the mass of the payload and propellant to begin its optimizations. In this mode the date of arrival in Mars' sphere of influence is the only controllable date, all else is referenced to that date. The heliocentric code optimizes "backward" in time to find the minimum acceleration (i.e., minimum propellant) trajectory. Finally, the spiral to escape from Earth is executed and the mass at escape is matched with that at the beginning of the heliocentric transfer. The genetic algorithm is used only with the heliocentric portion of the code.

A.5 Results

The results of the RAPTOR code under the assumptions of this study are given in figure (A.1). The results for the trip time can be considered accurate to within $\pm$ 10 days, and for the propellant mass within $\pm$ 1 mT. The accuracy of the trip time is based on the sum of the round offs in the convergence calculation of various phases of the trip, and the accuracy of the mass estimate is based on the sum of the uncertainty associated with estimating the mass of the components such as the tank mass, and other structural mass.

The RAPTOR code does not explicitly optimize for trip time, rather it finds the trajectory that minimizes acceleration. This amounts to minimizing the required initial mass in nuclear-safe earth orbit. Since the thruster mass, payload mass, and power supply masses were assumed to be constant for each stage of the mission, the initial mass is a function of propellant mass alone. The minimum acceleration trajectory will result in the minimum propellant used and hence the minimum initial mass. For the piloted portion of the mission, the desired propulsion option would be the one which accomplishes the mission in the least amount of time. Trip times ranged from 490 days for the H-MPDT-3 ([43]) to just under 340 days for the LiLFA. The 3.75 MW H-MPDT-2 ([178]) had a trip time of only about one month longer (380 days) than the LiLFA. However, the initial mass required

173

was also higher than the LiLFA. Due to its high specific impulse, the MPDT-3 required the least propellant mass fraction, 33% (45 mT), for the mission. However, its low efficiency (25%), and its lower thrust-to-power (compared to other choices at the same power level), prevented it from being competitive because of long trip time.

The range of trip times (340-490 days) depends upon the power level chosen (7.5 MW) for this stage of the mission. At that power level, the LiLFA is the best option, with the minimum trip time and a moderate propellant requirement (57% = 129 mT lithium) compared to other choices.
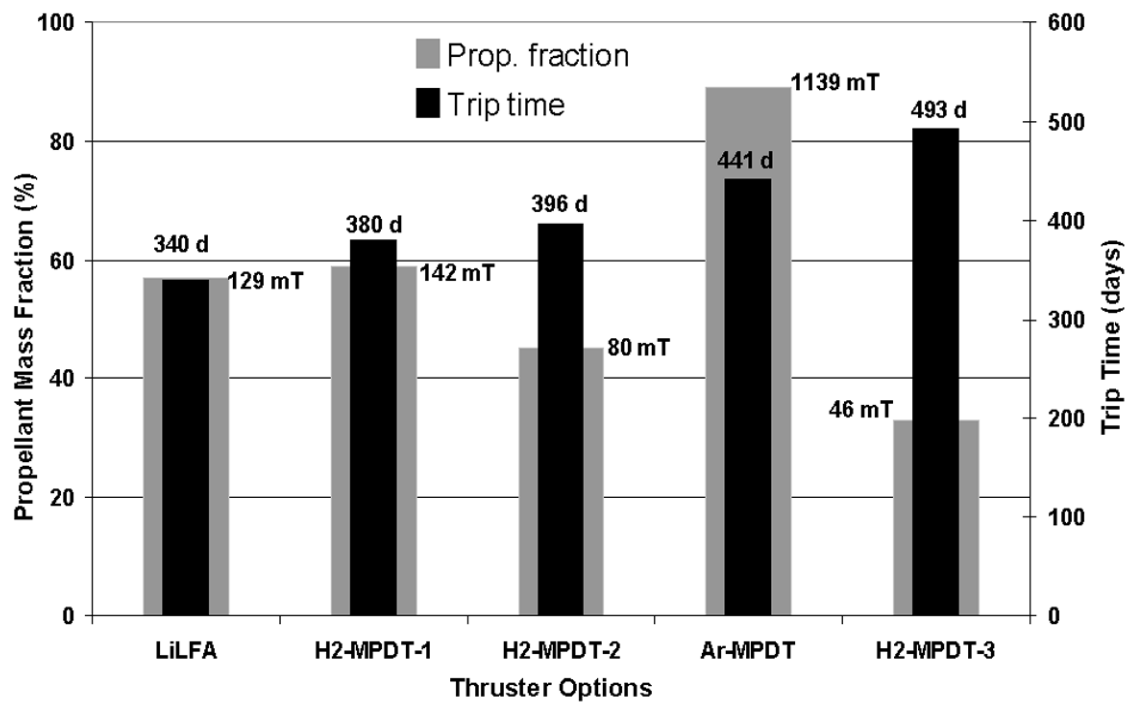

Figure A.1: Results of the piloted mission analysis (all set to arrive on 12/1/2018), with increasing trip time from left to right.

A.6 Other Viable Candidates

As mentioned in §A.3.1, we restricted our analysis to thrusters that have measured performance data, and have demonstrated significant lifetime. This eliminated many thruster concepts that may be promising for this mission.

Ion propulsion has demonstrated the in-space performance and lifetime necessary to be incorporated into future mission design and planning [179]. Good power throttling over a rather broad power range make ion propulsion ideal for solar electric propulsion missions where the electric power available varies with distance from the sun. In fact, the next-generation ion thrusters are being developed for such missions. NEXT, NASA's Evolutionary Xenon Ion Thruster, will provide higher power capabilities and lower specific mass with slightly increased exhaust velocities over Deep Space 1 technology[180]. These advances will meet the requirements of several near-term planetary missions including a Neptune orbiter and a Titan explorer[180].

Due to the electrostatic nature of ion propulsion, increased power (exhaust velocities) and propellant throughput (thrust) require corresponding increases in thruster size. The 30-cm DS1 thruster was capable of operation at up to 2.5 kW. The NEXT thruster will increase the effective area by 2, by moving to 40-cm diameter optics, and power capabilities near 10 kW. NASA's long-range goal for the development of ion engine technology is the demonstration of operation at 30 kW and above [179]. Work in 1968 investigated the feasibility of much higher power (> 100 kW) ion thrusters. Preliminary tests on a 150-cm engineering model showed that operation at 177 kW was possible with exhaust velocities in excess of 7000s and calculated efficiencies of 76%. Thruster conditioning and grid stability issues arose at this size and power, as well as a need for higher power electron sources [181]. Lack of potential missions at that time caused the research program to end before these issues were solved or thrust measurements could be obtained. However, there appears to be no fundamental limit on thrusters of this size and power[179].

Another thruster concept that could be promising is the pulsed inductive thruster (PIT) [182].

Using ammonia as propellant, this thruster demonstrated 48% efficiency, with Isp of 4000 s at discharge energy of 2 kJ per pulse. If this thruster can be operated at a pulsing frequency of ($\mathcal{O}$(100-1000 Hz)), it would be competitive with the LiLFA for the piloted mission. However, the PIT has yet to show potential for lifetime of the order of the mission duration for it to be a serious candidate.

In addition, there are other thruster concepts, such as the VAriable Specific Impulse Magneto-plasma Rocket (VASIMR)[156], that may be suited for this mission. The VASIMR is a two-stage plasma propulsion device: the production of the plasma is accomplished in the first stage, and the heating and acceleration in the second. It is hoped that the separation of these two processes would allow for better control of the exhaust velocity, while utilizing maximum available power. This device is intended to operate at power levels ranging from 10 kW to 100 MW. If proven, its ability to vary specific impulse independent of power (which will likely require varying the propellant), can reduce both trip time and propellant utilization. However, this device has not yet been successfully operated in the laboratory as a thruster, and propulsive characteristics and performance have not been directly measured.

A.7 Remarks

The goal of this study was to examine electric propulsion options for near-term (10-20 years) cargo and piloted missions to Mars. Thrusters for the study were chosen from the highest performance data available, subject to the following constraints: that they had demonstrated operation at power levels of 25 kW (cargo) or 500 kW (piloted) in a *single* laboratory thruster, that thrust measurements at this power level had been published, and has demonstrated a *potential* for lifetimes on the order of at least 100 hours. Power levels chosen for this study were 150 kW for the cargo mission and 7.5 MW for the piloted mission. Trajectory analysis was performed by the NASA-JSC RAPTOR code which optimized acceleration for the heliocentric portion of the mission.

The cargo mission results showed that several of the thrusters we considered are promising candidates. For a chosen power level of 150 kW, the AF-LiLFA and all three of Hall thrusters considered could deliver the 9 mT payload with nearly the same mass in earth orbit.

For the piloted mission at 7.5 MW, the lithium Lorentz force accelerator (LiLFA) provided trip times savings of at least one month over any of the MPDTs in the study. The initial mass required to accomplish this was in the middle of the range of the thrusters considered. Overall, the LiLFA seems to be a promising technology for high-power, high ΔV missions of this type. Because the power available for this mission is fixed at 7.5 MW, the range of trip times (340-490 days) is longer than the estimates in other studies that consider much higher power levels.

This study provides a survey of electric propulsion options for cargo and piloted Mars missions. In order to more completely determine the relative strengths and weaknesses of each system considered, several of our assumptions need to be addressed in future work. So far, we have completed only the first phase of this study, with strong assumptions on specific mass of components, and thruster operation at a single power level only. The next step would be to perform trajectory analysis for each mission stage at a range of power levels. This would allow for the determination on of the optimum thruster and power level for a given mission. In addition, the assumptions of constant thruster and power supply specific mass for all thruster options might have influenced our results, given the large variations in power requirements of each thruster. Obtaining better estimates of these values would increase the relevance of our results. Finally, in the next phase of this work, a parametric study of thruster efficiency and specific impulse will be undertaken, which could provide guidelines for future research in thruster design and optimization.

Appendix B

PHYSICAL MODELS

B.1 Equation of State

B.1.1 Lithium

Hill's equation:

$$
\gamma(T) = \begin{cases}
1.17256 + ((1.68755 - 1.17256) * T^{-4.16357} \\
/(T^{-4.16357} + 5413.43^{-4.16357})) & ; T \leq 1.1 \times 10^4 K, \\
1.14211 + ((1.65640 - 1.14211) * T^{3.33299} \\
/(T^{3.33299} + 21389.1^{3.33299})) & ; 1.1 \times 10^4 K \leq T \leq 7.5 \times 10^4 K
\end{cases}
$$
$$(B.1)$$

B.1.2 Argon

Refer to Fig.(2.8).

For the 10Pa case:

$$
\gamma(T) = \begin{cases}
C_1 + C_2 e^{-C_3 T} & ; 8000 < T < 10000 \\
C_4 + C_5 e^{-((T-C_6)/C_7)^2} & ; 10000 < T < 40000 \,,
\end{cases}
$$
$$(B.2)$$

where,

$$C_1 = 1.0846518,$$
$$C_2 = 143654.2145,$$
$$C_3 = 1.6201 \times 10^{-3},$$
$$C_4 = 1.096307595,$$
$$C_5 = 0.0242730046,$$
$$C_6 = 13643.43525,$$
$$C_7 = 2175.419991.$$

(B.3)

For the 100Pa case:

$$\gamma(T) = A + Be^{-((T-C)/D)^2},$$

(B.4)

where,

$$8000 < T < 10000 \quad :$$
$$A = 1.112166458,$$
$$B = 0.5299556066,$$
$$C = 8050.606514,$$
$$D = 1318.851134,$$
$$10000 < T < 40000 \quad :$$
$$A = 1.105400732,$$
$$B = 0.02526659335,$$
$$C = 15142.82094,$$
$$D = 2394.061632.$$

B.2 Collision Cross Section

Lithium:

$$
Q_{ea} = \begin{cases} 4.56166 \times 10^{-18} + (8.13214 \times 10^{-18} \sin((39.972T_e) + 4.85669)) & ; T_e \leq 0.08eV, \\ 1.17313 \times 10^{-19} + (2.42048 \times 10^{-18} \exp{(-1.00867T_e)}) & \\ +(2.82164 \times 10^{-17} \exp{(-12.2009T_e)}) & ; T_e > 0.08eV \end{cases},
$$

(B.5)

where T_e is in eV.

B.3 Radiation

$$
L(T_e) = \begin{cases} 1.297 \times 10^{-36} & ; T_e < 5.8 \times 10^4 K, \\ 10^{-13} ((9.13296 \times 10^{-22}) + (9.09094 \times 10^{-22} & \\ \times \sin((2.06274 \times 10^{-5}T_e) + 3.37656) & ; T_e \geq 5.8 \times 10^4 K \end{cases}.
$$

(B.6)

Appendix C

MATHEMATICAL MANIPULATIONS

C.1   Vector Identities

The vector identities used in this chapter are available from the NRL Plasma Formulary[183]. In this notation, $\mathbf{A}$, $\mathbf{B}$, $\mathbf{U}$ are vectors, $\bar{\bar{\mathcal{I}}}$ is the unit dyad and

$$(\nabla \times \mathbf{B}) \times \mathbf{B} = (\nabla\mathbf{B}) \cdot \mathbf{B} - (\mathbf{B} \cdot \nabla)\,\mathbf{B} \tag{C.1}$$

$$\nabla \cdot (\mathbf{A}\mathbf{B}) = (\nabla \cdot \mathbf{A})\,\mathbf{B} + (\mathbf{A} \cdot \nabla)\,\mathbf{B} \tag{C.2}$$

$$(\nabla\mathbf{B}) \cdot \mathbf{B} = \nabla \cdot \left[\frac{\mathbf{B} \cdot \mathbf{B}}{2} \bar{\bar{\mathcal{I}}} \right] \tag{C.3}$$

$$\nabla \times [\mathbf{u} \times \mathbf{B}] = [\mathbf{u}\,(\nabla \cdot \mathbf{B}) + (\mathbf{B} \cdot \nabla)\,\mathbf{u} - \mathbf{B}\,(\nabla \cdot \mathbf{u}) - (\mathbf{u} \cdot \nabla)\,\mathbf{B}] \tag{C.4}$$

$$\nabla \cdot \mathbf{A} = \frac{\partial A_r}{\partial r} + \frac{A_r}{r} + \frac{1}{r}\frac{\partial A_\theta}{\partial \theta} + \frac{\partial A_z}{\partial z} \tag{C.5}$$

$$\nabla \cdot \bar{\bar{\mathcal{T}}} = \begin{bmatrix} \frac{1}{r}\frac{\partial}{\partial r}\left(rT_{rr}\right) + \frac{\partial T_{zr}}{\partial z} - \frac{T_{\theta\theta}}{r} \\[2mm] \frac{1}{r}\frac{\partial}{\partial r}\left(rT_{r\theta}\right) + \frac{\partial T_{z\theta}}{\partial z} + \frac{T_{\theta r}}{r} \\[2mm] \frac{1}{r}\frac{\partial}{\partial r}\left(rT_{rz}\right) + \frac{\partial T_{zz}}{\partial z} \end{bmatrix} \tag{C.6}$$

$$\nabla \mathbf{A} = \begin{bmatrix} \frac{\partial A_r}{\partial r} & \frac{\partial A_\theta}{\partial r} & \frac{\partial A_z}{\partial r} \\[2mm] \frac{1}{r}\left(\frac{\partial A_r}{\partial \theta} - A_\theta\right) & \frac{1}{r}\left(\frac{\partial A_\theta}{\partial \theta} + A_r\right) & \frac{1}{r}\frac{\partial A_z}{\partial \theta} \\[2mm] \frac{\partial A_r}{\partial z} & \frac{\partial A_\theta}{\partial z} & \frac{\partial A_z}{\partial z} \end{bmatrix} \tag{C.7}$$

C.2   Mathematical Manipulations

Using the definition,

$$\bar{\bar{j}} = \frac{1}{\mu_o}\left[\nabla \mathbf{B} - \nabla \mathbf{B}^\dagger\right] \ ,$$

and the Ohm's law (without ∇p_e drift) written in the form,

$$\mathbf{E}' = \eta_o \mathbf{j} + \frac{\mathbf{j} \times \mathbf{B}}{en_e} = \bar{\bar{\eta}} \cdot \mathbf{j} \ , \tag{C.8}$$

the resistive diffusion of the magnetic field can be written as the divergence of the tensor,

$$\bar{\bar{E}}_{res} = \left[\bar{\bar{\eta}} \cdot \bar{\bar{j}}\right] - \left[\bar{\bar{\eta}} \cdot \bar{\bar{j}}\right]^\dagger - \left[\eta_o \bar{\bar{j}}\right] \ .$$

In other words,

$$\nabla \times \mathbf{E}' = -\nabla \cdot \bar{\bar{E}}_{res} \ . \tag{C.9}$$

Appendix D

EIGENSYSTEM OF MHD

Alfvèn speeds: $C_{A;r,\theta,z} = \frac{B_{r,\theta,z}}{\sqrt{\mu_o\rho}},$

Sonic speed: $a = \sqrt{\frac{\gamma p}{\rho}}$

Normalization coefficients (based on the work in refs.[184], [185])

$$\beta_{r;\theta,z} = \frac{C_{A;\theta,z}}{\sqrt{C_{A;\theta}^2+C_{A;z}^2}} \quad \alpha_{r;f,s} = \sqrt{\pm\frac{a^2 C_{S,F;r}^2}{C_{F;r}^2 - C_{S;r}^2}}$$

$$\beta_{z;r,\theta} = \frac{C_{A;r,\theta}}{\sqrt{C_{A;r}^2+C_{A;\theta}^2}} \quad \alpha_{z;f,s} = \sqrt{\pm\frac{a^2 C_{S,F;z}^2}{C_{F;z}^2 - C_{S;z}^2}}$$

Fast and slow magnetosonic waves:

$$C_{F,S;\,r}^2 = \frac{1}{2}\left[(\frac{\mathbf{B}\cdot\mathbf{B}}{\mu_o\rho} + a^2) \pm \sqrt{(\frac{\mathbf{B}\cdot\mathbf{B}}{\mu_o\rho} + a^2)^2 - (4a^2 C_{A;\,r}^2)}\right]$$

$$C_{F,S;\,z}^2 = \frac{1}{2}\left[(\frac{\mathbf{B}\cdot\mathbf{B}}{\mu_o\rho} + a^2) \pm \sqrt{(\frac{\mathbf{B}\cdot\mathbf{B}}{\mu_o\rho} + a^2)^2 - (4a^2 C_{A;\,z}^2)}\right]$$

The Jacobian of transformation between primitive and conservation variables:

$$\frac{d\mathbf{U}}{d\mathbf{W}} = \begin{bmatrix} 1 & 0 & 0 & 0 & 0 & 0 & 0 & \\ u & \rho & 0 & 0 & 0 & 0 & 0 & 0 \\ v & 0 & \rho & 0 & 0 & 0 & 0 & 0 \\ w & 0 & 0 & \rho & 0 & 0 & 0 & 0 \\ 0 & 0 & 0 & 0 & 1 & 0 & 0 & 0 \\ 0 & 0 & 0 & 0 & 0 & 1 & 0 & 0 \\ 0 & 0 & 0 & 0 & 0 & 0 & 1 & 0 \\ \frac{\mathbf{u} \cdot \mathbf{u}}{2} & \rho u & \rho v & \rho w & \frac{B_x}{\mu_o} & \frac{B_y}{\mu_o} & \frac{B_z}{\mu_o} & \frac{1}{\gamma - 1} \end{bmatrix}$$

D.1 $\hat{\mathbf{r}}$ Direction

D.1.1 Eigenvalues

(in non-decreasing order):

$$[u - C_{F;r},\ u - C_{A;r},\ u - C_{S;r},\ u,\ u,\ u + C_{S;r},\ u + C_{A;r},\ u + C_{F;r}]$$

D.1.2 Ortho-normalized eigenvectors

$$L1_r = \left[0, \frac{-\alpha_{r;f}C_{F;r}}{2a^2}, \frac{\alpha_{r;s}C_{S;r}\beta_{r;\theta}Sgn[B_r]}{2a^2}, \frac{\alpha_{r;s}C_{S;r}\beta_{r;z}Sgn[B_r]}{2a^2}, 0, \frac{\alpha_{r;s}\beta_{r;\theta}}{2a\sqrt{\mu_o\rho}}, \frac{\alpha_{r;s}\beta_{r;z}}{2a\sqrt{\mu_o\rho}}, \frac{\alpha_{r;f}}{2\rho a^2}\right]$$

$$L2_r = \left[0, 0, -\frac{\beta_{r;z}}{\sqrt{2}}, \frac{\beta_{r;\theta}}{\sqrt{2}}, 0, -\frac{\beta_{r;z}}{\sqrt{2\mu_o\rho}}, \frac{\beta_{r;\theta}}{\sqrt{2\mu_o\rho}}, 0\right]$$

$$L3_r = \left[0, \frac{-\alpha_{r;s}C_{S;r}}{2a^2}, \frac{-\alpha_{r;f}C_{F;r}\beta_{r;\theta}Sgn[B_r]}{2a^2}, \frac{-\alpha_{r;f}C_{F;r}\beta_{r;z}Sgn[B_r]}{2a^2}, 0, \frac{-\alpha_{r;f}\beta_{r;\theta}}{2a\sqrt{\mu_o\rho}}, \frac{-\alpha_{r;f}\beta_{r;z}}{2a\sqrt{\mu_o\rho}}, \frac{\alpha_{r;f}}{2\rho a^2}\right]$$

$$L4_r = \left[1, 0, 0, 0, 0, 0, 0, \frac{-1}{a^2}\right]$$

$$L5_r = [0, 0, 0, 0, 1, 0, 0, 0]$$

$$L6_r = \left[0, \frac{\alpha_{r;s}C_{S;r}}{2a^2}, \frac{\alpha_{r;f}C_{F;r}\beta_{r;\theta}Sgn[B_r]}{2a^2}, \frac{\alpha_{r;f}C_{F;r}\beta_{r;z}Sgn[B_r]}{2a^2}, 0, \frac{-\alpha_{r;f}\beta_{r;\theta}}{2a\sqrt{\mu_o\rho}}, \frac{-\alpha_{r;f}\beta_{r;z}}{2a\sqrt{\mu_o\rho}}, \frac{\alpha_{r;f}}{2\rho a^2}\right]$$

$$L7_r = \left[0, 0, -\frac{\beta_{r;z}}{\sqrt{2}}, \frac{\beta_{r;\theta}}{\sqrt{2}}, 0, \frac{\beta_{r;z}}{\sqrt{2\mu_o\rho}}, -\frac{\beta_{r;\theta}}{\sqrt{2\mu_o\rho}}, 0\right]$$

$$L8_r = \left[0, \frac{\alpha_{r;f}C_{F;r}}{2a^2}, \frac{-\alpha_{r;s}C_{S;r}\beta_{r;\theta}Sgn[B_r]}{2a^2}, \frac{-\alpha_{r;s}C_{S;r}\beta_{r;z}Sgn[B_r]}{2a^2}, 0, \frac{\alpha_{r;s}\beta_{r;\theta}}{2a\sqrt{\mu_o\rho}}, \frac{\alpha_{r;s}\beta_{r;z}}{2a\sqrt{\mu_o\rho}}, \frac{\alpha_{r;f}}{2\rho a^2}\right]$$

184

$$R1_r = \left[\rho\alpha_{r;f}, -\alpha_{r;f}C_{F;r}, \alpha_{r;s}C_{S;r}\beta_{r;\theta}Sgn\left[B_r\right], \alpha_{r;s}C_{S;r}\beta_{r;z}Sgn\left[B_r\right], 0, \alpha_{r;s}a\beta_{r;\theta}\sqrt{\mu_o\rho},\right.$$
$$\left.\alpha_{r;s}a\beta_{r;z}\sqrt{\mu_o\rho}, \rho a^2\alpha_{r;f}\right]$$

$$R2_r = \left[0, 0, \frac{-\beta_{r;z}}{\sqrt{2}}, \frac{\beta_{r;\theta}}{\sqrt{2}}, 0, \frac{-\beta_{r;z}\sqrt{\mu_o\rho}}{\sqrt{2}}, \frac{\beta_{r;\theta}\sqrt{\mu_o\rho}}{\sqrt{2}}, 0\right]$$

$$R3_r = \left[\rho\alpha_{r;s}, -\alpha_{r;s}C_{S;r}, -\alpha_{r;f}C_{F;r}\beta_{r;\theta}Sgn[B_r], -\alpha_{r;f}C_{F;r}\beta_{r;z}Sgn[B_r], 0, -\alpha_{r;f}a\beta_{r;\theta}\sqrt{\mu_o\rho},\right.$$
$$\left.-\alpha_{r;f}a\beta_{r;z}\sqrt{\mu_o\rho}, \rho a^2\alpha_{r;f}\right]$$

$$R4_r = [1, 0, 0, 0, 0, 0, 0, 0]$$

$$R5_r = [0, 0, 0, 0, 1, 0, 0, 0]$$

$$R6_r = \left[\rho\alpha_{r;s}, \alpha_{r;s}C_{S;r}, \alpha_{r;f}C_{F;r}\beta_{r;\theta}Sgn[B_r], \alpha_{r;f}C_{F;r}\beta_{r;z}Sgn[B_r], 0, -\alpha_{r;f}a\beta_{r;\theta}\sqrt{\mu_o\rho},\right.$$
$$\left.-\alpha_{r;f}a\beta_{r;z}\sqrt{\mu_o\rho}, \rho a^2\alpha_{r;f}\right]$$

$$R7_r = \left[0, 0, \frac{-\beta_{r;z}}{\sqrt{2}}, \frac{\beta_{r;\theta}}{\sqrt{2}}, 0, \frac{\beta_{r;z}\sqrt{\mu_o\rho}}{\sqrt{2}}, \frac{-\beta_{r;\theta}\sqrt{\mu_o\rho}}{\sqrt{2}}, 0\right]$$

$$R8_r = \left[\rho\alpha_{r;f}, \alpha_{r;f}C_{F;r}, -\alpha_{r;s}C_{S;r}\beta_{r;\theta}Sgn[B_r], -\alpha_{r;s}C_{S;r}\beta_{r;z}Sgn[B_r], 0, \alpha_{r;s}a\beta_{r;\theta}\sqrt{\mu_o\rho},\right.$$
$$\left.\alpha_{r;s}a\beta_{r;z}\sqrt{\mu_o\rho}, \rho a^2\alpha_{r;f}\right]$$

D.2 $\hat{z}$ Direction

D.2.1 Eigenvalues

(in non-decreasing order)

$$\left[\; w - C_{F;z}, \; w - C_{A;z}, \; w - C_{S;z}, \; w, \; w, \; w + C_{S;z}, \; w + C_{A;z}, \; w + C_{F;z} \;\right]$$

D.2.2 Ortho-normalized eigenvectors

$$L1_z = \left[0, \frac{\alpha_{z;s}C_{S;z}\beta_{z;r}Sgn[B_z]}{2a^2}, \frac{\alpha_{z;s}C_{S;z}\beta_{z;\theta}Sgn[B_z]}{2a^2}, \frac{-\alpha_{z;f}C_{F;z}}{2a^2}, \frac{\alpha_{z;s}\beta_{z;r}}{2a\sqrt{\mu_o\rho}}, \frac{\alpha_{z;s}\beta_{z;\theta}}{2a\sqrt{\mu_o\rho}}, 0, \frac{\alpha_{z;f}}{2\rho a^2}\right]$$

$$L2_z = \left[0, \frac{-\beta_{z;\theta}}{\sqrt{2}}, \frac{\beta_{z;r}}{\sqrt{2}}, 0, \frac{-\beta_{z;\theta}}{\sqrt{2\mu_o\rho}}, \frac{\beta_{z;r}}{\sqrt{2\mu_o\rho}}, 0, 0\right]$$

$$L3_z = \left[0, \frac{-\alpha_{z;f}C_{F;z}\beta_{z;r}Sgn[B_z]}{2a^2}, \frac{-\alpha_{z;f}C_{F;z}\beta_{z;\theta}Sgn[B_z]}{2a^2}, \frac{-\alpha_{z;s}C_{S;z}}{2a^2}, \frac{-\alpha_{z;f}\beta_{z;r}}{2a\sqrt{\mu_o\rho}}, \frac{-\alpha_{z;f}\beta_{z;\theta}}{2a\sqrt{\mu_o\rho}}, 0, \frac{\alpha_{z;s}}{2\rho a^2}\right]$$

$$L4_z = [0, 0, 0, 0, 0, 0, 1, 0]$$

$$L5_z = \left[1, 0, 0, 0, 0, 0, 0, \frac{-1}{a^2}\right]$$

$$L6_z = \left[0, \frac{\alpha_{z;f}C_{F;z}\beta_{z;r}Sgn[B_z]}{2a^2}, \frac{\alpha_{z;f}C_{F;z}\beta_{z;\theta}Sgn[B_z]}{2a^2}, \frac{\alpha_{z;s}C_{S;z}}{2a^2}, \frac{-\alpha_{z;f}\beta_{z;r}}{2a\sqrt{\mu_o\rho}}, \frac{-\alpha_{z;f}\beta_{z;\theta}}{2a\sqrt{\mu_o\rho}}, 0, \frac{\alpha_{z;s}}{2\rho a^2}\right]$$

$$L7_z = \left[0, \frac{-\beta_{z;\theta}}{\sqrt{2}}, \frac{\beta_{z;r}}{\sqrt{2}}, 0, \frac{\beta_{z;\theta}}{\sqrt{2\mu_o\rho}}, \frac{-\beta_{z;r}}{\sqrt{2\mu_o\rho}}, 0, 0\right]$$

$$L8_z = \left[0, \frac{-\alpha_{z;s}C_{S;z}\beta_{z;r}Sgn[B_z]}{2a^2}, \frac{-\alpha_{z;s}C_{S;z}\beta_{z;\theta}Sgn[B_z]}{2a^2}, \frac{\alpha_{z;f}C_{F;z}}{2a^2}, \frac{\alpha_{z;s}\beta_{z;r}}{2a\sqrt{\mu_o\rho}}, \frac{\alpha_{z;s}\beta_{z;\theta}}{2a\sqrt{\mu_o\rho}}, 0, \frac{\alpha_{z;f}}{2\rho a^2}\right]$$

$$R1_z = \left[\rho\alpha_{z;f}, \alpha_{z;s}C_{S;z}\beta_{z;r}Sgn[B_z], \alpha_{z;s}C_{S;z}\beta_{z;\theta}Sgn[B_z], -\alpha_{z;f}C_{F;z}, \alpha_{z;s}a\beta_{z;r}\sqrt{\mu_o\rho},\right.$$
$$\left.\alpha_{z;s}a\beta_{z;\theta}\sqrt{\mu_o\rho}, 0, \rho a^2\alpha_{z;f}\right]$$

$$R2_z = \left[0, \frac{-\beta_{z;\theta}}{\sqrt{2}}, \frac{\beta_{z;r}}{\sqrt{2}}, 0, \frac{-\beta_{z;\theta}\sqrt{\mu_o\rho}}{\sqrt{2}}, \frac{\beta_{z;r}\sqrt{\mu_o\rho}}{\sqrt{2}}, 0, 0\right]$$

$$R3_z = \left[\rho\alpha_{z;s}, -\alpha_{z;f}C_{F;z}\beta_{z;r}Sgn[B_z], -\alpha_{z;f}C_{F;z}\beta_{z;\theta}Sgn[B_z], -\alpha_{z;s}C_{S;z}, -\alpha_{z;f}a\beta_{z;r}\sqrt{\mu_o\rho},\right.$$
$$\left.-\alpha_{z;f}a\beta_{z;\theta}\sqrt{\mu_o\rho}, 0, \rho a^2\alpha_{z;s}\right]$$

$$R4_z = [0, 0, 0, 0, 0, 0, 1, 0]$$

$$R5_z = [1, 0, 0, 0, 0, 0, 0, 0]$$

$$R6_z = \left[\rho\alpha_{z;s}, \alpha_{z;f}C_{F;z}\beta_{z;r}Sgn[B_z], \alpha_{z;f}C_{F;z}\beta_{z;\theta}Sgn[B_z], \alpha_{z;s}C_{S;z}, -\alpha_{z;f}a\beta_{z;r}\sqrt{\mu_o\rho},\right.$$
$$\left.-\alpha_{z;f}a\beta_{z;\theta}\sqrt{\mu_o\rho}, 0, \rho a^2\alpha_{z;s}\right]$$

$$R7_z = \left[0, \frac{-\beta_{z;\theta}}{\sqrt{2}}, \frac{\beta_{z;r}}{\sqrt{2}}, 0, \frac{\beta_{z;\theta}\sqrt{\mu_o\rho}}{\sqrt{2}}, \frac{-\beta_{z;r}\sqrt{\mu_o\rho}}{\sqrt{2}}, 0, 0\right]$$

$$R8_z = \left[\rho\alpha_{z;f}, -\alpha_{z;s}C_{S;z}\beta_{z;r}Sgn[B_z], -\alpha_{z;s}C_{S;z}\beta_{z;\theta}Sgn[B_z], \alpha_{z;f}C_{F;z}, \alpha_{z;s}a\beta_{z;r}\sqrt{\mu_o\rho},\right.$$
$$\left.\alpha_{z;s}a\beta_{z;\theta}\sqrt{\mu_o\rho}, 0, \rho a^2\alpha_{z;f}\right]$$